Title: Non-invasive assessment of normal and impaired iron homeostasis in living human brains.

Authors: Shir Filo[1], Rona Shaharabani[1], Daniel Bar Hanin[1], Masha Adam[1], Eliel Ben-David[2], Hanan Schoffman[3], Nevo Margalit[4], Naomi Habib[1], Tal Shahar[3,4†], Aviv Mezer[1†]

Affiliations:

[1]The Edmond and Lily Safra Center for Brain Sciences, The Hebrew University of Jerusalem, Israel;

[2]The Department of Radiology; [3]The Laboratory of Molecular Neuro-Oncology and [4]The Department of Neurosurgery, Shaare Zedek Medical Center, Faculty of Medicine, The Hebrew University of Jerusalem, Israel

† Equal contributions.

Abstract: Strict iron regulation is essential for normal brain function. The iron homeostasis, determined by the milieu of available iron compounds, is impaired in aging, neurodegenerative diseases and cancer. However, non-invasive assessment of different molecular iron environments implicating brain tissue's iron homeostasis remains a challenge. We present a novel magnetic resonance imaging (MRI) technology sensitive to the iron homeostasis of the living brain (the r1-r2* relaxivity). *In vitro*, our MRI approach reveals the distinct paramagnetic properties of ferritin, transferrin and ferrous iron. In the *in vivo* human brain, we validate our approach against ex vivo iron compounds quantification and gene expression. Our approach varies with the iron mobilization capacity across brain regions and in aging. It reveals brain tumors' iron homeostasis, and enhances the distinction between tumor tissue and non-pathological tissue without contrast agents. Therefore, our approach may allow for non-invasive research and diagnosis of iron homeostasis in living human brains.

Graphical abstract: *Non-invasive assessment of normal and impaired iron homeostasis in living human brains.*

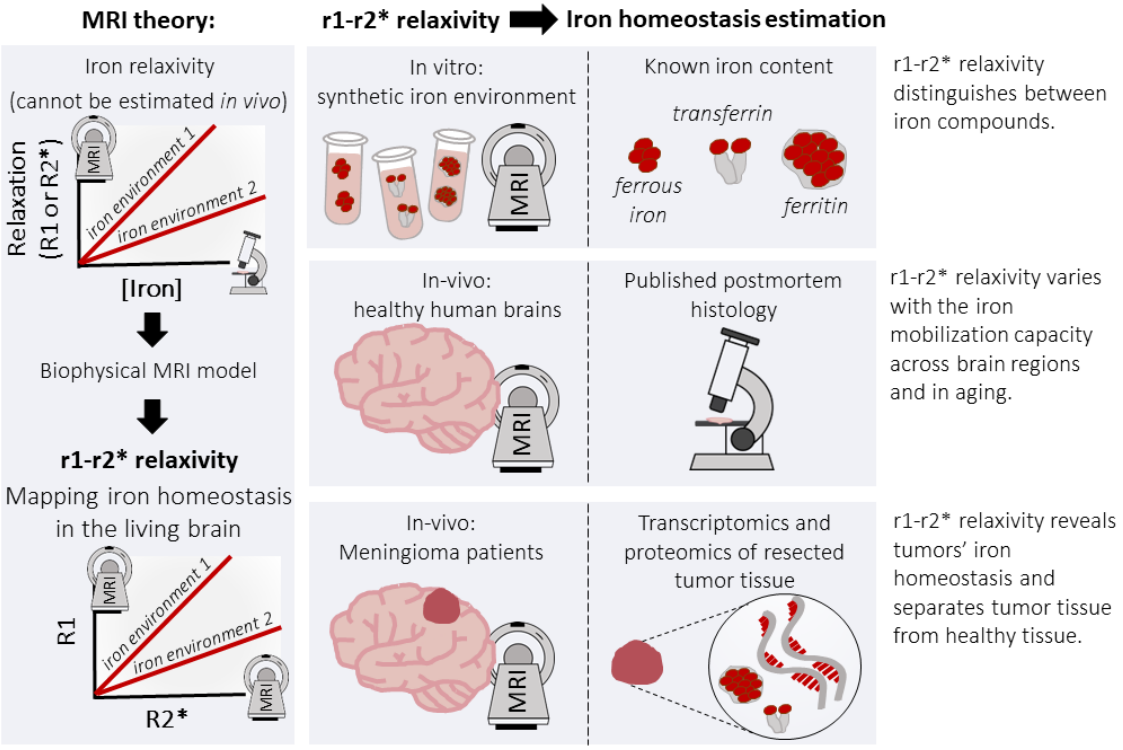

Introduction:

Iron is the most abundant trace element in the human body[1]. It participates in fundamental processes such as oxygen transport, cellular metabolism, myelin formation and the synthesis of neurotransmitters[1–4]. Therefore, strict iron regulation is essential for maintaining normal brain function. Brain tissue's iron homeostasis could be characterized by the tissue's molecular iron environment, determined by the specific milieu of available iron compounds, their iron binding capacities and aggregation states. Importantly, the molecular iron environment varies between cell types and across brain regions[3,5–7].

Disrupted iron homeostasis plays a major role in normal aging and in neurodegenerative diseases such as Parkinson's disease (PD), Alzheimer's disease (AD), multiple sclerosis, Friedreich's ataxia, aceruloplasminaemia, neuroferritinopathy, Huntington's disease, and restless legs syndrome[1,2,5–10]. The two iron compounds most involved in iron homeostasis are transferrin and ferritin[3]. Transferrin, the main iron transport protein, carries iron from the blood into brain tissue, while ferritin, the main iron storage protein, stores excess iron atoms. When iron concentrations exceed the capacity of iron-binding proteins, this can lead to oxidative stress and cellular damage[10]. For example, the ratio of transferrin to iron, which reflects iron mobilization capacity, differs between elderly controls and patients (AD and PD) in a brain-region–dependent manner[7]. In addition, specifically in the substantia nigra and the locus coeruleus, reduction in neuromelanin-iron complexes is considered a biomarker for PD and AD[11,12].

Impaired homeostasis of the molecular iron environment also have been reported in cancer cells[13,14]. Tumor cell proliferation requires a modulated expression of proteins involved in iron uptake. In addition, iron may affect the immune surveillance of tumors[15]. Therefore, the availability of iron in the tumor cells' microenvironment may affect their survival and growth rate, and subsequently the course of the disease. For example, meningioma brain tumors[16], compared to non-pathological tissue, were shown to contain a higher concentration of ferrimagnetic particles and abnormal expression of iron-related genes[17,18]. These findings suggest there are detectable differences in iron homeostasis between brain tumors and normal brain tissue.

The extensive implications of impaired iron homeostasis in normal aging, neurodegeneration and carcinogenesis suggest that assessment of iron homeostasis in the living brain would be highly valuable for diagnosis, therapeutic monitoring, and understanding pathogenesis of diseases[4]. Iron's paramagnetic properties make magnetic resonance imaging (MRI) a perfect candidate for non-invasive estimation of iron content in brain tissue. In particular, iron is a major contributor to the longitudinal and effective transverse relaxation rates, R1 and R2* respectively[19–22]. These relaxation rates can be measured using quantitative MRI (qMRI) techniques[23–26]. Indeed, *in vivo* studies often use these qMRI measurements as a proxy for iron presence in brain tissue[21,27–31]. However, a major limitation of current MRI techniques is that they lack information regarding the state of iron homeostasis, as they do not have the sensitivity to discriminate between different molecular environments of iron in the brain[4].

Early *in vitro* and postmortem works suggest that different iron environments can be distinguished by their iron relaxivity[31–35]. The iron relaxivity is defined as the dependency of MR relaxation rates on the iron concentration[36]. It was shown that iron relaxivity varies with the specific environment in which the iron resides[31–35]. However, a major limitation of this approach is that it requires direct estimation of the tissue iron concentration, which can only be acquired *in vitro* or postmortem. Therefore, until now the phenomenon of iron relaxivity could not be studied in living humans.

Here we propose an *in vivo* iron relaxivity approach sensitive for the state of iron homeostasis in the brain. Our approach fully relies on MRI parameters, and does not require estimation of the tissue iron concentration, thereby allowing for the first time non-invasive assessment of different molecular iron environments in the living brain. We exploit the distinct iron relaxivities of the MR relaxation rates, R1 and R2*, to construct a biophysical model of their linear interdependency, which we label the r1-r2* relaxivity. Using the r1-r2* relaxivity, we argue that the distinct iron relaxivity of different molecular iron environments can be estimated *in vivo*. We confirm this hypothesis based on a novel validation framework. First, we used a bottom-up strategy in which we evaluated the r1-r2* relaxivity of different iron environments *in vitro*. Next, we used a top-down strategy in which we measured the r1-r2* relaxivity in human brains *in vivo* and compared it to ex vivo quantification of iron compounds and gene expression, both at the group and the

single-subject levels. In healthy subjects, we assessed the biological correlates of the r1-r2* relaxivity, and compared it to other MR contrasts across brain regions and in aging. In meningioma patients, we tested the ability of our approach to enhance the distinction between tumor tissue and non-pathological tissue, and to reveal the state of iron homeostasis in tumors. Therefore, we provide a well-validated MRI framework with great implications for the non-invasive research and diagnosis of normal and impaired iron homeostasis in living human brains (see graphical abstract).

Results:

The theoretical basis for the r1-r2 relaxivity.*

The iron relaxivity is defined based on the linear relationship between the relaxation rates (R1 and R2*) and the iron concentration ($[IC]$)[36]:

$$R_1 = r_{(1,IC)}[IC] + c_1 \qquad R_2^* = r_{(2,IC)}[IC] + c_2$$

The slopes of these linear dependencies, $r_{(1,IC)}$ and $r_{(2,IC)}$, represent the iron relaxivities of R1 and R2*, which were shown to have different values for different iron environments[31–34]. c_1 and c_2 are constants. Notably, the iron relaxivities require estimation of the iron concentration ($[IC]$), thereby limiting this approach to *in vitro* and ex vivo studies.

Here we propose a theory which advances the relaxivity model and provides *in vivo* iron relaxivity measurements for identifying different iron environments in the brain. We take advantage of the fact that R1 and R2* are governed by different molecular and mesoscopic mechanisms[37–39], and therefore each of them may have a distinct iron relaxivity in the presence of paramagnetic substances. Based on our theoretical framework ("*In vivo* iron relaxivity model" in Methods), the linear dependency of R1 on R2* can be described by the following equation:

$$R_1 = \frac{r_{(1,IC)}}{r_{(2,IC)}} * R_2^* + constant$$

The slope of this linear dependency ($\frac{r_{(1,IC)}}{r_{(2,IC)}}$) represents the ratio of the iron relaxivities, r_1 and r_2^*, which are sensitive to the molecular environment of iron. Therefore, we define this MRI-based

82 slope as the r1-r2* relaxivity ($\frac{r_{(1,IC)}}{r_{(2,IC)}}$) and hypothesize it reveals the distinct properties of
83 different molecular iron environments. Notably, in the brain, the r1-r2* relaxivity could be
84 affected by the entire milieu of available iron compounds, their iron binding capacities and
85 aggregation states (i.e. the molecular iron environment). For an extension of the relaxivity model
86 in the presence of a heterogeneous iron environment and myelin see **Supplementary Section 4.1:**
87 **The theoretical basis for the r1-r2* relaxivity of brain tissue.**

88 ***In vitro validation for the sensitivity of the iron relaxivity to molecular iron environments.***
89 Before implementing this approach in the living human brain, we validated our theory by
90 manufacturing *in vitro* samples of different iron environments in a synthetic cellular membrane
91 environment. These samples were scanned in the MRI to verify that different iron environments
92 have different iron relaxivities. We then tested whether our r1-r2* relaxivity theory could reveal
93 these different relaxivities.

94 We prepared samples of transferrin, ferritin and ferrous iron in different cellular-like
95 environments (free in water or adjacent to liposomes and proteins, to achieve physiological iron
96 concentrations the transferrin concentrations are higher than the ones measured *in vivo*[3,4]).
97 These highly controlled synthetic iron environments were scanned for R1 and R2* mapping. We
98 found that both R1 and R2* increased with the concentration of iron compounds (**Figure 1a-b**).
99 The rate of this increase, defined as the iron relaxivity, was different for different iron
100 environments (**Figure 1a-c**, p(ANCOVA)<10^{-50}). We show that R1 and R2* change both with the
101 type and concentration of iron, thereby making it impossible to distinguish between iron
102 environments with these measurements. For example, R1 increased with the ferritin
103 concentration, but also was higher for ferritin compared to transferrin (**Figure 1a-b**, **Sup. Figure 1a-**
104 **b**). Consequently, similar R1 values can be obtained for ferritin, transferrin and ferrous iron,
105 depending on their concentrations (**Sup. Figure 1b, Figure 1a**). This ambiguity can be resolved by
106 the iron relaxivity, which differentiated the iron environments, and was consistent when
107 computed over samples with higher or lower concentrations (**Sup. Figure 1c**). Therefore, we find

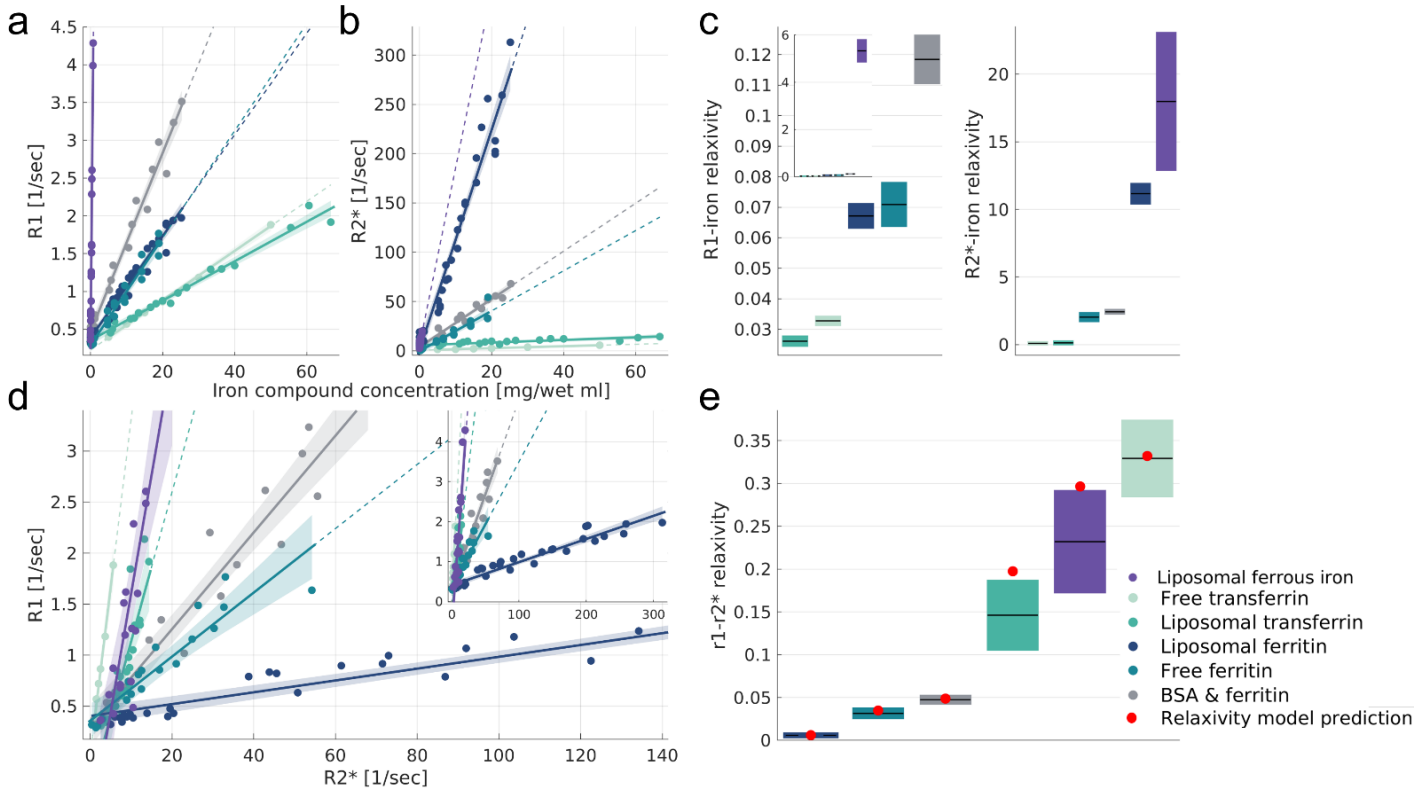

Figure 1: ***In vitro validation of the non-invasive framework for assessing the iron environments. (a-b)*** *The dependency of R1 and R2* on the iron compound concentrations for different iron environments: free ferritin, liposomal ferritin, bovine serum albumin (BSA)-ferritin mixture, free transferrin, liposomal transferrin and liposomal ferrous iron. Data points represent samples with varying concentrations relative to the water fraction ([mg/wet ml]). The linear relationships between relaxation rates and iron- compounds concentrations are marked by lines. We define the slopes of these lines as the iron relaxivities. Dashed lines represent extrapolation of the linear fit. Shaded areas represent the 95% confidence bounds.* ***(c)*** *The iron relaxivity of R1 and R2* is different for different iron environments (p(ANCOVA)<10^{-50}). Iron relaxivities are calculated by taking the slopes of the linear relationships shown in (a,b), and are measured in [sec^{-1}/(mg/wet ml)]. For each box, the central mark is the iron relaxivity (slope); the box shows the 95% confidence bounds of the linear fit. For the R1-iron relaxivity, the inset shows a zoom-out of the main figure, presenting the entire range of measured values* ***(d)*** *The dependency of R1 on R2* for different iron environments. Data points represent samples with varying iron compound concentrations relative to the water fraction. The linear relationships of R1 and R2* are marked by lines. The slopes of these lines are the r1-r2* relaxivities, which do not require iron concentration estimation and therefore can be estimated in vivo. Dashed lines represent extrapolation of the linear fit. Shaded areas represent the 95% confidence bounds. The inset shows a zoom-out of the main figure, presenting the entire range of measured R2* values* ***(e)*** *The r1-r2* relaxivities are different for different iron environments (p(ANCOVA)<10^{-38}). For each box, the central mark is the r1-r2* relaxivity, and the box shows the 95% confidence bounds of the linear fit. Red dots indicate the successful prediction of the experimental r1-r2* relaxivity from the ratio between the iron relaxivities of R1 and R2* ($\frac{r_{(1,IC)}}{r_{(2,IC)}}$, shown in c). This validates our theoretical in vivo relaxivity model.*

that the iron relaxivity reflects changes in the molecular environment of iron and is independent of the iron concentration. Ferritin binds thousands iron ions while transferrin binds only few[3]. Thus, we wanted to exclude the possibility that the relaxivity differences were being driven by the different iron ion concentration. We estimated the iron ion concentrations for the different molecular iron environments (see Methods), and verified that ferritin, transferrin and ferrous iron indeed have different iron relaxivities even when accounting for the discrepancies in iron concentrations (**Supplementary Section 1: The dependency of R1 and R2* on the iron concentration.**).

The r1-r2* relaxivity reveals the distinct iron relaxivities of different iron environments.

In agreement with previous findings[31–34], our *in vitro* experiments indicate that iron relaxivity can be used to identify different iron environments. While the iron relaxivity cannot be estimated *in vivo*, as it requires measurements of iron concentrations, the r1-r2* relaxivity only relies on MRI measurements that can be estimated *in vivo*. Based on our theory, we argue that two iron environments with different iron relaxivities are also likely to differ in their r1-r2* relaxivities. We validated this hypothesis using synthetic iron-containing samples. As predicted by our theoretical model, iron environments with different iron-relaxivities had different r1-r2* relaxivities (**Figure 1d-e**, p(ANCOVA)<10^{-38}). Notably, as suggested by our theoretical formulation, the r1-r2* relaxivity provides a good MRI approximation for the ratio between the iron relaxivities of R1 and R2* ($\frac{r_{(1,IC)}}{r_{(2,IC)}}$, **Figure 1e**). Similar to the iron relaxivities, the r1-r2* relaxivity is consistent across iron concentrations (**Sup. Figure 1d**). Hence, the r1-r2* relaxivity is more sensitive to the molecular iron environment than R1 and R2* by themselves. In addition, we validated that the r1-r2* relaxivity is sensitive to the paramagnetic properties of iron-binding proteins. We found that apo-transferrin (transferrin which is not bound to iron) has a much smaller r1-r2* relaxivity compared to iron-bound transferrin (p(ANCOVA)<10^{-8}; **Sup. Figure 4**). This implies that it is paramagnetic properties that induce the r1-r2* relaxivity that we measure. Taken together, these results validate our theory, indicating that the r1-r2* relaxivity can be used to measure iron relaxivity *in vivo* for exposing the distinct paramagnetic properties of different molecular iron environments.

135 Brain tissue includes a complex milieu of iron compounds and myelin, which is a major
136 contributor to R1 and R2*[4,19,25,29,40–45]. Therefore, we tested *in vitro* the r1-r2* relaxivity of a
137 heterogenous molecular iron environment of ferritin-transferrin liposomal mixtures
138 (**Supplementary Section 4.2: The r1-r2* relaxivity of ferritin and transferrin mixtures *in vitro*.**). We found
139 that changing the transferrin-ferritin ratio leads to considerable changes in the r1-r2* relaxivity,
140 even in mixtures with low ratio of transferrin compared to ferritin as in the brain[3]. Importantly,
141 these changes were above the detection limit of the *in vitro* r1-r2* relaxivity measurement (**Sup.**
142 **Figure 8**). Since myelin is composed mainly of lipids, we tested the effect of the myelin fraction on
143 the iron relaxivity by varying the liposomal fractions in our *in vitro* experiments. We found that
144 the r1-r2* relaxivities are stable for different liposomal fractions and lipid types (for more details
145 see **Supplementary Section 2: The dependency of the iron relaxivity on the liposomal fraction.**). These
146 results highlight the specificity of the r1-r2* relaxivity to differences in the molecular state of
147 iron, unlike the ambiguous measurements of R1 or R2* independently.

148 ***The r1-r2* relaxivity provides a new MRI contrast in the in vivo human brain.***

149 Following the *in vitro* validation, we measured the *r1-r2* relaxivity* in the living human brain. For
150 this aim we calculated the linear dependency of R1 on R2* across voxels of different
151 anatomically-defined ROIs (see "r1-r2* relaxivity computation for ROIs in the human brain" in
152 Methods). We found distinct r1-r2* relaxivities for different brain regions (**Figure 2a**). This
153 indicates a heterogeneous distribution of the *in vivo* iron relaxivity across the brain, which is
154 consistent across healthy subjects (age 27±2 years, N=21, **Figure 2b**) and is reproducible in scan-
155 rescan experiments (**Sup. Figure 9**).

156 In agreement with our *in vitro* results, which indicated that the r1-r2* relaxivity provides
157 different information compared to R1 and R2*, in the *in vivo* human brain we find that the r1-r2*
158 relaxivity produces a new contrast, statistically different from R1 and R2* (**Figure 2b-d**; $p<0.05$ for
159 the two-sample Kolmogorov–Smirnov test comparing the r1-r2* relaxivity distribution to R1, and
160 $p<0.001$ comparing it to R2*). While the r1-r2* relaxivity is calculated for an anatomically-
161 defined ROI in the brain, a voxel-wise r1-r2* relaxivity visualization based on each voxel's local
162 neighborhood, as well as comparison to the R1 and R2* contrasts, is demonstrated in
163 **Supplementary Section 3: Voxel-wise r1-r2* relaxivity visualization.**

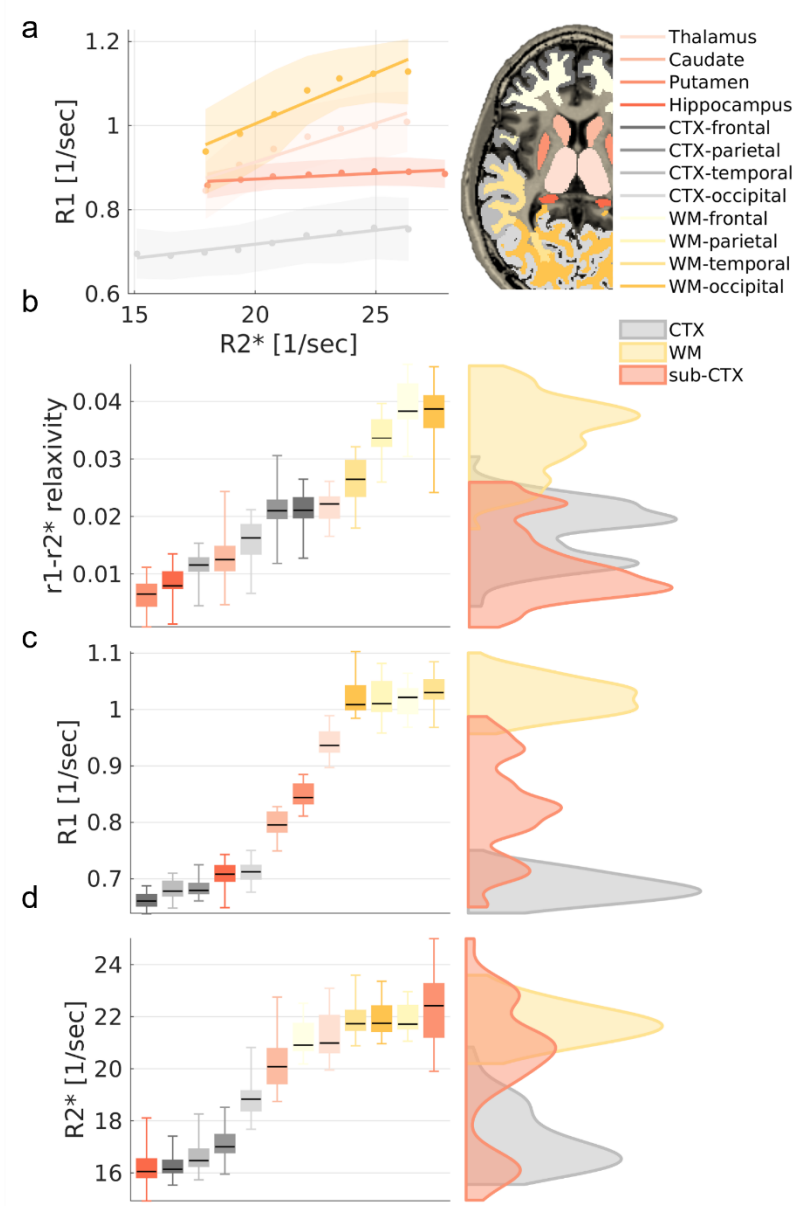

Figure 2: The *in vivo r1-r2* relaxivity provides a novel contrast in the brain.* ***(a)*** *The dependency of R1 on R2* in four representative brain regions (WM-occipital, CTX-occipital, Thalamus & Putamen) of a single subject. R2* and R1 were binned (dots represent the median; shaded areas represent the mean absolute deviation), and a linear fit was calculated. The slopes of the linear fit represent the dependency of R1 on R2* (r1-r2* relaxivity) and vary across brain regions.* ***(b)*** *The r1-r2* relaxivity across the brain. Left: the reliability of the method in different brain regions as observed by the variation in the r1-r2* relaxivity across normal subjects (age 27±2, N=21). The 25th, 50th and 75th percentiles and extreme data points are shown for each box. Right: the contrast of the r1-r2* relaxivity across the brain. Red, yellow and gray distributions represent the values of the r1-r2* relaxivities in sub-cortical (sub-CTX), white-matter (WM) and cortical (CTX) brain regions, respectively.* ***(c-d)*** *Similar analyses for R1 and R2* values, in which the gray-matter vs. white-matter contrast is much more dominant compared to the r1-r2* relaxivity. Hence, the r1-r2* relaxivity provides new information compared to R1 and R2*, beyond the WM-GM. Results in this entire figure are for ROIs in the left hemisphere. WM=white-matter, CTX=cortex.*

164 *The effect of myelin on the r1-r2* relaxivity*

165 The sensitivity of R1 and R2* to the myelin content is known to produce contrasts that are
166 governed mainly by the differences between white-matter and gray-matter tissues[4,19,25,29,40–44].
167 As expected, we find a strong distinction between gray-matter and white-matter regions in R1
168 and R2* values (**Figure 2c-d**). However, the contrast of the r1-r2* relaxivity across the brain shows
169 a novel spatial pattern and reveals differences between brain regions beyond the typical white
170 matter—gray matter differentiation. For example, we found the temporal, parietal and occipital
171 white-matter regions to be indistinguishable in terms of their R1 and R2* values (p(ANOVA)>0.4),
172 but these regions were separable based on their different r1-r2* relaxivities (p(ANOVA)<10^{-10},
173 **Sup. Figure 13**).

174 To further establish that the r1-r2* relaxivity is less sensitive to the myelin content relative to R1
175 and R2* we compared it to several *in vivo* myelin markers. The qMRI measurements of the
176 macromolecular tissue volume (MTV)[46],magnetization transfer saturation (MTsat)[47], and mean
177 diffusivity (MD) were shown to approximate the myelin content and characteristics[48–53]. These
178 myelin-sensitive markers were highly correlated with R1 and R2* but were not significantly
179 correlated with the r1-r2* relaxivity (**Figure 3a, Sup. Figure 14-15**). In a biophysical model of the r1-
180 r2* relaxivity, that accounts for the presence of myelin and iron compounds, we find that the
181 variability of myelin within an ROI can affect the r1-r2* relaxivity measurement (**Supplementary**
182 **Section 4.3: Numerical simulations of the r1-r2* relaxivity.**). Yet, an *in vivo* estimate of this myelin
183 characteristic revealed it explains only 30% of the variability in the *in vivo* r1-r2* relaxivity across
184 the brain (**Sup. Figure 27**). We also performed a set of numerical simulations in which we consider
185 the contributions of multiple brain tissue components to the relaxivity measurement
186 (**Supplementary Section 4.3: Numerical simulations of the r1-r2* relaxivity.**). As in the *in vivo* brain, we
187 found that changes in the myelin concentration substantially affect the simulated measurements
188 of R1 and R2*. However, myelin-related changes were not the main component governing the
189 simulated measurement of the r1-r2* relaxivity, and in simulations of physiological conditions
190 they could not explain the variability in the r1-r2* relaxivity across the brain.

191 *The r1-r2* relaxivity correlates with the iron mobilization capacity across the brain and in aging.*
192 Next, we tested the sensitivity of the *r1-r2* relaxivity* to the state of iron homeostasis across the

193 normal brain and in aging. We aggregated previously reported postmortem histological data
194 describing iron, ferritin and transferrin concentrations in different brain regions of young (aged
195 27-64 years, N>=7) and older (aged 65-88 years, N>=8) adults[5,7,9] (see "Group-level comparison
196 of qMRI parameters and histological measurements" in Methods). We performed a group-level
197 comparison between these postmortem findings and *in vivo* MRI parameters, which we
198 measured in the same brain regions and age groups (healthy young subjects aged 23-63 years,
199 N=26; older subjects aged 65-77 years, N=13). As expected, R2* was significantly correlated with
200 iron concentration (R^2=0.41, p-value (FDR)<0.05; **Figure 3b**). Importantly, this result validates the
201 agreement between the *in vivo* and postmortem datasets, thus allowing to further examine the
202 biological correlates of the r1-r2* relaxivity. For this aim we estimated a feature of the iron
203 homeostasis, the iron mobilization capacity (transferrin/iron[7]), available in the postmortem
204 dataset. This measure was not correlated with R2* or R1 (**Figure 3c**). However, the iron
205 mobilization capacity[5,7] was significantly correlated with the r1-r2* relaxivity across brain
206 regions and age groups (R^2=0.59, p-value(FDR)<0.001, **Figure 3c**). Hence, the r1-r2* relaxivity,
207 unlike R1 and R2*, is sensitive to the obtained *ex vivo* measurements of the iron mobilization
208 capacity across the brain and can capture the effect of aging on this iron homeostasis marker.

209 The r1-r2* relaxivity was much less correlated with the absolute ferritin, transferrin or iron
210 concentrations (**Figure 3b, Sup. Figure 18**). Moreover, the correlation with the iron concentration
211 was driven mostly by outliers (the globus pallidum), unlike the sensitivity of the r1-r2* relaxivity
212 to the iron homeostasis marker (**Supplementary Section 5: The r1-r2* relaxivity in the pallidum.**).
213 Therefore, the r1-r2* relaxivity is less sensitive to absolute changes in the iron and myelin
214 concentrations. In return, these results imply that the r1-r2* relaxivity enhances the sensitivity of
215 MRI to the iron homeostasis. We corroborated these findings with numerical simulations of the
216 r1-r2* relaxivity of brain tissue. In these simulations we further demonstrated that the measured
217 changes in the r1-r2* relaxivity across the brain can be induced by changes in the iron
218 environment (**Sup. Section 4.3**). Moreover, we find that the effect of the iron environment on the
219 r1-r2* relaxivity is not confounded by the myelin and iron concentrations and is well above the
220 detection limit of this MRI measurement (**Sup. Figure 9**). These analyses suggest that the *in vivo*

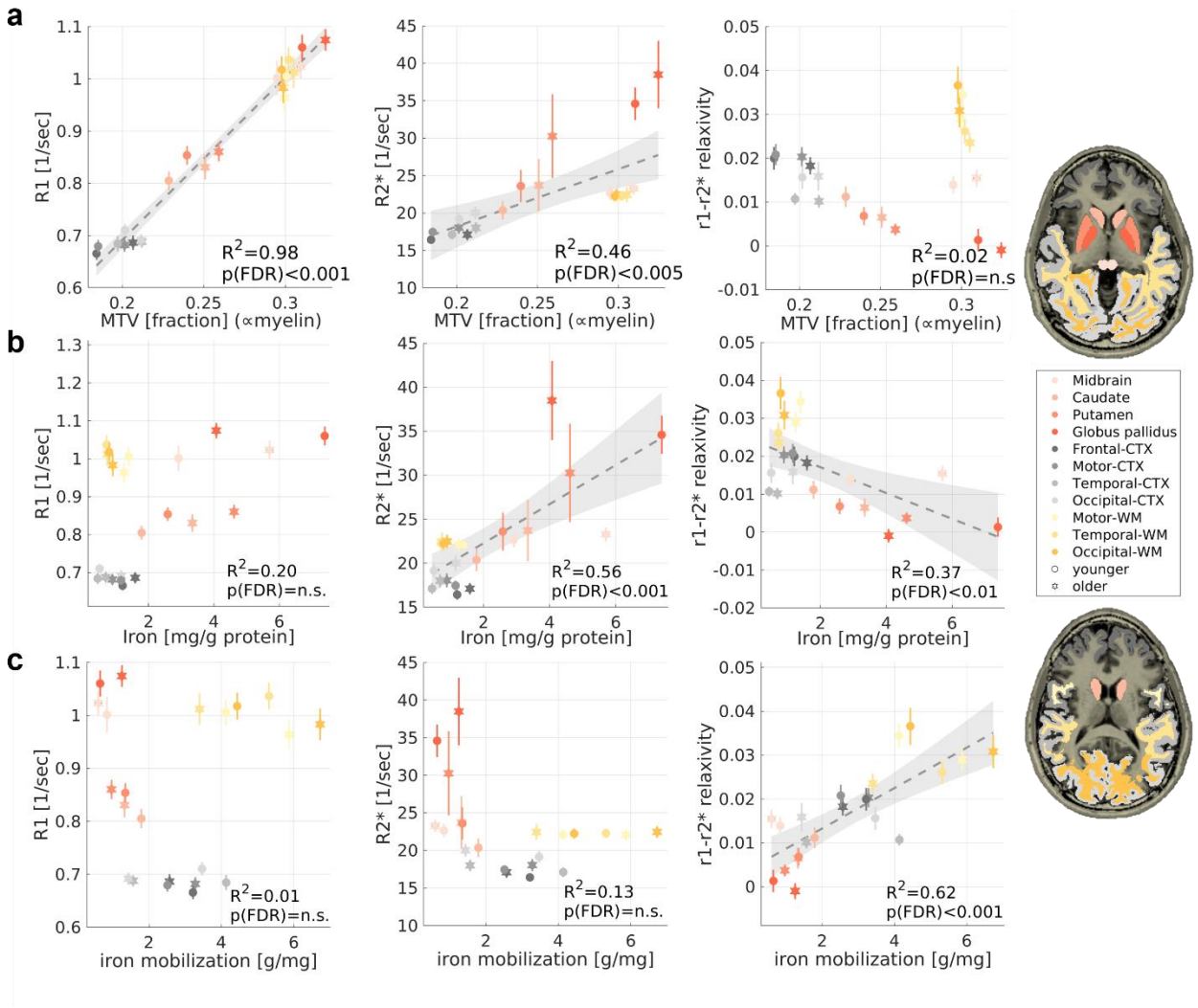

Figure 3: The r1-r2* relaxivity has unique biological correlates compared to R1 and R2* across the brain and in aging. *R1, R2* and the r1-r2* relaxivity were measured in vivo across younger (aged 23-63 years, N =26) and older (aged 65-77 years, N=13) subjects (different marker shapes) in 11 brain regions (different colors). Each row presents the correlations of these qMRI measurements with a different in vivo or* ex vivo *histological feature (fitted model and 95% confidence bounds are presented for significant correlations):* ***(a)*** *qMRI vs. the macromolecular tissue volume (MTV), an in vivo myelin-sensitive marker, measured for younger (aged 23-63 years, N =26) and older (aged 65-77 years, N=13) subjects. Unlike R1 and R2*, the r1-r2* relaxivity is not linearly related to this myelin-sensitive marker (See* ***Sup. Figure 14, Sup. Figure 15*** *for additional in vivo myelin-sensitive markers)* ***(b)*** *qMRI vs. the iron concentration (postmortem, from the literature[5,7]) measured for younger (aged 27-64 years, N>=7) and older (aged 65-88 years, N>=8) subjects. Please note that the r1-r2* relaxivity is not significantly correlated with the iron content when excluding the outlier values in the globus pallidum while the R2* correlation survives this exclusion (see* ***Sup. Figure 31****).* ***(c)*** *qMRI vs. the iron mobilization capacity (transferrin/iron ratio), an iron homeostasis marker (postmortem, from the literature[5,7], same subjects as in b). Only the r1-r2* relaxivity is significantly correlated with the iron mobilization capacity, implying for its sensitivity to the iron homeostasis across brain regions and in aging. WM=white-matter, CTX=cortex.*

221 r1-r2* relaxivity is capable of revealing important characteristics of the iron environment
222 previously inaccessible with MRI.

223 ***The r1-r2* relaxivity enhances the distinction between tumor tissues and non-pathological tissue.***

224 While the r1-r2* relaxivity forms a unique pattern of changes across the brain, it needs to be
225 established that this contrast contains meaningful clinical information, that can complement the
226 contrasts of R1 and R2*. For this aim, we evaluated the MRI contrast between pathological and
227 normal-appearing tissues of patients with meningioma brain tumors (N=18, **Figure 4a-b**). The
228 diagnosis of brain tumors and their delineation from the surrounding non-pathological tissue is
229 routinely performed using contrast-enhanced MRI, which requires the injection of an external
230 gadolinium (Gd)-based contrast agent with paramagnetic properties[54]. As expected, when using
231 Gd-based contrast, tumor tissue was distinct from white-matter and gray-matter tissues (**Figure**
232 **4c**, Cohen's d=1.4, $p<10^{-4}$ for tumor-gray matter; Cohen's d=1.18, $p<10^{-3}$ for tumor-white
233 matter). Recently renewed concerns about the long-term safety of Gd-based agents[55,56],
234 highlight the need for Gd-free MRI techniques that can serve as safe alternatives[57]. However,
235 without Gd-agent injection, both for R1 and R2* values the biggest effect size was observed
236 between white-matter and gray-matter tissues, with no significant difference between gray-
237 matter and tumor tissues (Cohen's d<0.45, p>0.08 for R1, Cohen's d<0.11, p>0.65 for R2*, **Figure**
238 **4d-e**). This demonstrates the poor performances of R1 and R2* in Gd-free tumor tissue
239 delineation. Importantly, the r1-r2* relaxivity greatly enhanced the contrast between tumor
240 tissue and non-pathological tissue, without contrast agent injection (**Figure 4f**, Cohen's d=1.5,
241 $p<10^{-5}$ for tumor-gray matter; Cohen's d=4.32, $p<10^{-11}$ for tumor-white matter). This Gd-free
242 enhancement was comparable in size to the effect of Gd-based contrast. Moreover, we provide
243 an example for a voxel-wise visualization of the r1-r2* relaxivity approach in a representative
244 meningioma patient, which demonstrates the Gd-free tumor enhancement (**Supplementary**
245 **Section 3: Voxel-wise r1-r2* relaxivity visualization**. These results emphasize the improved sensitivity
246 of the r1-r2* relaxivity to the unique tumor microenvironment, which may have wide clinical
247 implications as a safe alternative for contrast agents' injections.

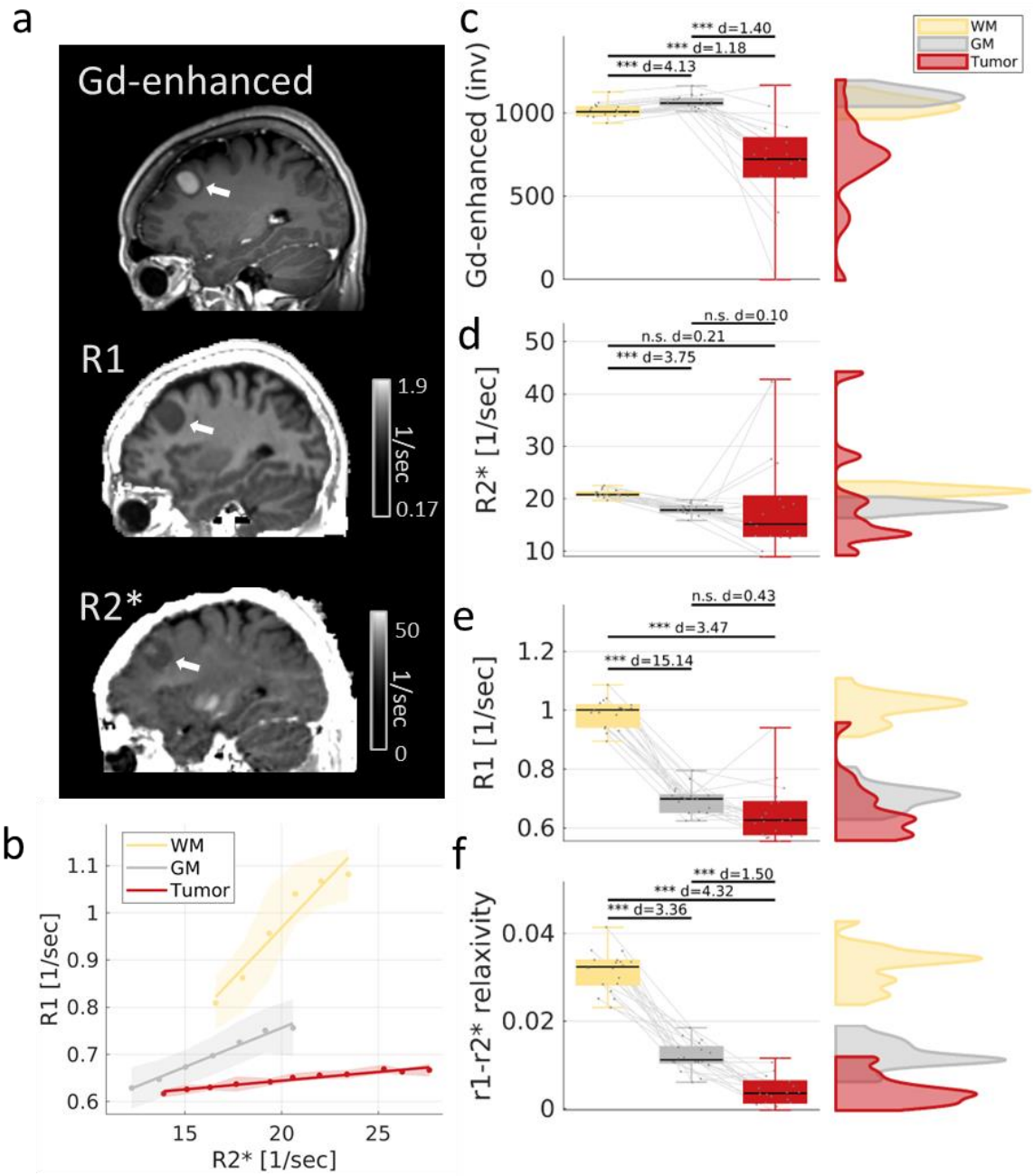

***Figure 4**: Application of the r1-r2* relaxivity on meningioma brain tumors. **(a)** From top to bottom: Gd-enhanced T1-weighted image, R1 map and R2* map in a representative subject with a meningioma brain tumor (white arrow). **(b)** The dependency of R1 on R2* (the r1-r2* relaxivity) for the white matter (WM, frontal), gray matter (GM, frontal) and tumor tissue of the same subject. Tumor tissue exhibits distinct r1-r2* relaxivity relative to non-pathological tissue, as evident by the slopes of the R1-R2* linear dependency. **(c-f)** The contrast between the white matter (WM), gray matter (GM) and tumor tissues across patients (N=18) for the Gd-enhanced contrast (inverted for visualization, a.u.) (c), R2* (d), R1 (e) and the r1-r2* relaxivity (f). Only the r1-r2* relaxivity produces significant differences between tumor and GM tissues without contrast agents. Left: boxes present the variation in the contrasts. The 25th, 50th and 75th percentiles and extreme data points are shown. The d-values represent the effect size (Cohen's d) of the differences between tissue types, and the significance level is based on a t-test. Gray lines extend between values of the same patient. Right: the distribution of the values between WM, GM and tumor tissue across patients. Estimates in non-pathological tissues are for the tumor-free hemisphere. p<0.05; **p<0.01; ***p<0.001*

248 ***The r1-r2* relaxivity is associated with unique biological pathways and gene expression profiles.***
249 To further examine how the tumor characteristics obtained by the r1-r2* relaxivity differ from
250 the information contained in R1 and R2*, we examined the associations of these *in vivo* MRI
251 measurements with underlying gene-expression profiles for the same tissue. To this end, we
252 analyzed cases in which the MRI scans of the meningioma patients were followed by surgical
253 interventions, to obtain matching resected tumor tissue samples that we profiled by bulk RNA-
254 sequencing (**Figure 5a**). For these tumor samples (N=17), we performed an unbiased analysis to
255 identify genes and molecular pathways that could be linked with the *in vivo* measured MRI
256 parameters. For each gene we calculated the correlation between the expression level and the *in*
257 *vivo* MRI measurements (r1-r2* relaxivity, R1 and R2*) across patients. We then performed gene
258 set enrichment analysis (GSEA)[58,59] to identify molecular functions that are significantly
259 associated with each MRI measurement. In total, we found 9, 55 and 59 significantly enriched
260 gene sets for R1, R2* and the r1-r2* relaxivity, respectively ($p<0.01$ after familywise error rate
261 (FWER) correction; **Sup. Table 1**). These gene sets define genes linked to a specific biological
262 pathway. Almost half of the significant gene sets were exclusively associated with the r1-r2*
263 relaxivity, and not with R1 or R2* (**Sup. Figure 16**). The enrichment score represents the degree to
264 which the genes within a set were positively or negatively correlated with MRI measurements. In
265 examining the associations of MRI measures to biological pathways, as reflected in the
266 enrichment score, we found that the r1-r2* relaxivity clustered separately from R1 and R2*
267 (**Figure 5b**). The clustering results were replicated when performed on the p-value of the
268 enrichment, or on the subset of genes within the top enrichment pathways. This implies that the
269 r1-r2* relaxivity reflects unique cellular and molecular properties, undetectable by the separate
270 analysis of R1 and R2*. Therefore, the *in vivo* r1-r2* relaxivity provides a unique dimension for
271 measuring microstructure and gene expression features across the brain. The gene enrichment
272 analysis that we performed on resected brain tumors (**Figure 5b**) can provide insights into the
273 biological pathways associated with the r1-r2* relaxivity. The two most enriched pathways for
274 the r1-r2* relaxivity were "immunoglobulin complex" (normalized enrichment score (NES)= -
275 3.62, FWER p-value<0.001; **Sup. Figure 17a**) and "scavenging of heme from plasma" (NES= -3.27,

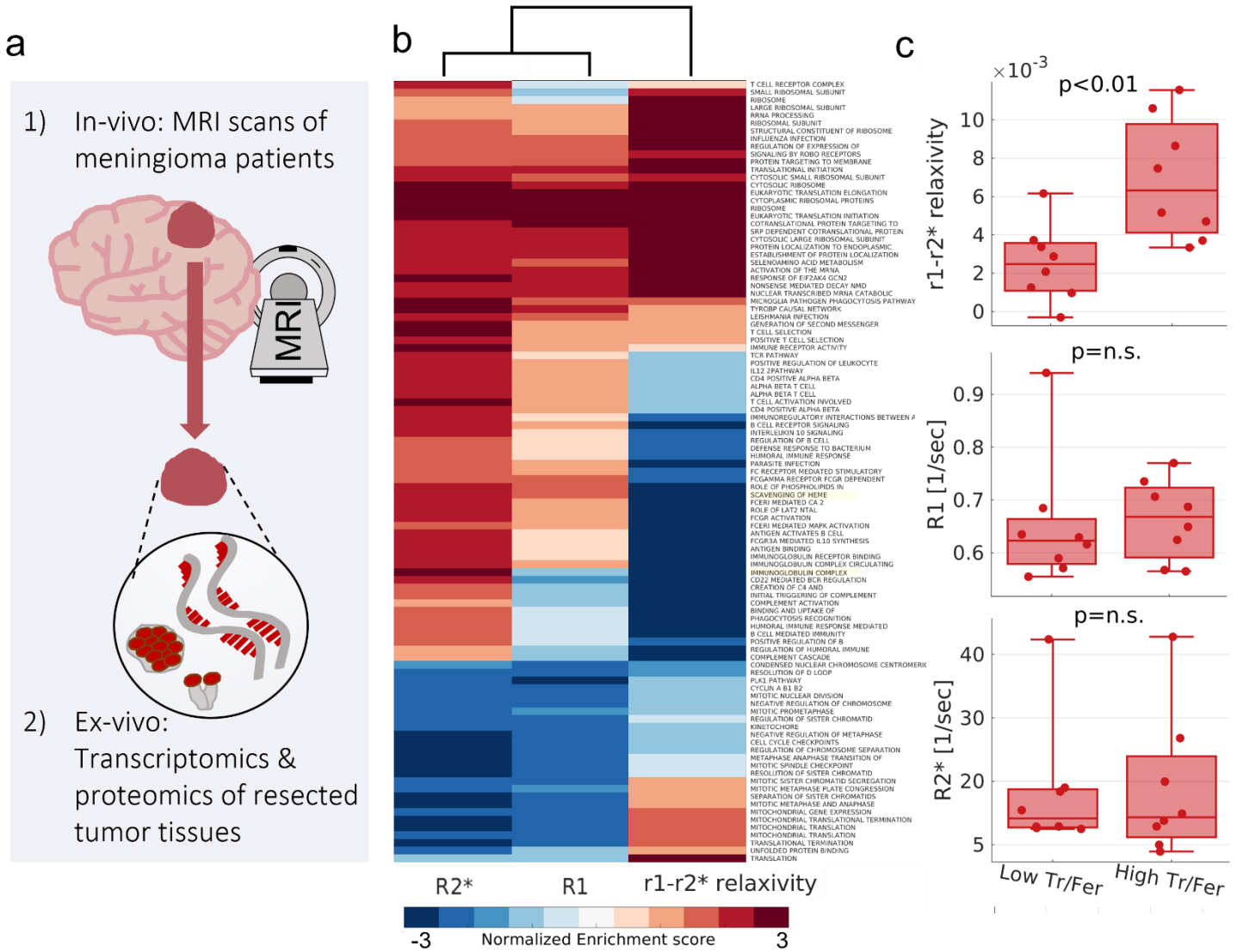

Figure 5: The r1-r2 relaxivity measured in vivo in meningioma patients agrees with iron homeostasis markers estimated* ex vivo *on surgical specimens of meningiomas from the same patients. (a) Unique comparison between qMRI parameters measured in vivo to* ex vivo *iron histology of the same human tissue; MRI scans of meningioma patients (N=17) were followed by surgical interventions, to obtain matching resected tumor tissue samples. These tissue samples were profiled by bulk RNA-sequencing to obtain gene expression profiles, and by western-blot analysis to estimate the transferrin/ferritin ratio, a marker for iron homeostasis. (b) Gene set enrichment analysis for the correlation of MRI with gene expression. Rows show significant biological pathways, columns represent R1, R2* and the r1-r2* relaxivity. The dendrogram shows hierarchical clustering of the normalized enrichment scores. The r1-r2* relaxivity clustered separately from R1 and R2* and is therefore enriched for unique biological pathways. The two most enriched pathways for the r1-r2* relaxivity are highlighted in yellow. (c) The r1-r2* relaxivity, R1 and R2* measured in vivo for tumor tissues (N=16) classified as having either low or high transferrin-to-ferritin ratios (Tf/Fer). Tf/Fer ratio, an iron homeostasis marker, was estimated using western-blot analysis following surgical resection of the tissue. The threshold between groups was set to 1 based on the median across subjects. While R1 and R2* cannot distinguish between the groups with different Tf/Fer ratios, the r1-r2* relaxivity is higher in tissues with a high Tf/Fer ratio, indicating its sensitivity to iron homeostasis. p-values presented are for two-sample t-tests .*

276 FWER p-value<0.001; **Sup. Figure 17b**). While the former may relate to the response of the
277 immune system to the cancerous process[60,61], the latter involves the absorption of free heme, a
278 source of redox-active iron[62]. This iron-related pathway was not significantly associated with R1
279 or R2* (p>0.01). Moreover, we examined the main genes involved in iron regulation: transferrin
280 receptor (TFRC), ferritin heavy-chain polypeptide 1 (FTH1) and ferritin light-chain polypeptide
281 (FTL)[63,64]. Both TFRC and FTH1 were included in the subset of genes within the top enrichment
282 pathways for the r1-r2* relaxivity, but were not found to be associated with R1 or R2*. These
283 findings provide evidence at the level of gene-expression for the sensitivity of the r1-r2*
284 relaxivity to iron homeostasis.

285 ***The r1-r2* relaxivity reveals differences in iron homeostasis between tumor tissues.***
286 We further validated the sensitivity of the r1-r2* relaxivity to iron homeostasis at the proteomics
287 level, by comparing *in vivo* MRI measurements to ex vivo iron homeostasis estimation on the
288 same tissue (**Figure 5a)**. MRI scans of the meningioma patients were followed by surgical
289 interventions, to obtain matching resected tumor tissue samples that we analyzed by western-
290 blot. We compared *in vivo* MRI values of tumor tissue to its transferrin/ferritin ratio which serves
291 as a proxy for iron homeostasis. Neither R1 nor R2* showed significant differences between
292 tumors with low and high transferrin/ferritin ratios (**Figure 5c**). Notably, the r1-r2* relaxivity was
293 significantly higher for tumors with high transferrin/ferritin ratio compared to tumors with low
294 transferrin/ferritin ratio (p<0.01, **Figure 5c**). Therefore, as established by both gene expression
295 and proteomics analyses, the r1-r2* relaxivity measured *in vivo* detects pathological disruptions
296 in iron homeostasis which were previously only observable ex vivo.

297 Discussion

298 We present a new MRI relaxivity approach, with increased sensitivity to different molecular
299 environments of iron. First, we confirm *in vitro* that different iron environments induce different
300 relaxivities, which can be estimated with MRI using the r1-r2* relaxivity. When examining R1 and
301 R2* of different iron environments, we find the molecular state of iron is confounded by the
302 strong effects of iron and myelin concentrations. In this *in vitro* setting, we show that the r1-r2*
303 relaxivity reveals the sensitivity of MRI to the intrinsic paramagnetic properties of different iron

304 environments. In the healthy human brain, we show that the r1-r2* relaxivity provides a unique
305 MRI contrast. This contrast is less sensitive to myelin compared to other quantitative MRI
306 parameters. Interestingly, it does vary with an iron homeostasis marker[7] across brain regions and
307 age groups. We further demonstrate that the r1-r2* relaxivity contains meaningful clinical
308 information associated with iron homeostasis, which was previously inaccessible to conventional
309 MRI approaches. In meningioma patients, we find that the r1-r2* relaxivity contrast is useful for
310 enhancing the distinction between tumor tissue and non-pathological tissue. We substantiate
311 this finding by associating *in vivo* MRI measurements with RNA sequencing and protein
312 expression levels of the same tumor tissues. We find that the r1-r2* relaxivity is associated with
313 unique iron-related biological pathways and reveals the state of iron homeostasis in tumors.

314 Relaxivity commonly is employed to characterize MR contrast agents[65]. While most contrast
315 agents induce relaxation based on their paramagnetic or superparamagnetic properties, some
316 agents elevate the R1 relaxation rate more efficiently while others elevate R2*. R1 relaxation
317 mechanisms are affected by local molecular interactions, while R2* is sensitive to more global
318 effects of extended paramagnetic interactions at the mesoscopic scale[37]. We show that by
319 contrasting these two different mechanisms, we gain sensitivity to the endogenous iron
320 environment, without the injection of an external contrast agent.

321 The concept of iron relaxivity, and its sensitivity to the molecular environment of iron, was
322 previously suggested by several postmortem and *in vitro* studies[31–35]. We reproduce these
323 results in our *in vitro* experiments and further demonstrate that different iron environments
324 have different iron relaxivities. Moreover, Ogg et al.[31] calculated the iron relaxivity by comparing
325 postmortem measurements of iron concentration for different age groups to the typical R1
326 values in those age groups. They found that this approximation of iron relaxivity was higher in
327 the gray matter and white matter than in sub-cortical structures. Remarkably, we replicate this
328 result in living subjects, based on our novel approach for estimating the iron relaxivity *in vivo*.
329 The theoretical derivation we propose for the r1-r2* relaxivity shows that it represents the ratio
330 of the iron relaxivities of R1 and R2*. This theory was supported by our *in vitro* experiments. To
331 account for the complex molecular environment of the brain, we expanded the biophysical
332 model of the r1-r2* relaxivity for the case of a heterogenous iron environment and in the

333 presence of myelin. Numerical simulations of this model under physiological conditions
334 demonstrate that variations in the iron environment change the r1-r2* relaxivity considerably.
335 Therefore, we exploit the different relaxation rates for a biophysical model of their linear
336 interdependency, thus allowing to approximate the iron relaxivity in the living brain for the first
337 time.

338 First, we evaluated the sensitivity of the r1-r2* relaxivity to the molecular environment of iron
339 based on *in vitro* experiments with ferritin, transferrin and ferrous iron. We show that these iron
340 environments induce different relaxivities, even when accounting for the discrepancies in iron-
341 binding. Moreover, we show that the macromolecular environment in which the iron reside can
342 alter the relaxivity as well. For example, ferritin induces different relaxivities in the presence of
343 liposomes, proteins or when it is free. As implied previously[32], this effect can be explained by the
344 encapsulation and the spatial distribution of paramagnetic molecules. Therefore, similarly to
345 different contrast agents, the physical mechanisms by which iron compounds interact with the
346 surrounding water environment are inherently different. To further confirm that our results are
347 related to paramagnetic properties and not the presence of the proteins themself, we tested
348 MRI measurements of apo-transferrin (transferrin unbound to iron). In this case, the R1 relaxivity
349 of transferrin vanished. Therefore, the presence of iron in different *in vitro* environments can be
350 detected by the r1-r2* relaxivity. Moreover, evaluating ferritin-transferrin mixtures, we find that
351 in heterogenous iron environments the specific composition of the iron milieu affects the r1-r2*
352 relaxivity.

353 The biological interpretation of the r1-r2* relaxivity measurement is more ambiguous when
354 applied to the *in vivo* human brain. This is due to the fact that most qMRI parameters, including
355 R1 and R2*, are known to suffer from low biological specificity in the brain[4,19,25,29,40–42]. The
356 primary MRI contrast between gray matter and white matter usually is associated with myelin,
357 while an additional and often correlated effect is attributed to the iron concentration[4].

358 A major strength of our relaxivity approach is that it captures new biological and pathological
359 information, not acquired by traditional qMRI parameters such as R1 and R2*. We show that the
360 great contrast between white matter and gray matter usually observed in R1 and R2* is no

361 longer as substantial in the r1-r2* relaxivity. *In vitro*, we show that the r1-r2* relaxivity is stable
362 across iron and liposomal concentrations. To farther demonstrate the minimal effect of myelin
363 on the r1-r2* relaxivity in the brain , we employed the qMRI measurements of MTV[46], MTsat[47]
364 and MD, which were shown to approximate the myelin content[48–53]. These *in vivo* myelin
365 markers are all highly correlated with R1 and R2* but not with the r1-r2* relaxivity. Adapting the
366 biophysical model for the r1-r2* relaxivity to account for myelin (**Supplementary Section 4.3:**
367 **Numerical simulations of the r1-r2* relaxivity.**), we find that the variability in myelin within an ROI
368 can still affect the r1-r2* relaxivity measurement. Yet, *in vivo* estimate of the myelin variability
369 only explains ~30% of the variation in the *in vivo* r1-r2* relaxivity across the brain. In brain tissue
370 numerical simulations, we show that the myelin content substantially affects the measurements
371 of R1 and R2*, but it cannot by itself explain the measured variability in the r1-r2* relaxivity
372 across the brain (**Supplementary Section 4.3: Numerical simulations of the r1-r2* relaxivity.**).
373 Nonetheless, it could be that the r1-r2* relaxivity contains some residual contribution of the
374 myelin content. Yet, we show that this contribution is much more limited compared to
375 traditional qMRI parameters such as R1 and R2*. In return, the novel MRI measurement of the
376 r1-r2* relaxivity enhances the contrast between pathological tissue and normal tissue and is
377 associated with distinct gene expression pathways. Hence, the relaxivity framework reveals
378 distinct biological features otherwise undetectable in standard qMRI measurements.

379 Still, an open question remains whether the biological interpretation of the r1-r2* relaxivity
380 demonstrated *in vitro* is also measurable *in vivo*. We bring several evidence that the r1-r2*
381 relaxivity reveals the sensitivity of MRI to properties of the molecular iron environment,
382 otherwise confounded by myelin and iron concentrations. First, in the healthy and aging brain
383 we show that unlike R1 and R2*, the r1-r2* relaxivity is correlated with an iron homeostasis
384 marker, the iron mobilization capacity (the transferrin/iron ratio). We also show that the r1-r2*
385 relaxivity is less correlated with the absolute ferritin, transferrin or iron concentrations,
386 indicating that it enhances the sensitivity to the homeostasis between iron compounds, rather
387 than their absolute concentrations. Importantly, we corroborate these findings based on *in vivo*
388 and *ex vivo* analyses of meningioma patients. We find that the variability in the *in vivo* r1-r2*
389 relaxivity of brain tumors is explained by their transferrin-ferritin ratios and is associated with

390 iron-related genes. These results could not be obtained for the individual measurements of R1
391 and R2*. To further validate that the r1-r2* relaxivity could be sensitive to the iron homeostasis,
392 even when accounting for the massive effect of the myelin and iron concentrations on the MRI
393 signal, we generated a simulation of a brain-like environment which contains multiple tissue
394 components (**Supplementary Section 4.3: Numerical simulations of the r1-r2* relaxivity**.). We provide
395 an example for physiological changes in the iron environment, based on the ferritin-transferrin
396 fraction, which could lead to considerable changes in the r1-r2* relaxivity, well above the
397 detection limit of this MRI measurement. Therefore, we show *in vitro*, *in vivo*, ex vivo and in
398 numerical simulations, that the r1-r2* relaxivity measurement could allow to detect changes in
399 the iron homeostasis under physiological conditions.

400 Our *in vitro* experiments are based on ferritin, transferrin and ferrous iron as examples for
401 variable iron environments. Yet, in the human brain our approach is probably more broadly
402 sensitive to the entire milieu of iron compounds, their iron binding characteristics and
403 aggregation states. Other iron compounds that exist in the brain, such as hemoglobin,
404 hemosiderin, neuromelanin, magnetite, ferric ion, lactoferrin and melanotransferrin [4], might
405 have distinct iron relaxivities as well. Moreover, other characteristics of the iron environment
406 such as iron compounds' aggregate sizes, intra-aggregate spacing, spatial distributions and iron
407 loadings, could all have an additional effect on the iron relaxivity[35]. For example, catecholamine
408 neurons of the substantia nigra and locus coeruleus are rich in neuromelanin-iron complexes[4,66]
409 which could contribute to the r1-r2* relaxivity measurement in these regions (see also
410 **Supplementary Section 5: The r1-r2* relaxivity in the pallidum**.). In addition, the paramagnetic
411 properties of deoxyhemoglobin in capillaries and veins and their orientations are known to affect
412 the R2* measurement[67–69]. Thus, the r1-r2* relaxivity might also be sensitive to the iron
413 environment in the vascular system, which is crucial for brain iron metabolism and
414 homeostasis[70]. Moreover, on the cellular scale there is substantial heterogeneity in the iron
415 environment[71,72]. R1 and R2* each represent some average of different spatial and cellular
416 compartments, but it is unclear how the r1-r2* relaxivity is weighting such cellular contributions.
417 Last, similar to the measurements of R1 and R2*, the r1-r2* relaxivity might be contaminated by
418 biases related to magnetic field inhomogeneities[23]. Yet, we show that the r1-r2* relaxivity is

419 reproducible in scan-rescan experiments (both *in vitro* and *in vivo*) and is stable across subject,
420 thus indicating the limited effect of such biases. To conclude, while we demonstrate our
421 approach *in vitro* based on ferritin, transferrin and ferrous iron samples, we believe that in the
422 human brain the r1-r2* relaxivity provides more comprehensive information on the molecular
423 iron milieu previously inaccessible by MRI.

424 In order to further model the separate contributions to the MRI signal of different iron
425 compounds, it would be necessary to increase the dimensionality of the *in vivo* iron relaxivity
426 measurement. In addition to R1 and R2*, other qMRI parameters known to be sensitive to iron
427 include quantitative susceptibility mapping (QSM) and R2[3,4]. In addition, it was suggested that
428 magnetization transfer (MT) measurements are affected by neuromelanin-iron complexes[12,73].
429 The linear interdependencies of these other iron-related MRI measurements may uncover
430 additional features of the iron environment[74]. Therefore, we speculate that the concept we
431 introduce here, of exposing the iron relaxivities *in vivo* based on the linear dependency of R1 on
432 R2* (the r1-r2* relaxivity), can be generalized to further increase MRI's specificity for iron using
433 additional complementary measurements. For example, in a previous work we implemented a
434 different aspect of relaxivity for the detection of lipid composition, based on the linear
435 dependency of qMRI parameters on the macromolecular tissue volume (MTV)[46]. Here, we
436 demonstrate that the r1-r2* relaxivity and the dependency of R1 on MTV provide two
437 orthogonal microstructural axes (**Supplementary Section 2: The dependency of the iron relaxivity on**
438 **the liposomal fraction.**). The dependency of R1 on MTV changes according to the lipid types, even
439 in the presence of iron, while the r1-r2* relaxivity is insensitive to the lipid types and provides
440 better distinctions between iron environments. Therefore, the presented framework can be
441 generalized further to boost MRI's specificity and support a more comprehensive *in vivo*
442 histology with qMRI.

443 While the field of *in vivo* histology with MRI is rapidly growing, ground-truth validation remains a
444 great challenge. Here we propose a cutting-edge validation strategy combining both bottom-up
445 and top-down approaches in which we incorporate *in vitro*, *in vivo* and ex vivo analyses. For the
446 bottom-up analysis, we developed a unique, synthetic biological system that allows us to
447 examine the biophysical interpretation of the r1-r2* relaxivity in highly controlled *in vitro*

448 settings. For the top-down analysis, we tested whether our interpretation remains valid in the
449 context of the extremely complex biological tissue. We compared the r1-r2* relaxivity measured
450 *in vivo* to histological measurements of iron homeostasis and gene expression. This comparison
451 was done both at the group level, based on previously reported findings, and at the single-
452 subject level, by analyzing resected tumor tissues. To our knowledge, this is the first time that
453 qMRI parameters measured *in vivo* have been compared to ex vivo iron histology and gene
454 expression of the same human tissue. Taken together, the different validation strategies all
455 indicate that the r1-r2* relaxivity increases the specificity of MRI to different molecular
456 environments of iron, highlighting the robustness of our findings.

457 Our proposed approach for measuring iron homeostasis *in vivo* using the r1-r2* relaxivity may
458 have wide clinical and scientific implications. First, the r1-r2* relaxivity provides a new contrast
459 for imaging the brain, which is associated with 45 distinct gene sets, not associated with R1 or
460 R2* by themselves. Moreover, we show that the r1-r2* relaxivity, which captures paramagnetic
461 properties, enhances the contrast between tumor tissue and normal-appearing white-matter
462 and gray-matter tissues. In agreement with these findings, meningioma tumors have been
463 shown to contain a higher concentration of ferrimagnetic particles and an abnormal expression
464 of iron-related genes compared to non-pathological brain tissue[17,18]. Indeed, the contrast
465 enhancement we saw with the r1-r2* relaxivity is similar to the one observed for Gd-enhanced
466 imaging, which is based on the altered relaxivity in the presence of paramagnetic agents[75].
467 Concerns regarding the safety of Gd-based contrast agents raise the need for Gd-free diagnosis
468 of brain tumors[55,56]. Adjusting our approach for clinical imaging might offer safer alternatives for
469 brain tumor diagnosis.

470 Finally, the sensitivity of the r1-r2* relaxivity to iron homeostasis in the brain may have clinical
471 implications for neurodegenerative diseases. Alterations in the distribution of molecular iron
472 compounds can lead to cellular damage which is disease-specific[10]. In particular, the iron
473 mobilization capacity was shown to differ between elderly controls and patients diagnosed with
474 either Parkinson's disease (PD) or Alzheimer's disease (AD)[7]. We found that this iron homeostasis
475 marker is correlated with the r1-r2* relaxivity across brain regions and age groups. This result, in
476 addition to our other validation strategies, demonstrate the sensitivity of the r1-r2* relaxivity to

477 the iron homeostasis in the brain and in the aging process. Therefore, our approach can add a
478 new important layer of information to existing *in vivo* PD and AD biomarkers such as
479 neuromelanin MRI[12] and may further advance the research, diagnosis and treatment of
480 neurodegenerative diseases[1,2,5–9].

481 Conclusion:

482 We present a novel MRI contrast, based on the r1-r2* relaxivity, which is sensitive to the iron
483 homeostasis in the human brain. This new technology can differentiate between tumor tissue
484 and non-pathological tissue without injecting contrast agents, and can detect biological
485 properties inaccessible to conventional MRI approaches. We validated the sensitivity of the r1-
486 r2* relaxivity to the molecular state of iron using *in vitro*, *in vivo* and ex vivo analyses. We show
487 that our MRI technology reveals the intrinsic paramagnetic properties of different *in vitro* iron
488 environments. Furthermore, the r1-r2* relaxivity varies with the iron mobilization capacity
489 across brain regions and age groups, and reveals differences in iron homeostasis and iron-related
490 gene expression in pathological tissues. Therefore, this approach may further advance our
491 understanding of the impaired iron homeostasis in cancer, normal aging and neurodegenerative
492 diseases, and may open new avenues for the non-invasive research and diagnosis of the living
493 human brain.

494 Methods:

495 *In vivo iron relaxivity model*:
496 The iron relaxivity model assumes a linear relationship between relaxation rates and iron
497 concentration[31–34].
498 This linear relationship for two different iron environments *a* and *b* with iron concentrations [a]
499 and [b] can be expressed using the following equations:

500 $$(1)\ R_1 = r_{(1,a)}[a] + c_{(1,a)} \qquad R_1 = r_{(1,b)}[b] + c_{(1,b)}$$
501 $$(2)\ R_2^* = r_{(2,a)}[a] + c_{(2,a)} \qquad R_2^* = r_{(2,b)}[b] + c_{(2,b)}$$

502 where $r_{(1/2,a/b)}$ represents the R1-iron relaxivity or the R2*-iron relaxivity of the two iron
503 environments, and $c_{(1/2,a/b)}$ are constants.
504 The two iron environments are distinguished by their iron relaxivities under the assumption:

$$(3)\ r_{(1,a)} \neq r_{(1,b)} \qquad and/or \qquad r_{(2,a)} \neq r_{(2,b)}$$

Rearranging Eq. 2:

$$(4)\ [a] = \frac{R_2^* - c_{(2,a)}}{r_{(2,a)}} \qquad [b] = \frac{R_2^* - c_{(2,b)}}{r_{(2,b)}}$$

Substituting Eq. 4 in Eq. 1:

$$(5)\ R_1 = \frac{r_{(1,a)}}{r_{(2,a)}} R_2^* + const \qquad R_1 = \frac{r_{(1,b)}}{r_{(2,b)}} R_2^* + const$$

where $\frac{r_{(1,a)}}{r_{(2,a)}}$ and $\frac{r_{(1,b)}}{r_{(2,b)}}$ represent the linear dependencies of R1 on R2* (r1-r2* relaxivities) of the two iron environments *a* and *b*. Importantly, the MRI-measured r1-r2* relaxivity serves as an *in vivo* estimator of iron relaxivity and reveals intrinsic properties of the iron environment. Assuming that the iron relaxivity of R1 provides a different separation between the two iron environments *a* and *b* compared to the iron relaxivity of R2*:

$$\frac{r_{(1,a)}}{r_{(2,a)}} \neq \frac{r_{(1,b)}}{r_{(2,b)}}$$

These two iron environments *a* and *b* then can be distinguished by their r1-r2* relaxivities (i.e., the *in vivo* iron relaxivity). In the brain, the r1-r2* relaxivity could be affected by the entire milieu of available iron compounds, their iron binding capacities and aggregation states (i.e. the molecular iron environment). For an elaboration of this model under the assumption of a complex iron environment and in the presence of myelin see Supplementary Section 4: Exploring the biophysical sources of the r1-r2* relaxivity.

Phantom samples experiments:

Phantom system:

We prepared samples of four different iron compounds: transferrin (holo-transferrin human, Sigma), apo-transferrin (apo-transferrin human, Sigma), ferritin (equine spleen, Sigma), and ferrous (iron (II) sulfate heptahydrate, Sigma). These samples were prepared in three different molecular environments: liposomes, 18.2 MΩ-cm water, and bovine serum albumin (BSA, Sigma)[76,77]. For each combination of iron compound and molecular environment, we made different samples by varying both the iron compound concentration and the lipid/BSA-water fractions. For liposomal/BSA environments, the iron compounds concentrations were divided by the water-lipid or water-BSA fractions to get units of [mg/wet ml]. The liposomes were made from a mixture of soy phosphatidylcholine (PC) and egg sphingomyelin (SM) purchased from Lipoid and used without further purification. Additional results with PC and PC-cholesterol (Sigma) liposomes are presented in Sup. Section 2. The lipid samples were mixed in chloroform at

535 desired mole ratios and evaporated under reduced pressure (8 mbar) in a Buchi rotary
536 evaporator vacuum system (Flawil, Switzerland). The resulting lipid film was resuspended in a 10
537 mM ammonium bicarbonate solution, lyophilized, and subsequently hydrated in the reassembly
538 buffer. To achieve the desired lipid-protein concentration, the protein solution (~50 mg/ml in
539 water) was diluted to the right concentration and subsequently was added to the lyophilized
540 lipid powder. For the BSA phantoms, samples were prepared by dissolving lyophilized BSA in 18.2
541 MΩ-cm water at the desired concentrations.

542 Samples were placed in a 2-ml glass vials glued to a glass box, which was then filled with ~1%
543 SeaKem® LE Agarose (Ornat) and 0.1% gadolinium (Gadoteric acid (Dotarem, Guerbet)) dissolved
544 in distilled water (DW). The purpose of the agarose with gadolinium (Agar-Gd) was to stabilize
545 the vials and to create a smooth area in the space surrounding the samples that minimalized air-
546 sample interfaces.

547 MRI acquisition for phantoms:
548 Data were collected on a 3T Siemens MAGNETOM Skyra scanner equipped with a 32-channel
549 head receive-only coil at the ELSC Neuroimaging Unit at the Hebrew University.

550 *Quantitative R1 & MTV:* 3D Spoiled gradient echo (SPGR) images were acquired with different
551 flip angles (FA = 4°, 8°, 16°, and 30°). The TE/TR were 4.45/18 ms. The scan resolution was 0.5
552 mm x 0.5 mm x 0.6 mm. For calibration, we acquired an additional spin-echo inversion recovery
553 (SEIR) scan. This scan was done on a single slice, with an adiabatic inversion pulse and inversion
554 times of TI = 2,000, 1,200, 800, 400, and 50 ms. The TE/TR were 73/2,540 ms. The scan
555 resolution was 1.2 mm x 1.2 mm x 2.0 mm.

556 *Quantitative R2*:* SPGR images were acquired with different flip angles (α = 4°, 8°, 16°, and 30°).
557 The TR was 27 ms and 5 echoes were equally spaced between 4.45 and 20.85 ms. The scan
558 resolution was 0.5 mm x 0.5 mm x 0.6 mm.

559 Estimation of qMRI parameters for phantoms:
560 *Quantitative R1 & MTV mapping:* R1 and MTV estimations for the lipid samples were computed
561 with the mrQ [46] (https://github.com/mezera/mrQ) and Vista Lab
562 (https://github.com/vistalab/vistasoft/wiki) software packages. The mrQ software was modified
563 to suit the phantom system[77]. The modification utilizes the fact that the Agar-Gd mixture which
564 fills the box around the vials is homogeneous, and therefore can be assumed to have a constant
565 R1 value. We used this gold-standard R1 value generated from the SEIR scan to correct for the
566 excite bias in the SPGR scans.

567 A mask labeling the different phantom samples was generated based on MATLAB's
568 "imfindcircles" function, and was filtered to remove voxels with extremely high and low signals.
569 Voxels were filtered based on a fixed threshold on the SPGR signal at FA=16. In addition, we also

filtered out those voxels in which the SPGR signal at FA=16 was two median absolute deviations away from the median value. We further edited this mask manually, removing voxels with susceptibility artifacts resulting from the vials and air pockets. To fit the R1 and proton density of each phantom sample, we calculated the median values of the SPGR signal as well as the excite and receive biases across all the voxels of each sample. These median values were used in the Vista Lab function "relaxFitT1" to find the median R1 and proton density of each sample. proton density values then were calibrated using the proton density of a water-filled vial in order to calculate the MTV values.

Quantitative R2 mapping:* We used the SPGR scans with multiple echoes to estimate R2*. Fitting was done by taking the median values of the SPGR signal across all the voxels of the phantom sample for each TE. To label the different samples, we used the same mask that was used to calculate R1 and MTV. We then used an exponential fitting process to find R2*. As we had four SPGR scans with variable flip angles, we averaged the R2* values acquired from each of these scans for increased signal to noise ratio.

r1-r2* relaxivity computation for phantoms:

For each iron compound in each molecular environment, we computed the linear dependency of R1 on R2* across samples with varying iron-binding proteins concentrations relative to the water fractions. We fitted the following linear model across samples:

$$R1 = a * R2^{*} + b$$

The slope of this linear model (a) represents the r1-r2* relaxivity. b is constant. This process was implemented in MATLAB.

Estimation of total iron content in phantoms:

We estimated the iron content of our transferrin and ferritin samples using the following equation:

$$iron\ \left(\frac{mg}{ml}\right) = \frac{iron\ binding\ protein\ \left(\frac{mg}{ml}\right)}{protein\ molecular\ weight\ \left(\frac{mg}{mol}\right)} * \frac{iron\ ions}{protein} * iron\ molecular\ weight\ \left(\frac{mg}{mol}\right)$$

Transferrin contains 2 iron ions per protein molecule[3], and its molecular weight was estimated as $76*10^{6}$ mg/mol (based on manufacturer information). The iron loading of ferritin was estimated as 2,250 iron ions per protein molecule (based on manufacturer information) and its molecular weight was estimated as $440*10^{6}$ mg/mol[3]. The molecular weight of iron was set to $55.847*10^{3}$ mg/mol.

This resulted in the following equation for converting iron-binding protein concentrations into iron concentrations:

1 mg/ml transferrin = 1.4 µg/ml iron

1 mg/ml ferritin = 0.29 mg/ml iron

605 MRI human dataset:

606 Healthy Human subjects:
607 We scanned 26 young adults (aged 27 ± 10 years, 10 females), and 13 older adults (aged 70 ± 3
608 years, 4 females). Healthy volunteers were recruited from the community surrounding the
609 Hebrew University of Jerusalem. The experimental procedure was approved by the Helsinki
610 Ethics Committee of Hadassah Hospital, Jerusalem, Israel. Written informed consent was
611 obtained from each participant prior to the procedure. This data was first used in our previous
612 work[76].

613 Meningioma patients:
614 During the study period May 2019 to August 2020, we recruited 19 patients who had undergone
615 surgery for the resection of brain meningiomas. All patients had preoperative qMRI scans in
616 addition to their clinical brain MRI assessment. One subject, with a titanium cranial fixation plate
617 adjacent to the tumor, was excluded from the study due to local disruption of the magnetic field.
618 The final cohort included 18 patients (11 females). Imaging studies were anonymized before they
619 were transferred for further analysis. Brain meningioma surgical specimens, available for 16
620 patients, were obtained from the fresh frozen tissue biobank of the Department of
621 Neurosurgery, Shaare Zedek Medical Center, Jerusalem, Israel, and were transferred on dry ice
622 for western-blot and gene expression analyses. Study participants provided informed consent
623 according to an institutional review board.

624 MRI acquisition for healthy human subjects:
625 Data were collected on a 3T Siemens MAGNETOM Skyra scanner equipped with a 32-channel
626 head receive-only coil at the ELSC Neuroimaging Unit at the Hebrew University.

627 *Quantitative R1, R2* & MTV mapping:* SPGR echo images were acquired with different flip angles
628 (α = 4°, 10°, 20° and 30°). Each image included 5 equally spaced echoes (TE=3.34-14.02 ms) and
629 the TR was 19 ms. The scan resolution was 1 mm isotropic. Additional SPGR echo image was
630 acquired with an MT pulse (TE=3.34, TR=27, α = 10, 1 mm isotropic). For calibration, we acquired
631 an additional spin-echo inversion recovery scan with an echo-planar imaging read-out (SEIR-epi).
632 This scan was done with a slab-inversion pulse and spatial-spectral fat suppression. For SEIR-epi,
633 the TE/TR were 49/2,920 ms. The TIs were 200, 400, 1,200, and 2,400 ms. We used 2-mm in-
634 plane resolution with a slice thickness of 3 mm. The EPI readout was performed using 2×
635 acceleration.

636 *Anatomical images:* 3D magnetization-prepared rapid gradient echo (MP-RAGE) scans were
637 acquired for 30 of the 39 healthy subjects. The scan resolution was 1 mm isotropic, the TE/TR
638 were 2.98/2,300 ms. Magnetization-prepared 2 rapid acquisition gradient echo (MP2RAGE)
639 scans were acquired for the remaining 9 subjects. The scan resolution was 1 mm isotropic, the
640 TE/TR were 2.98/5,000 ms.

641 *Whole-brain DTI measurements:* performed using a diffusion-weighted spin-echo EPI sequence
642 with isotropic 1.5-mm resolution. Diffusion weighting gradients were applied at 64 directions
643 and the strength of the diffusion weighting was set to b = 2000 s/mm2 (TE/TR=95.80/6,000 ms,
644 G=45 mT/m, δ=32.25 ms, Δ=52.02 ms). The data includes eight non-diffusion-weighted images
645 (*b* = 0). In addition, we collected non-diffusion-weighted images with reversed phase-encode
646 blips. For two subjects (1 young, 1 old) we failed to acquire this correction data and they were
647 excluded from the diffusion analysis.

648 MRI acquisition for meningioma patients:
649 Data were collected on a 3T Siemens MAGNETOM Skyra scanner equipped with a 32-channel
650 head receive-only coil at the Shaare Zedek Medical Center.

651 *Quantitative R1, R2* & MTV mapping:* SPGR echo images were acquired with different flip angles
652 (α = 4°, 10°, 20° and 30°). Each image included 5 equally spaced echoes (TE=2.85-14.02 ms) and
653 the TR was 18 ms. The scan resolution was 1.5 mm isotropic. For calibration, we acquired an
654 additional SEIR-epi scan. This scan was done with a slab-inversion pulse and spatial-spectral fat
655 suppression. For SEIR-epi, the TE/TR were 49/2,920 ms. The TIs were 200, 400, 1,200, and 2,400
656 ms. We used 2-mm in-plane resolution with a slice thickness of 3 mm. The EPI readout was
657 performed using 2× acceleration.

658 *Gd-enhanced anatomical images:* Gd-enhanced MPRAGE scans were acquired. The scan
659 resolution was 1 mm isotropic, the TE/TR were 2.4/1,800 ms. The contrast agent was either
660 Multihance or Dotarem at a dose of 0.1 mmol/kg. Contrast agent injection and MPRAGE
661 acquisition were done after the acquisition of the quantitative MRI protocol, or on a different
662 day.

663 Estimation of qMRI parameters for human subjects:
664 *Quantitative R1 & MTV mapping:* Whole-brain MTV and R1 maps, together with bias correction
665 maps of B1+ and B1-, were computed using the mrQ software[46,78].

666 *Quantitative R2* mapping:* We used the SPGR scans with multiple echoes to estimate R2*.
667 Fitting was performed with the MPM toolbox[79]. As we had four SPGR scans with variable flip
668 angles, we averaged the R2* maps acquired from each of these scans for increased SNR.

669 *Quantitative MD mapping:* Diffusion analysis was done using the FDT toolbox in FSL [80,81].
670 Susceptibility and eddy current induced distortions were corrected using the reverse phase-
671 encode data, with the eddy and topup commands[82,83]. MD maps were calculated using vistasoft
672 (https://github.com/vistalab/vistasoft/wiki).

673 *Quantitative MTsat mapping:* MTsat maps were computed as described in Helms et al. (2008)[47].

674 The MTsat measurement was extracted from equation:

675 $$MTsat = M_0 B1\alpha \frac{R1TR}{S_{MT}} - \frac{(B1\alpha)^2}{2} - R1TR$$

676 Where S_{MT} is the signal of the SPGR scan with additional MT pulse, α is the flip angle and TR is
677 the repetition time. M_0 (the equilibrium magnetization parameter), $B1$ (the transmit
678 inhomogeneity) and $R1$ estimations were computed from the non-MT weighted SPGR scans,
679 during the pipeline described under "*Quantitative R1 & MTV mapping*". Registration of the
680 S_{MT} image to the imaging space of the R1 map was done using a rigid-body alignment (R1, B1
681 and M_0 are all in the same space).

682 Brain segmentation in healthy subjects:
683 Whole-brain segmentation was computed automatically using the FreeSurfer segmentation
684 algorithm[84]. For subjects with MPRAGE scan, we used that as a reference; for the other subjects
685 the MP2RAGE scan was used. These anatomical images were registered to the R1 space prior to
686 the segmentation process, using a rigid-body alignment. FreeSurfer's estimates of subcortical
687 gray-matter structures were replaced with estimates from FSL's FIRST tool[85].

688 Brain segmentation in meningioma patients:
689 Tumor contouring was performed by the neurosurgeon (T.S.) using BrainLab's Elements software
690 (BrainLab AG, Munich, Germany) over the Gd-enhanced MPRAGE images, and exported as a
691 DICOM file for further analysis. The contours of the tumors were registered to the R1 space
692 using rigid-body segmentation. Cases that required manual adjustment were examined and
693 approved for accuracy by the neurosurgeon (T.S.).

694 Whole-brain segmentation was computed automatically using the FreeSurfer segmentation
695 algorithm[84]. We used the synthetic T1w image generated with mrQ as the reference image, from
696 which we removed the skull and the tumor. We then ran FreeSurfer with the "-noskullstrip" flag.
697 For each patient, we used FreeSurfer's segmentation in the tumor-free hemisphere. Estimates
698 for the entire white matter and gray matter tissues were averaged across the different
699 FreeSurfer parcellations in these regions.

700 r1-r2* relaxivity computation for ROIs in the human brain:
701 We used MATLAB to compute the r1-r2* relaxivity in different brain areas. For each ROI, we
702 extracted the R2* and R1 values from all voxels. R2* values were pooled into 36 bins spaced
703 equally between 0 and 50 s^{-1}. This was done so that the linear fit would not be heavily affected
704 by the density of the voxels in different R2* regimes. We removed any bins in which the number
705 of voxels was smaller than 4% of the total voxel count in the ROI. The median R2* of each bin
706 was computed, along with the R1 median. We used these data points to fit the following linear
707 model across bins using simple linear regression:

$$R1 = aR_2^* + b$$

The slope of this linear model (a) represents the r1-r2* relaxivity. b is constant.

Generating voxel-wise r1-r2* relaxivity visualizations:

In order to generate a voxel-wise visualization of the r1-r2* relaxivity in the brain, we calculated the local linear dependency of R1 on R2* using a moving-window approach. For each voxel within the brain mask, we extracted R1 and R2* values of that voxel and all its neighboring voxels (a box of 125 voxels total). If at least 10 of these voxels were inside the brain mask, we fit the following linear model across these voxels:

$$R1 = aR_2^* + b$$

The slope of this linear model (a) represents the local r1-r2* relaxivity of the voxel. b is constant.

Group-level comparison of qMRI parameters and histological measurements:

We aggregated data published in different papers[5,7,9] that describe ferritin, transferrin and iron concentrations in 11 brain regions. One of the papers[9] described the concentration of L-rich ferritin and H-rich ferritin independently and we combined these estimates for each ROI to get the total ferritin concentration. One of the papers[5] reported the iron level in units of [µmol Fe/ g protein] and we converted these measurements to units of [µg Fe/ g protein]. In order to use this data for our analysis with we matched the brain regions reported in the literature with their corresponding FreeSurfer labels (see table). The table summarizes the aggregated data:

Brain Region	FreeSurfer labels[(f)]	Age group	Transferrin [ng/µg protein][(a)]	Ferritin [ng/µg protein] [(b)]	Iron [mg/g protein] [(c)]
Frontal CTX	1003,1012,1014,1019 ,1020,1027,1028,1032	younger	3.88[7]	45.34[9]	1.21[7]
		older	4.09[7]	89.77[9]	1.59[7]
Caudate	11	younger	3.21[7]	60.92[9]	1.79[7]
		older	4.44[7]	135.12[9]	3.34[7]
Putamen	12	younger	3.49[7]	58.63[9]	2.59[7]
		older	4.47[7]	124.12[9]	4.62[7]
Substantia nigra (midbrain)[(d)]	173	younger	2.45[7]	54.96[9]	2.92[7]
		older	3.42[7]	135.12[9]	5.70[7]
Globus pallidus[(e)]	13	younger	4.82[7]	28.40[9]	7.39[7]
		older	5.10[7]	215.27[9]	4.07[7]
Gray superior temporal gyrus (Temporal CTX)[(d)]	1001,1006,1007,1009, 1015,1016,1030,1033,1034	younger	1.84[5]	25.65[5]	0.45[5]
		older	1.08[5]	24.20[5]	0.69[5]
White superior temporal gyrus (Temporal WM)[(d)]	3001,3006,3007,3009, 3015,3016,3034,3030,3033	younger	3.82[5]	44.87[5]	0.72[5]
		older	2.52[5]	33.50[5]	0.74[5]
Motor CTX	1017,1022,1024,1031	younger	2.91[5]	40.20[5]	1.16[5]

		older	2.93[5]	22.13[5]	0.89[5]
Motor WM	3024,3017,3022,3031	younger	5.75[5]	30.38[5]	1.39[5]
		older	7.34[5]	21.51[5]	1.25[5]
Occipital CTX	1011,1013,1005,1021	younger	1.75[5]	9.34[5]	0.50[5]
		older	1.67[5]	34.27[5]	1.16[5]
Occipital WM	3011,3013,3005,3021	younger	3.53[5]	13.81[5]	0.80[5]
		older	6.07[5]	31.38[5]	0.90[5]

* WM= white matter, CTX=cortex

[a] Transferrin levels were determined by ELISA[7], or by SDS-PAGE and immunoassay with western blotting[5]. In both works transferrin levels were adjusted for total protein as determined with the Bio-Rad Protein Assay (Bio-Rad)[5,7].

[b] Ferritin levels were determined by immunoassays with slot blot technique, and were adjusted for total protein as determined with the Bio-Rad Protein Assay (Bio-Rad) in both works[5,9].

[c] Iron levels were determined by Ferrochem II Serum Iron / TIBC analyzer, and were adjusted for total protein as determined with the Bio-Rad Protein Assay (Bio-Rad)[5,7].

[d] To avoid very small and unreliable ROI segmentations, for the substantia nigra we used the entire midbrain, and for the gray/white superior temporal gyrus we used the entire temporal CTX/WM.

[e] For results when the pallidum is excluded see **Sup. section 5**.

[f] These labels represent left-hemisphere ROIs, but the corresponding right-hemisphere labels were used as well. For each subject, we averaged the MRI measurements of both hemispheres of bilateral brain regions.

726 **Western blot analysis of meningioma tissue:**
727 Fresh frozen meningioma samples (40-50 mg) from 16 patients were homogenized in 200 µL of
728 RIPA buffer (Thermo Fisher Scientific) supplemented with protease inhibitor (Sigma-Aldrich,)
729 using a Bioruptor Pico sonication device (Diagenode) and protein extraction beads (Diagenode,
730 NJ, USA) according to the manufacturer instructions. Protein concentration was determined
731 using the Pierce assay (Thermo Fisher Scientific, MA, USA). Samples containing 20 µg of protein
732 were separated on 4-20% Tris-Glycine SDS-PAGE gel (Bio-Rad, CA, USA) and transferred to PVDF
733 membrane using Trans-Blot Turbo transfer system and transfer packs (Bio-Rad, Hercules, CA,
734 USA). Membranes were probed using Anti-Ferritin Light chain (#AB69090, Abcam, 1:1,000
735 dilution) and Anti-Transferrin (#AB82411, Abcam, 1:10,000 dilution) primary antibodies and
736 appropriate horseradish peroxidase-conjugated secondary antibody (Abcam, Cambridge, UK).
737 Membranes were treated with EZ-ECL (Biological industries, Beit-Ha'emek, Israel) and visualized
738 using ImageQuant LAS 4000 (GE Healthcare, IL, USA). Blot intensities were quantified using the

739 FIJI ImageJ software[86]. The ratio of transferrin/ferritin was based on the ratio in the blot
740 intensities of transferrin and ferritin. Due to the noisy nature of the western-blot analysis, we
741 averaged the estimates over six repetitions. We then used the median transferrin/ferritin ratio
742 across subjects (which was equal to 1) as the threshold between the two groups (low and high
743 transferrin/ferritin ratio).

744 RNA-sequencing of meningioma tissue:

745 RNA-seq libraries: Tumor samples from 17 patients (samples from 16 patients and a replicate for
746 one) were flash frozen and kept in -80c until processing. RNA isolation was done with the
747 following steps: First, frozen tissue was chopped and transferred with a 2ml lysis buffer
748 (Macherey-Nagel, 740955) five times through a needle attached to a 0.9 mm syringe to achieve
749 homogenization. Next, total RNA was extracted with NucleoSpin RNA kit (Macherey-Nagel,
750 740955), following the standard protocol. Finally, mRNA was isolated using the NEBNext Poly(A)
751 mRNA Magnetic Isolation Module (NEB E7490S), using 5ug of total RNA as an input and following
752 the standard protocol. The purified mRNA was used as input for cDNA library preparation, using
753 NEBNext® Ultra™ II Directional RNA Library Prep Kit for Illumina (NEB E7760), and following the
754 standard protocol. Quantification of the libraries was done by Qubit and TapeStation. Paired-end
755 sequencing of the libraries was performed on Nextseq 550.

756 Data processing: The demultiplexing of the samples was done with Illumina's bcl2fastq software.
757 The fastq files were next aligned to the human genome (hg38) using STAR and the transcriptome
758 alignment and gene counts were obtained with HTseq. For quality control RNAseQC software
759 was used. Quality control and data normalization was done in R using the DEseq2 package from
760 Bioconductor (version 3.13). The counts matrix per gene and sample were normalized using the
761 Variance stabilizing transformation. Genes with less than 5 counts were filtered out of the
762 analysis. The filtered and normalized matrix was used in all downstream analysis.

763 Gene set enrichment analysis (GSEA):

764 The final sequencing dataset included the expression of approximately 27,000 genes in 17 tumor
765 samples. We then excluded unannotated genes based on the gene ontology resource
766 (http://geneontology.org/) as well as genes with low (<6) expression levels, yielding 19,500
767 genes.

768 We used GSEA to further validate that the subset of highly correlated genes is not random, but
769 rather represents known biological pathways. For this aim, we calculated the correlations across
770 patients between the expression of each of the genes and one of the qMRI parameters (R1, R2*
771 or r1-r2* relaxivity). For each of the qMRI parameters, genes were ranked based on the *r* values
772 of the correlations, and the ranked list was used in the GSEAPranked toolbox[58,59]. The gene sets
773 databases used for this analysis included go, biocarta, kegg, pid, reactome and wikipathways.

774 The primary result of the GSEA is the enrichment score (ES), which reflects the degree to which a
775 gene set is overrepresented at the top or bottom of a ranked list of genes: A positive ES indicates
776 gene set enrichment at the top of the list, while a negative ES indicates gene set enrichment at
777 the bottom. The normalized ES (NES) accounts for differences in gene set size and in correlations
778 between gene sets and the expression dataset.

779 One tumor sample was excluded from the analysis, as the R1 and R2* values in the tumor were
780 relatively high, which led to the fact that no significantly enriched pathway were found for R1
781 and R2* (though we did detect significantly enriched pathways for the r1-r2* relaxivity).
782 Removing this outlier improved GSEA results for R1 and R2* and we therefore excluded this
783 subject.

784 Following the GSEA analysis, we found a total of 101 significantly enriched pathways for at least
785 one of the R1, R2* and r1-r2* relaxivity. We then clustered those significantly enriched pathways
786 using the "clustergram" function in MATLAB. In order to evaluate which genes are included
787 within the top enrichment pathways for each MRI parameter, we used Leading Edge Analysis (as
788 implemented in the GSEA toolbox).

789 Data availability:
790 The data that support the findings of this study are available on request from the corresponding
791 author (S.F.). The data are not publicly available due to them containing information that could
792 compromise research participant privacy/consent.

793 Code availability:
794 A toolbox for computing the r1-r2* relaxivity, including example data, is available at:
795 [https://github.com/shirfilo/r1_r2s_rel_toolbox].

References:

796 1. Thirupathi, A. & Chang, Y. Z. Brain iron metabolism and CNS diseases. in *Advances in*
797 *Experimental Medicine and Biology* vol. 1173 1–19 (Springer New York LLC, 2019).

798 2. Bulk, M. *et al.* Quantitative comparison of different iron forms in the temporal cortex of
799 Alzheimer patients and control subjects. *Sci. Rep.* **8**, 1–11 (2018).

800 3. Haacke, E. M. *et al.* Imaging iron stores in the brain using magnetic resonance imaging.
801 *Magn. Reson. Imaging* **23**, 1–25 (2005).

802 4. Möller, H. E. *et al.* Iron, Myelin, and the Brain: Neuroimaging Meets Neurobiology. *Trends*

803 *Neurosci.* (2019).

804 5. Connor, J. R., Snyder, B. S., Beard, J. L., Fine, R. E. & Mufson, E. J. Regional distribution of
805 iron and iron-regulatory proteins in the brain in aging and Alzheimer's disease. *J. Neurosci.*
806 *Res.* **31**, 327–335 (1992).

807 6. Connor, J. R., Boeshore, K. L., Benkovic, S. A. & Menzies, S. L. Isoforms of ferritin have a
808 specific cellular distribution in the brain. *J. Neurosci. Res.* **37**, 461–465 (1994).

809 7. Loeffler, D. A. *et al.* Transferrin and Iron in Normal, Alzheimer's Disease, and Parkinson's
810 Disease Brain Regions. *J. Neurochem.* **65**, 710–716.

811 8. Zecca, L., Youdim, M. B. H., Riederer, P., Connor, J. R. & Crichton, R. R. Iron, brain ageing
812 and neurodegenerative disorders. **5**, 863–873 (2004).

813 9. Connor, J. R., Snyder, B. S., Arosio, P., Loeffler, D. A. & LeWitt, P. A Quantitative Analysis of
814 Isoferritins in Select Regions of Aged, Parkinsonian, and Alzheimer's Diseased Brains. *J.*
815 *Neurochem.* **65**, 717–724 (1995).

816 10. Ward, R. J., Zucca, F. A., Duyn, J. H., Crichton, R. R. & Zecca, L. *The role of iron in brain*
817 *ageing and neurodegenerative disorders*. *The Lancet Neurology* vol. 13 1045–1060 (2014).

818 11. Zarow, C., Lyness, S. A., Mortimer, J. A. & Chui, H. C. Neuronal loss is greater in the locus
819 coeruleus than nucleus basalis and substantia nigra in Alzheimer and Parkinson diseases.
820 *Arch. Neurol.* **60**, 337–341 (2003).

821 12. Sulzer, D. *et al.* Neuromelanin detection by magnetic resonance imaging (MRI) and its
822 promise as a biomarker for Parkinson's disease. *NPJ Park. Dis.* **4**, 11 (2018).

823 13. Legendre, C. & Garcion, E. Iron metabolism: A double-edged sword in the resistance of
824 glioblastoma to therapies. *Trends in Endocrinology and Metabolism* vol. 26 322–331
825 (2015).

826 14. Chen, Y., Fan, Z., Yang, Y. & Gu, C. Iron metabolism and its contribution to cancer (Review).
827 *International Journal of Oncology* vol. 54 1143–1154 (2019).

828 15. Pfeifhofer-Obermair, C., Tymoszuk, P., Petzer, V., Weiss, G. & Nairz, M. Iron in the tumor
829 microenvironment-connecting the dots. *Frontiers in Oncology* vol. 8 549 (2018).

830 16. Whittle, I. R., Smith, C., Navoo, P. & Collie, D. Meningiomas. in *Lancet* vol. 363 1535–1543
831 (2004).

832 17. Brem, F. *et al.* Magnetic iron compounds in the human brain: A comparison of tumour and
833 hippocampal tissue. *J. R. Soc. Interface* **3**, 833–841 (2006).

834 18. Hänninen, M. M. *et al.* Expression of iron-related genes in human brain and brain tumors.
835 *BMC Neurosci.* **10**, 36 (2009).

836 19. Gelman, N., Ewing, J. R., Gorell, J. M., Spickler, E. M. & Solomon, E. G. Interregional
837 variation of longitudinal relaxation rates in human brain at 3.0 T: Relation to estimated
838 iron and water contents. *Magn. Reson. Med.* (2001).

839 20. Callaghan, M. F., Helms, G., Lutti, A., Mohammadi, S. & Weiskopf, N. A general linear
840 relaxometry model of R_1 using imaging data. *Magn. Reson. Med.* **73**, 1309–1314 (2015).

841 21. Langkammer, C. *et al.* Quantitative MR imaging of brain iron: A postmortem validation
842 study. *Radiology* **257**, 455–462 (2010).

843 22. Vymazal, J. *et al.* The relation between brain iron and NMR relaxation times: An in vitro
844 study. *Magn. Reson. Med.* **35**, 56–61 (1996).

845 23. Cercignani, M., Dowell, N. G. & Tofts, P. S. *Quantitative MRI of the Brain : Principles of*
846 *Physical Measurement*. (CRC Press, 2018).

847 24. Basser, P. J. & Pierpaoli, C. Microstructural and Physiological Features of Tissues
848 Elucidated by Quantitative-Diffusion-Tensor MRI. *J. Magn. Reson. Ser. B* **111**, 209–219
849 (1996).

850 25. Weiskopf, N., Mohammadi, S., Lutti, A. & Callaghan, M. F. Advances in MRI-based
851 computational neuroanatomy. *Curr. Opin. Neurol.* **28**, 313–322 (2015).

852 26. Weiskopf, N., Edwards, L. J., Helms, G., Mohammadi, S. & Kirilina, E. Quantitative magnetic

853 resonance imaging of brain anatomy and in vivo histology. *Nat. Rev. Phys.* 1–19 (2021).

854 27. Ghadery, C. *et al.* R2* mapping for brain iron: Associations with cognition in normal aging.
855 *Neurobiol. Aging* **36**, 925–932 (2015).

856 28. Vymazal, J. *et al.* T1 and T2 in the brain of healthy subjects, patients with Parkinson
857 disease, and patients with multiple system atrophy: Relation to iron content. *Radiology*
858 **211**, 489–495 (1999).

859 29. Lorio, S. *et al.* Disentangling in vivo the effects of iron content and atrophy on the ageing
860 human brain. *Neuroimage* **103**, 280–289 (2014).

861 30. Edwards, L. J., Kirilina, E., Mohammadi, S. & Weiskopf, N. Microstructural imaging of
862 human neocortex in vivo. *NeuroImage* vol. 182 184–206 (2018).

863 31. Ogg, R. J. & Steen, R. G. Age-related changes in Brain T1 are correlated with iron
864 concentration. *Magn. Reson. Med.* **40**, 749–753 (1998).

865 32. Wood, J. C., Fassler, J. D. & Meade, T. Mimicking liver iron overload using liposomal ferritin
866 preparations. *Magn. Reson. Med.* **51**, 607–611 (2004).

867 33. Gossuin, Y., Muller, R. N. & Gillis, P. Relaxation induced by ferritin: a better understanding
868 for an improved MRI iron quantification. *NMR Biomed.* **17**, 427–432 (2004).

869 34. Zhang, N. *et al.* A model for the analysis of competitive relaxation effects of manganese
870 and iron in vivo. *NMR Biomed.* (2009).

871 35. Bennett, K. M., Shapiro, E. M., Sotak, C. H. & Koretsky, A. P. Controlled aggregation of
872 ferritin to modulate MRI relaxivity. *Biophys. J.* **95**, 342–351 (2008).

873 36. Rohrer, M., Bauer, H., Mintorovitch, J., Requardt, M. & Weinmann, H.-J. Comparison of
874 Magnetic Properties of MRI Contrast Media Solutions at Different Magnetic Field
875 Strengths. *Invest. Radiol.* **40**, (2005).

876 37. Kiselev, V. G. & Novikov, D. S. Transverse NMR relaxation in biological tissues. *NeuroImage*
877 vol. 182 149–168 (2018).

878 38. Brammerloh, M. *et al.* Measuring the iron content of dopaminergic neurons in substantia
879 nigra with MRI relaxometry. *Neuroimage* **239**, 118255 (2021).

880 39. Birkl, C. *et al.* The influence of iron oxidation state on quantitative MRI parameters in post
881 mortem human brain. *Neuroimage* **220**, (2020).

882 40. Callaghan, M. F. *et al.* Widespread age-related differences in the human brain
883 microstructure revealed by quantitative magnetic resonance imaging. *Neurobiol. Aging*
884 **35**, 1862–1872 (2014).

885 41. Heath, F., Hurley, S. A., Johansen-Berg, H. & Sampaio-Baptista, C. Advances in noninvasive
886 myelin imaging. *Dev. Neurobiol.* **78**, 136–151 (2018).

887 42. Lutti, A., Dick, F., Sereno, M. I. & Weiskopf, N. Using high-resolution quantitative mapping
888 of R1 as an index of cortical myelination. *Neuroimage* **93**, 176–188 (2014).

889 43. Stüber, C. *et al.* Myelin and iron concentration in the human brain: A quantitative study of
890 MRI contrast. *Neuroimage* **93**, 95–106 (2014).

891 44. Callaghan, M. F., Helms, G., Lutti, A., Mohammadi, S. & Weiskopf, N. A general linear
892 relaxometry model of R1 using imaging data. *Magn. Reson. Med.* **73**, 1309–14 (2015).

893 45. Kirilina, E. *et al.* Superficial white matter imaging: Contrast mechanisms and whole-brain
894 in vivo mapping. *Sci. Adv.* **6**, aaz9281 (2020).

895 46. Mezer, A. *et al.* Quantifying the local tissue volume and composition in individual brains
896 with magnetic resonance imaging. *Nat. Med.* **19**, 1667–72 (2013).

897 47. Helms, G., Dathe, H., Kallenberg, K. & Dechent, P. High-resolution maps of magnetization
898 transfer with inherent correction for RF inhomogeneity and T_1 relaxation obtained from
899 3D FLASH MRI. *Magn. Reson. Med.* **60**, 1396–1407 (2008).

900 48. Mohammadi, S. & Callaghan, M. F. Towards in vivo g-ratio mapping using MRI: Unifying
901 myelin and diffusion imaging. *J. Neurosci. Methods* **348**, 108990 (2021).

902 49. Berman, S., West, K. L., Does, M. D., Yeatman, J. D. & Mezer, A. A. Evaluating g-ratio

903 weighted changes in the corpus callosum as a function of age and sex. *Neuroimage* **182**,
904 304–313 (2018).

905 50. Mancini, M. *et al.* An interactive meta-analysis of MRI biomarkers of Myelin. *Elife* **9**, 1–23
906 (2020).

907 51. Piredda, G. F., Hilbert, T., Thiran, J. & Kober, T. Probing myelin content of the human brain
908 with MRI: A review. *Magn. Reson. Med.* **85**, 627–652 (2021).

909 52. Lévy, S. *et al.* Test-retest reliability of myelin imaging in the human spinal cord:
910 Measurement errors versus region- and aging-induced variations. *PLoS One* **13**, (2018).

911 53. Peters, J. M. *et al.* White matter mean diffusivity correlates with myelination in tuberous
912 sclerosis complex. *Ann. Clin. Transl. Neurol.* **6**, 1178–1190 (2019).

913 54. Essig, M. *et al.* Contrast-Enhanced Magnetic Resonance Imaging of Central Nervous
914 System Tumors. *Top. Magn. Reson. Imaging* **17**, 89–106 (2006).

915 55. Gulani, V., Calamante, F., Shellock, F. G., Kanal, E. & Reeder, S. B. Gadolinium deposition in
916 the brain: summary of evidence and recommendations. *The Lancet Neurology* vol. 16
917 564–570 (2017).

918 56. McDonald, R. J. *et al.* Gadolinium deposition in human brain tissues after contrast-
919 enhanced MR imaging in adult patients without intracranial abnormalities. *Radiology* **285**,
920 546–554 (2017).

921 57. Falk Delgado, A. A. *et al.* Diagnostic value of alternative techniques to gadolinium-based
922 contrast agents in MR neuroimaging—a comprehensive overview. *Insights into Imaging*
923 vol. 10 1–15 (2019).

924 58. Subramanian, A. *et al.* Gene set enrichment analysis: A knowledge-based approach for
925 interpreting genome-wide expression profiles. *Proc. Natl. Acad. Sci. U. S. A.* **102**, 15545–
926 15550 (2005).

927 59. Mootha, V. K. *et al.* PGC-1α-responsive genes involved in oxidative phosphorylation are
928 coordinately downregulated in human diabetes. *Nat. Genet.* **34**, 267–273 (2003).

929 60. Fang, L. *et al.* The immune cell infiltrate populating meningiomas is composed of mature,
930 antigen-experienced T and B cells. *Neuro. Oncol.* **15**, 1479–1490 (2013).

931 61. Comtesse, N. *et al.* Complex humoral immune response against a benign tumor: Frequent
932 antibody response against specific antigens as diagnostic targets. *Proc. Natl. Acad. Sci. U.*
933 *S. A.* **102**, 9601–9606 (2005).

934 62. Chiabrando, D., Vinchi, F., Fiorito, V., Mercurio, S. & Tolosano, E. Heme in
935 pathophysiology: A matter of scavenging, metabolism and trafficking across cell
936 membranes. *Front. Pharmacol.* **5**, 1–24 (2014).

937 63. Rosager, A. M. *et al.* Transferrin receptor-1 and ferritin heavy and light chains in astrocytic
938 brain tumors: Expression and prognostic value. *PLoS One* **12**, e0182954 (2017).

939 64. Sanchez, M. *et al.* Iron regulation and the cell cycle: identification of an iron-responsive
940 element in the 3'-untranslated region of human cell division cycle 14A mRNA by a refined
941 microarray-based screening strategy. *J Biol Chem.* **281**, 22865–74 (2006).

942 65. De Leõn-Rodríguez, L. M., Martins, A. F., Pinho, M. C., Rofsky, N. M. & Sherry, A. D. Basic
943 MR relaxation mechanisms and contrast agent design. *J. Magn. Reson. Imaging* **42**, 545–
944 565 (2015).

945 66. Zecca, L. *et al.* The role of iron and copper molecules in the neuronal vulnerability of locus
946 coeruleus and substantia nigra during aging. *Proc. Natl. Acad. Sci.* **101**, 9843–9848 (2004).

947 67. Thulborn, K. R., Waterton, J. C., Matthews, P. M. & Radda, G. K. Oxygenation dependence
948 of the transverse relaxation time of water protons in whole blood at high field. *Biochim.*
949 *Biophys. Acta* **714**, 265–270 (1982).

950 68. Ogawa, S., Lee, T. M., Kay, A. R. & Tank, D. W. Brain magnetic resonance imaging with
951 contrast dependent on blood oxygenation. *Proc. Natl. Acad. Sci. U. S. A.* **87**, 9868 (1990).

952 69. Viessmann, O., Scheffler, K., Bianciardi, M., Wald, L. L. & Polimeni, J. R. Dependence of
953 resting-state fMRI fluctuation amplitudes on cerebral cortical orientation relative to the
954 direction of B0 and anatomical axes. *Neuroimage* **196**, 337–350 (2019).

955 70. Wagner, K. R., Sharp, F. R., Ardizzone, T. D., Lu, A. & Clark, J. F. Heme and iron metabolism:
956 Role in cerebral hemorrhage. *Journal of Cerebral Blood Flow and Metabolism* vol. 23 629–
957 652 (2003).

958 71. Todorich, B., Pasquini, J. M., Garcia, C. I., Paez, P. M. & Connor, J. R. Oligodendrocytes and
959 myelination: The role of iron. *GLIA* vol. 57 467–478 (2009).

960 72. Reinert, A., Morawski, M., Seeger, J., Arendt, T. & Reinert, T. Iron concentrations in
961 neurons and glial cells with estimates on ferritin concentrations. *BMC Neurosci.* **20**, 25
962 (2019).

963 73. Trujillo, P. *et al.* Contrast mechanisms associated with neuromelanin-MRI. *Magn. Reson.*
964 *Med.* **78**, 1790–1800 (2017).

965 74. Taege, Y. *et al.* Assessment of mesoscopic properties of deep gray matter iron through a
966 model-based simultaneous analysis of magnetic susceptibility and R2* - A pilot study in
967 patients with multiple sclerosis and normal controls. *Neuroimage* **186**, 308–320 (2019).

968 75. Zhou, Z. & Lu, Z. R. Gadolinium-based contrast agents for magnetic resonance cancer
969 imaging. *Wiley Interdisciplinary Reviews: Nanomedicine and Nanobiotechnology* vol. 5 1–
970 18 (2013).

971 76. Filo, S. *et al.* Disentangling molecular alterations from water-content changes in the aging
972 human brain using quantitative MRI. *Nat. Commun.* **10**, (2019).

973 77. Shtangel, O. & Mezer, A. A. A phantom system for assessing the effects of membrane
974 lipids on water proton relaxation. *NMR Biomed.* **33**, (2020).

975 78. Mezer, A., Rokem, A., Berman, S., Hastie, T. & Wandell, B. A. Evaluating quantitative
976 proton-density-mapping methods. *Hum. Brain Mapp.* **37**, 3623–3635 (2016).

977 79. Weiskopf, N. *et al.* Quantitative multi-parameter mapping of R1, PD*, MT, and R2* at 3T:
978 A multi-center validation. *Front. Neurosci.* (2013).

979 80. Smith, S. M. *et al.* Advances in functional and structural MR image analysis and
980 implementation as FSL. *Neuroimage* (2004).

981 81. Behrens, T. E. J. *et al.* Characterization and propagation of uncertainty in diffusion-
982 weighted MR imaging. *Magn. Reson. Med.* (2003).

983 82. Andersson, J. L. R., Skare, S. & Ashburner, J. How to correct susceptibility distortions in
984 spin-echo echo-planar images: Application to diffusion tensor imaging. *Neuroimage* **20**,
985 870–88 (2003).

986 83. Andersson, J. L. R. & Sotiropoulos, S. N. An integrated approach to correction for off-
987 resonance effects and subject movement in diffusion MR imaging. *Neuroimage* **125**,
988 1063–1078 (2016).

989 84. Fischl, B. FreeSurfer. *Neuroimage* **62**, 774–781 (2012).

990 85. Patenaude, B., Smith, S. M., Kennedy, D. N. & Jenkinson, M. A Bayesian model of shape
991 and appearance for subcortical brain segmentation. *Neuroimage* **56**, 907–22 (2011).

992 86. Schindelin, J. *et al.* Fiji: An open-source platform for biological-image analysis. *Nature*
993 *Methods* vol. 9 676–682 (2012).

994 87. Donahue, K. M., Weisskoff, R. M. & Burstein, D. Water diffusion and exchange as they
995 influence contrast enhancement. *J. Magn. Reson. Imaging* **7**, 102–110 (1997).

996 88. Rooney, W. D. *et al.* Magnetic field and tissue dependencies of human brain
997 longitudinal1H2O relaxation in vivo. *Magn. Reson. Med.* **57**, 308–318 (2007).

998 89. Dlháň, Ľ., Kopáni, M. & Boča, R. Magnetic properties of iron oxides present in the human
999 brain. *Polyhedron* **157**, 505–510 (2019).

1000 90. Erikson, K. M., Syversen, T., Steinnes, E. & Aschner, M. Globus pallidus: A target brain
1001 region for divalent metal accumulation associated with dietary iron deficiency. *J. Nutr.*
1002 *Biochem.* **15**, 335–341 (2004).

Supplementary Materials for

"Non-invasive assessment of normal and impaired iron homeostasis in living human brains"

Contents

Supplementary Figure 1 3
Supplementary Section 1: The dependency of R1 and R2* on the iron concentration. 4
Supplementary Figure 2 5
Supplementary Figure 3 6
Supplementary Figure 4 7
Supplementary Section 2: The dependency of the iron relaxivity on the liposomal fraction. 8
Supplementary Figure 5 10
Supplementary Figure 6 11
Supplementary Figure 7 12
Supplementary Figure 8 13
Supplementary Figure 9 13
Supplementary Section 3: Voxel-wise r1-r2* relaxivity visualization. 14
Supplementary Figure 10 15
Supplementary Figure 11 16
Supplementary Figure 12 17
Supplementary Figure 13 18
Supplementary Figure 14 19
Supplementary Figure 15 19
Supplementary Figure 16 20
Supplementary Table 1 21
Supplementary Figure 17 22
Supplementary Figure 18 23
Supplementary Section 4: Exploring the biophysical sources of the r1-r2* relaxivity. 24
Supplementary Section 4.1: The theoretical basis for the r1-r2* relaxivity of brain tissue. 24
Supplementary Section 4.2: The r1-r2* relaxivity of ferritin and transferrin mixtures *in vitro*. 24
Supplementary Section 4.3: Numerical simulations of the r1-r2* relaxivity. 28
Supplementary Section 5: The r1-r2* relaxivity in the pallidum. 37
Supplementary Figure 31 38
Supplementary methods 39

Supplementary Figure 1

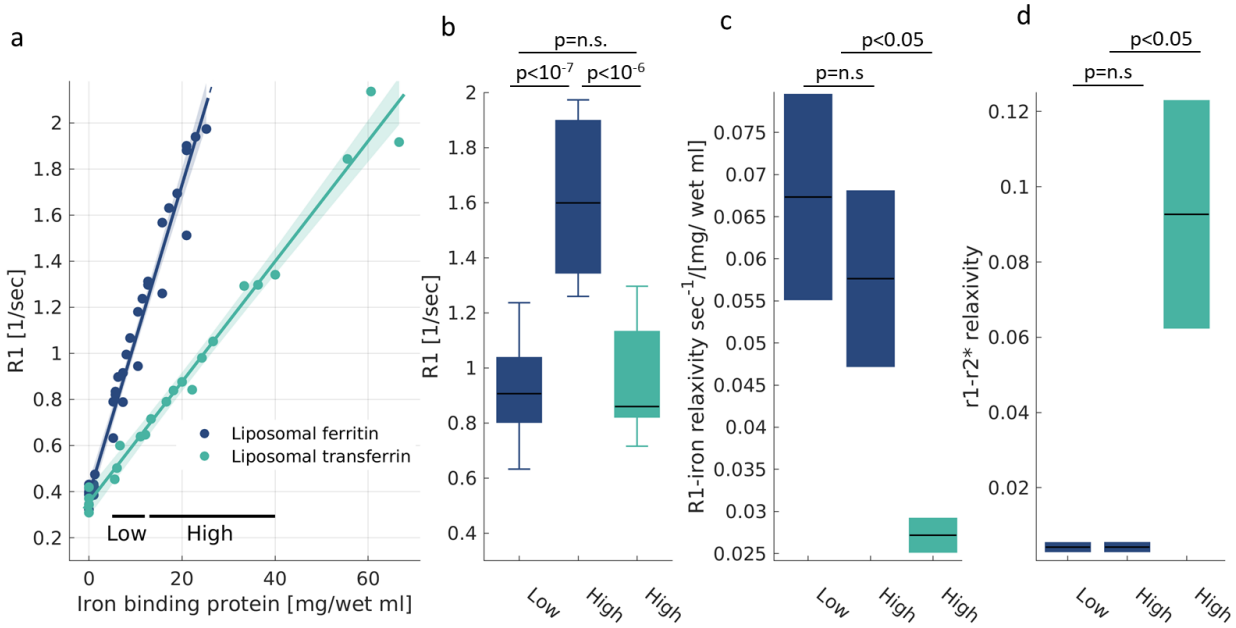

Sup. Figure 1: The effect of iron concentration on different MR estimations. (a) *The dependency of R1 on the iron-binding protein concentration for liposomal ferritin and liposomal transferrin. Data points represent liposomal samples with varying iron-binding protein concentrations relative to the water fraction ([mg/wet ml]). The linear relationships between relaxation rates and iron-binding protein concentrations are marked by lines. The slopes of these lines are the iron relaxivities. Shaded areas represent the 95% confidence bounds.* ***(b)*** *The ambiguity in R1; R1 changes as a function of both iron environment and iron concentration. This is shown by calculating the median R1 value over samples with high and low iron-binding protein concentrations (marked in (a); concentration ranges were chosen so that the number of data points in each range is similar). We find that R1 is greater for a higher ferritin concentration than for a lower ferritin concentration, but also find that R1 is greater for ferritin than for transferrin. For each box, the central line marks the median, the box extends vertically between the 25th and 75th percentiles, and the whiskers extend to the most extreme data points.* ***(c-d)*** *The ambiguity in R1 is resolved by the R1-iron relaxivity (c) and the r1-r2* (d), which are consistent when computed over higher or lower ferritin concentrations, and are consistently different from the iron relaxivity of transferrin regardless the concentration. For each box, the central lines marks the iron relaxivity, and the box shows the 95% confidence bounds of the linear fit. p-values are for the ANCOVA test corrected for multiple comparisons.*

Supplementary Section 1: The dependency of R1 and R2* on the iron concentration.

In ***Figure 1*** we computed the iron relaxivity as the dependency of R1 and R2* on the concentration of iron-binding proteins. We showed that different iron environments have different relaxivities. However, different proteins bind different amounts of iron. For example, ferritin binds three orders of magnitude more iron ions than does transferrin[3]. Therefore, we wanted to exclude the possibility that the different iron ion concentrations drive the different relaxivities of ferritin and transferrin.

We verified that the relaxivity changes according to the molecular type of iron, even when accounting for discrepancies in iron loading. We estimated the iron ion concentrations for ferritin and transferrin (see Methods section "Estimation of total iron content in phantoms") and tested whether those values can explain their different iron relaxivities. Importantly, after computing the iron relaxivity as the dependency of relaxation rates on the iron ion concentrations (rather than the concentration of iron-binding proteins), we still find that different iron environments have distinct relaxivities (**Sup. Figure 2**, $p(ANCOVA)<10^{-39}$).

To further stress the sensitivity of the r1-r2* relaxivity to the iron environment, we compared the relaxivity of liposomal ferrous iron (Fe^{2+}) and iron bound to liposomal transferrin (**Sup. Figure 3**). Unlike ferritin and transferrin, these two iron compounds have relatively similar iron ion concentrations. Yet we find that they produce different iron relaxivities ($p(ANCOVA)<10^{-4}$). The r1-r2* relaxivities of these two iron environments are different as well ($p(ANCOVA)<0.05$). Therefore, the iron relaxivity and the r1-r2* relaxivity are changing as a function of the molecular iron environment, even when accounting for the differences in iron binding.

Supplementary Figure 2

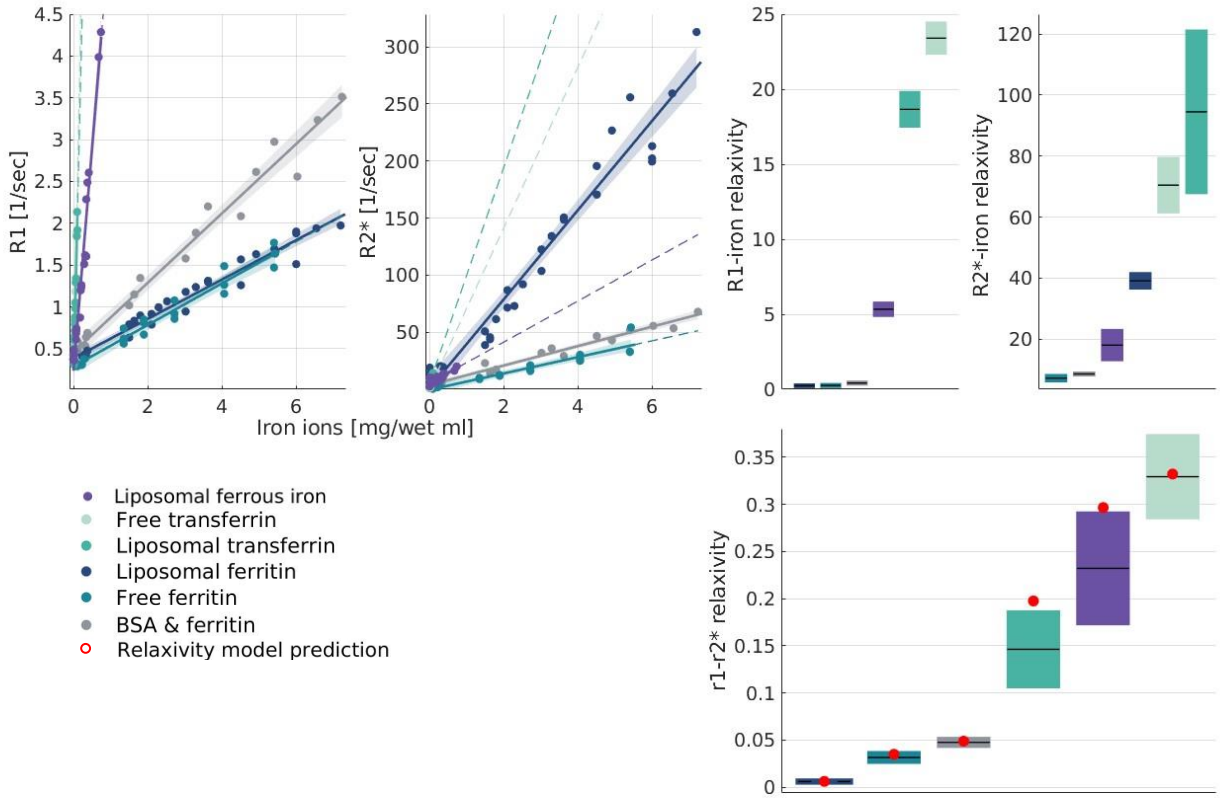

Sup. Figure 2: The iron relaxivity and the r1-r2* relaxivity are sensitive to the molecular type of iron regardless of the differences in iron-binding. (a-b) *The dependency of R1 and R2* on the estimated iron concentration (see method section "Estimation of total iron content in phantoms") for six different iron compounds: free ferritin, liposomal-ferritin, Bovine Serum Albumin (BSA)-ferritin mixture, free transferrin, liposomal transferrin and liposomal ferrous iron. Data points represent samples with varied estimated iron ion concentrations relative to the water fraction ([mg/wet ml]). The linear relationships between relaxation rates and iron concentration are marked by lines. The slopes of these lines are the iron relaxivities. Dashed lines represent extrapolations the linear fits, and shaded areas represent the 95% confidence bounds.* ***(c)*** *The iron relaxivities of R1 and R2* are different for different iron environments (p(ANCOVA)<10^{39}). Iron relaxivity is calculated here based on the estimated iron concentration (and not iron-binding proteins concentrations, as in* Figure 1*). To do so, we use the slope of the linear relationships shown in (a,b), expressed in [sec-1/(mg/wet ml)]. For each box the central lines marks the iron relaxivity, and the box shows the 95% confidence bounds of the linear fit.* ***(d)*** *The theoretical model successfully predicts the r1-r2* relaxivity even when it is based on the estimated iron ions concentration (and not iron compound concentrations, as in* Figure 1*). The model's prediction is based on the ratio between the iron relaxivities of R1 and R2* as shown in (c). For each box the central line marks the r1-r2* relaxivity, and the box shows the 95% confidence bounds of the linear fit. Red dots represent the prediction of the theoretical model.*

Supplementary Figure 3

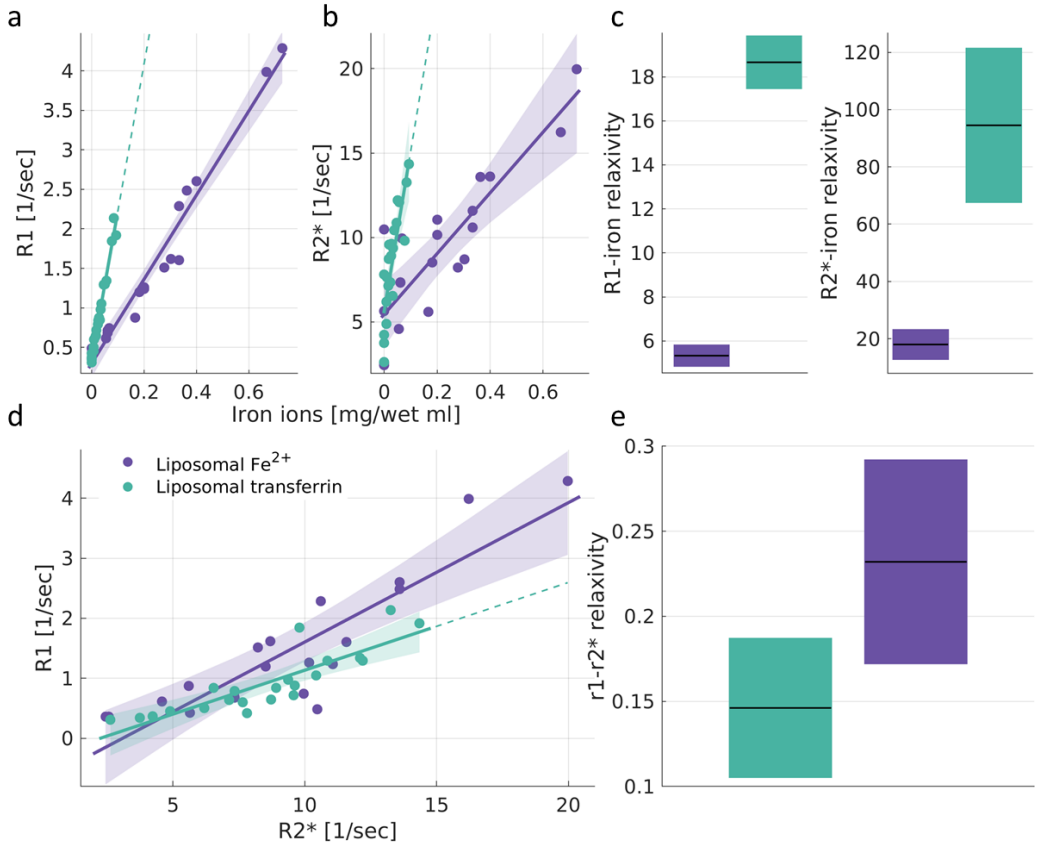

Sup. Figure 3: The iron relaxivity and the r1-r2* relaxivity are sensitive to the molecular iron environment even when the iron concentration is similar. (a-b) *The dependency of R1 and R2* on the estimated iron concentration for two different iron environments: liposomal transferrin (purple) and liposomal Fe^{2+} (green). Data points represent liposomal samples with varying iron ion concentrations relative to the water fraction ([mg/wet ml]). The linear relationships between relaxation rates and iron ion concentration are marked by lines. The slopes of these lines are the iron relaxivities. Dashed lines represent extrapolations of the linear fits. Shaded areas represent the 95% confidence bounds.* ***(c)*** *The iron relaxivity of R1 and R2* is different for different iron environments (p(ANCOVA)<10^{-4}). Iron relaxivity is calculated by taking the slope of the linear relationships shown in (a,b), and is measured in [sec-1/(mg/wet ml)]. For each box, the central line marks the iron relaxivity, and the box shows the 95% confidence bounds of the linear fit.* ***(d)*** *The dependency of R1 on R2* for different iron environments. Data points represent samples with varying concentrations. The linear relationships between R1 and R2* are marked by lines. The slopes of these lines are the r1-r2* relaxivities. Dashed lines represent extrapolations of the linear fits. Shaded areas represent the 95% confidence bounds.* ***(e)*** *The r1-r2* relaxivity is different for different iron environments (p(ANCOVA)<0.05). For each box, the central line marks the r1-r2* relaxivity, and the box shows the 95% confidence bounds of the linear fit.*

Supplementary Figure 4

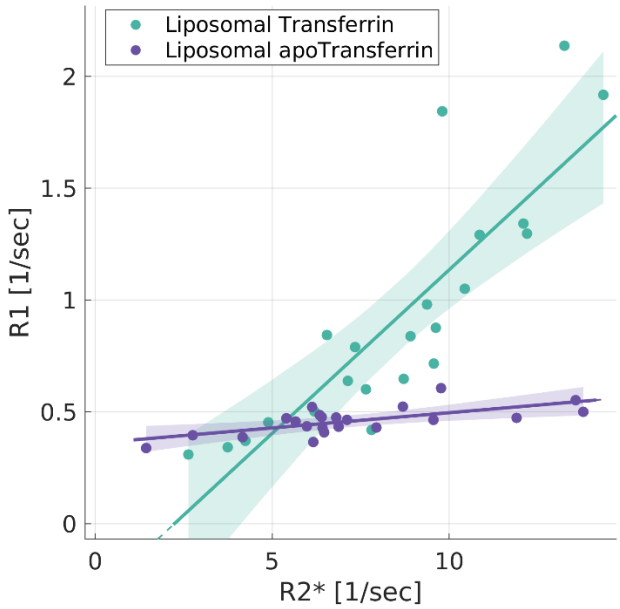

Sup. Figure 4: Validating the sensitivity of the the r1-r2* relaxivity to the paramagnetic properties of transferrin. *Data points represent liposomal samples with varying concentrations of transferrin (green) and apo-transferrin (transferrin which is not bound to iron, in purple). The linear relationships between R1 and R2* are marked by lines. The slopes of these lines are the r1-r2* relaxivities. Shaded areas represent the 95% confidence bounds. Apo-transferrin with no iron has lower r1-r2* relaxivity compared to iron-bound transferrin (p(ANCOVA)<10^{-8}). Therefore, the r1-r2* relaxivity is sensitive to the paramagnetic properties of iron-binding proteins and not to the proteins themselves.*

Supplementary Section 2: The dependency of the iron relaxivity on the liposomal fraction.

R1 and R2* measured in the brain are known to be sensitive to myelin content[4,19,25,29,40–42]. Myelin is composed mainly of lipids, though it also includes proteins. We tested the effect of the myelin fraction on iron relaxivity by varying the liposomal and protein (BSA) fractions in our phantoms.

In histological studies of brain iron, the iron concentrations often are reported relative to the wet weight, as this is considered more accurate[4]. To match our *in vitro* analysis to brain histology as much as possible, we calculated the iron-binding proteins' concentrations relative to the water fraction ([mg/wet ml]). This was done by computing the ratio between the iron concentration and the water fraction (which is complementary to the liposomal or protein fractions). The iron relaxivities shown in **Figure 1** were therefore calculated as the linear dependencies of relaxation rates on the iron-binding protein concentration relative to the water fraction. **Sup. Figure 5** presents the effect of the variable liposomal (or BSA) fractions on the iron relaxivity and on the r1-r2* relaxivity. When iron-binding protein concentrations were not calibrated to the water fraction (units of [mg/ml]), some variability in R1 and R2* values for different liposomal (or BSA) fractions was observed (**Sup. Figure 5a,c**). However, the iron relaxivities of different iron environments were still distinct, despite the liposomal (or BSA) fractions' variability. Calibrating the iron-binding protein concentrations to the water fraction (units of [mg/wet ml]) further eliminated the effect of the variable liposomal (or BSA) fractions on the iron relaxivities (**Sup. Figure 5b,d**). This is evident by the alignment of the data points with different liposomal (or BSA) fractions along the iron relaxivity's linear fits. Therefore, while the non-water fraction has an effect on the relaxation rates, it does not disrupt the sensitivity of the iron relaxivities to the molecular type of iron.

We further estimated the effect of the liposomal (or BSA) fractions on the r1-r2* relaxivity. In **Sup. Figure 5e** we show the same r1-r2* relaxivities presented in **Figure 1,** but now the liposomal (or BSA) fractions are indicated by different symbols. Similarly to the iron relaxivities, the r1-r2* relaxivities of different iron environments were distinct, even though they were calculated across varying liposomal (or BSA) fractions. Moreover, we estimated the r1-r2* relaxivity separately for

each liposomal (or BSA) fraction (**Sup. Figure 5f**). We find that the r1-r2* relaxivity differences between iron compounds are greater than the differences within each iron compound for the variable liposomal (or BSA) fractions.

The dependency of R1 on the macromolecular tissue volume (MTV) was associated with lipid composition in our previous work[76]. We tested this finding in the presence of iron by calculating the R1-MTV dependencies for different types of lipids mixed with iron (**Sup. Figure 6a-b**). Notably, in the current study we sampled only three liposomal fractions, and therefore the variation in the iron concentration between the samples was much richer than the variation in lipid concentration. Still, we were able to replicate our finding regarding the sensitivity of the R1-MTV dependency to lipid type. We find that the R1-MTV dependencies are different for two types of lipid mixtures (phosphatidylcholine (PC) and phosphatidylcholine-sphingomyelin (PC-SM)) mixed with ferrous (Fe^{2+}) iron (**Sup. Figure 6a**). In the presence of ferritin, the difference between the R1-MTV dependencies of the two lipids is smaller (**Sup. Figure 6b**).

Unlike the R1-MTV dependency, the r1-r2* relaxivity is insensitive to the lipid composition (**Sup. Figure 6c**): different lipids mixed with ferritin have a similar r1-r2* relaxivity (p(ANCOVA)=0.11). The variability in the r1-r2* relaxivity was much bigger when comparing these different liposomal ferritin samples to liposomal transferrin (p(ANOCVA)<10^{-7}). Compared to the R1-MTV dependencies, we find that the r1-r2* relaxivity provides a better distinction between iron compounds. **Sup. Figure 7** presents the r1-r2* relaxivities and the R1-MTV dependencies for different iron compounds. ANCOVA tests for the R1-MTV dependencies reveal that the only significant distinction is between the BSA-ferritin mixture and all the liposomal iron compounds (p(ANCOVA)<10^{-5}). The rest of the iron environments are indistinguishable in terms of their R1-MTV dependencies. On the contrary, all iron environments were distinguishable in terms of their r1-r2* relaxivity (p(ANCOA)<10^{-32}).

Supplementary Figure 5

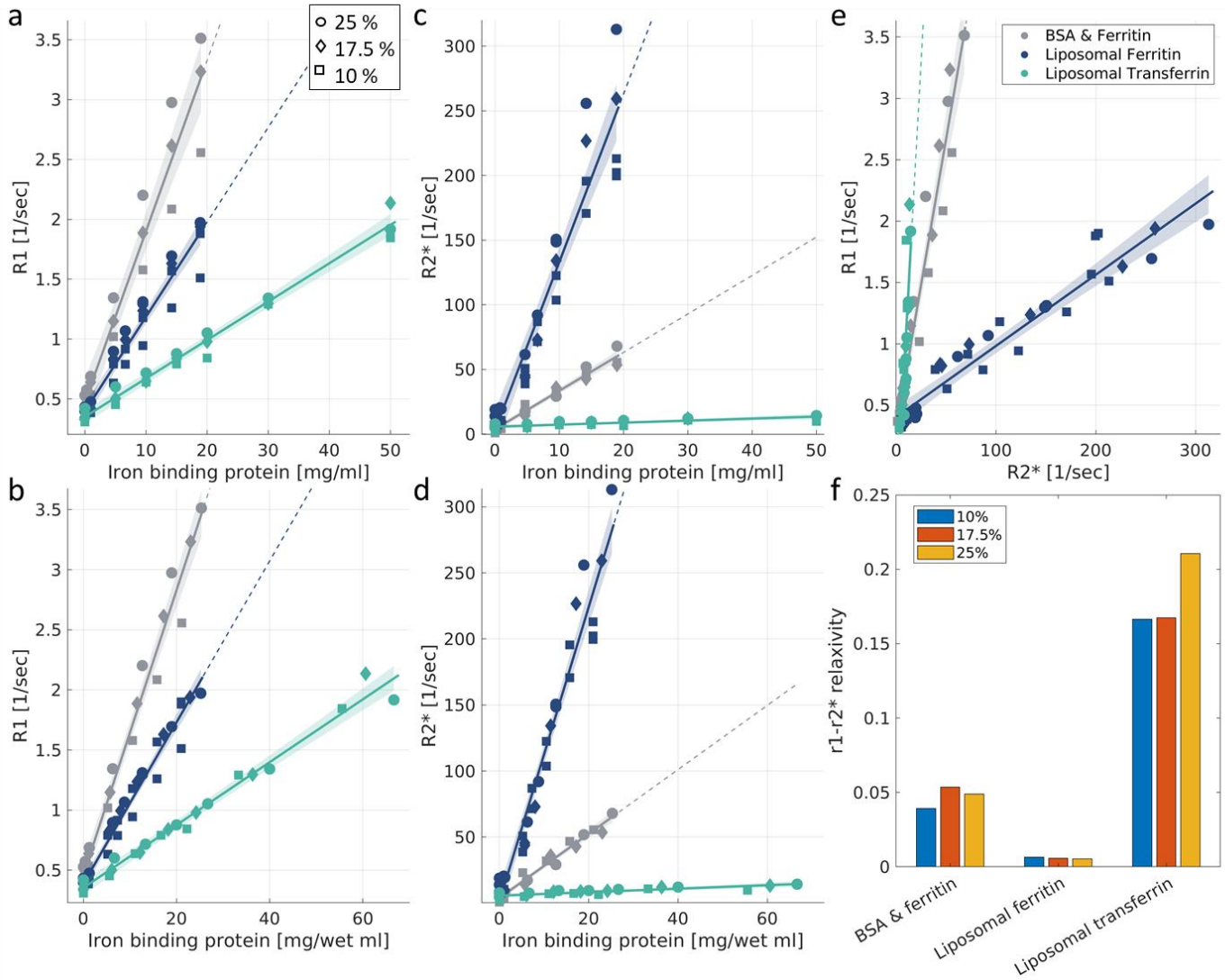

Sup. Figure 5: Relaxivities are stable across liposomal or BSA fractions. (a) *The dependency of R1 on the iron-binding protein concentration for different liposomal (or BSA) fractions (different symbols) and different iron environments (different colors). The x-axis represents the absolute concentration of iron-binding proteins (not relative to the water concentration, as in b). The linear relationships between relaxation rates and iron-binding protein concentration are marked by lines. The slopes of these lines are defined as the iron relaxivities. R1 values are affected by the variable liposomal (or BSA) fractions, but the iron relaxivities of different iron environments are still distinct, regardless of this manipulation. Dashed lines represent extrapolations of the linear fits. Shaded areas represent the 95% confidence bounds.* ***(b)*** *The dependency of R1 on the iron-binding protein concentration for different liposomal (or BSA) fractions (different symbols) and different iron environments (different colors). Here the x-axis represents the concentration of iron-binding proteins relative to the water fraction (which varies with the liposomal or BSA fraction). This estimation, in units of [mg/wet ml], further eliminates the effect of the liposomal (or BSA) fraction on the iron relaxivities. This is evident by the alignment of the data points with different liposomal (or BSA) fractions (different symbols) along the iron relaxivity linear fit.* ***(c-d)*** *A similar analysis for the R2*-iron relaxivity. The effect of the different liposomal (or BSA) fractions on the*

R2-iron relaxivity is eliminated by the calculation of the iron-binding proteins concentration relative to the water fraction ([mg/wet ml]).* ***(e)*** *The dependency of R1 on R2* for different liposomal (or BSA) fractions (different symbols) and different iron environments (different colors). The r1-r2* relaxivities of different iron environments are distinct even when calculated across liposomal (or BSA) fractions.* ***(f)*** *The r1-r2* relaxivity (y-axis) for different compounds of iron (liposomal ferritin, liposomal transferrin and BSA-ferritin mixture) in three different liposomal (or BSA) fractions (colors). The differences in the r1-r2* relaxivity between iron environments are greater than the differences within each iron environment for the variable liposomal (or BSA) fractions.*

Supplementary Figure 6

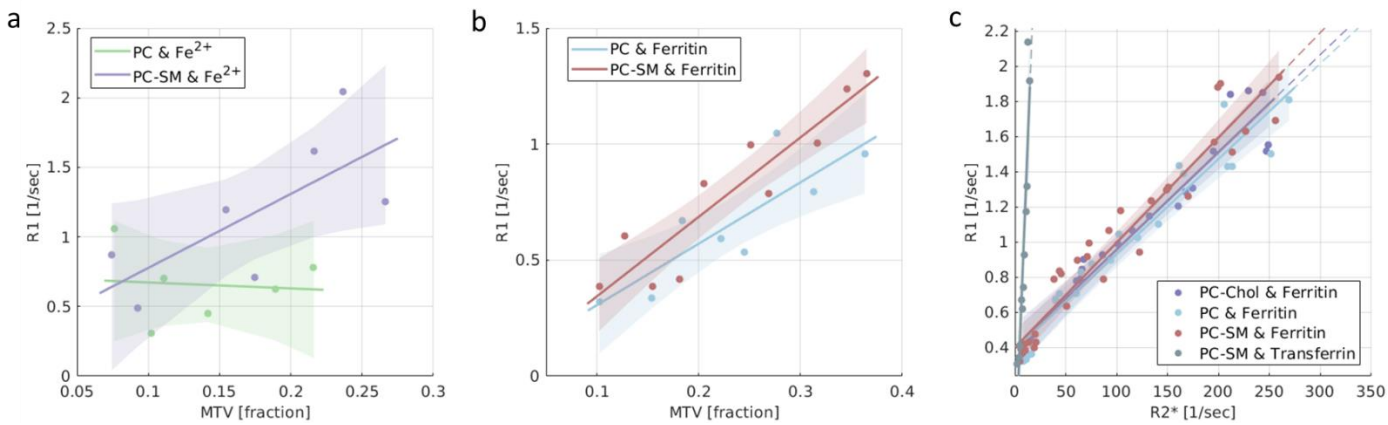

Sup. Figure 6: The r1-r2* relaxivity is stable for different types of lipids, while the R1-MTV dependency is sensitive to the lipid type. (a) *The dependency of R1 on MTV for an iron ion compound (Fe^{2+}) mixed with two different lipids: phosphatidylcholine (PC, green) and a mixture of PC-sphingomyelin (PC-SM, blue). This result replicates the sensitivity of the MTV dependencies to lipid types[76] in Fe^{2+}-containing phantoms.* ***(b)*** *The dependency of R1 on MTV for a second iron compound (ferritin) mixed with the same two lipids (PC and PC-SM).* ***(c)*** *The dependency of R1 on R2* (r1-r2* relaxivity) for four different iron-lipid mixtures: ferritin-PC ferritin-PC-SM, transferrin-PC-SM and ferritin-PC-cholesterol (PC-Chol, blue). The r1-r2* relaxivity is similar for the different lipid types mixed with ferritin, and the main difference is between the iron binding proteins; i.e., transferrin sample and the ferritin samples.*

Supplementary Figure 7

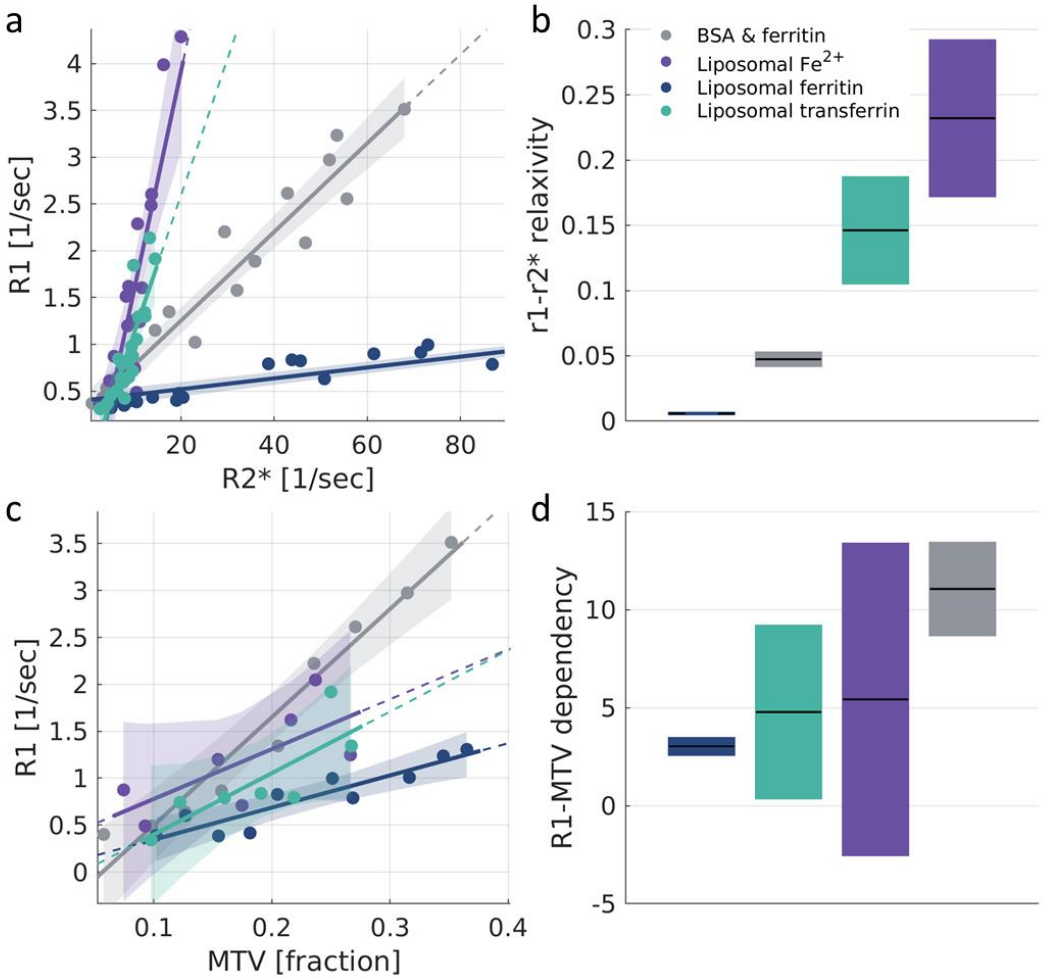

Sup. Figure 7: Iron environments are less distinguishable with MTV dependencies than with the r1-r2* relaxivity. (a) *The dependency of R1 on R2* (r1-r2* relaxivity) for different iron environments: liposomal-ferritin, BSA-ferritin mixture, liposomal transferrin and liposomal Fe^{2+}. Liposomal samples are based on PC-sphingomyelin. Data points represent samples with varying iron compounds concentrations relative to the water fraction. The linear relationships between relaxation rates are marked by lines, whose slopes represent the r1-r2* relaxivities. Dashed lines represent extrapolations of the linear fits. Shaded areas represent the 95% confidence bounds. The x-axis presents only partial range of R2* values, similar to* ***Figure 1d*** *(for the entire R2* range, see the inset of* ***Figure 1d****).* ***(b)*** *The r1-r2* relaxivities are different for these four iron environments. For each box, the central line marks the r1-r2* relaxivity, and the box shows the 95% confidence bounds of the linear fit.* ***(c)*** *The dependency of R1 on MTV for these four iron environments. Data points represent samples with varying iron compounds concentrations relative to the water fraction. The linear relationships between R1 and MTV are marked by lines, whose slopes represent the R1-MTV dependencies. Dashed lines represent extrapolations of the linear fits. Shaded areas represent the 95% confidence bounds.* ***(d)*** *The R1-MTV dependencies for the four iron environments. For each box, the central line marks the R1-MTV dependency, and the box showes the 95% confidence bounds of the linear fit.*

Supplementary Figure 8

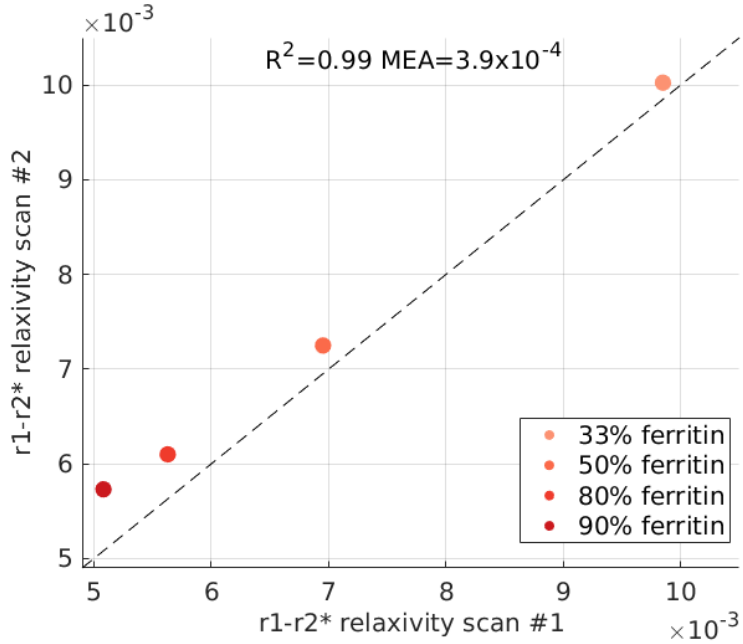

Sup. Figure 8: The reproducibility of the r1-r2* relaxivity measurement in vitro. *The reproducibility of the r1-r2* relaxivity measurement for in vitro ferritin-transferrin mixtures was estimated based on scan-rescan experiments. Four different transferrin-ferritin mixtures were scanned twice (on different days). Each mixture experiment had a different transferrin-ferritin fraction (different colors, legend shows the percentage of ferritin in the mixture). The r1-r2* relaxivity of each mixture experiment was calculated over samples with the same transferrin-ferritin fraction but varying total iron-binding protein concentrations. Figure shows the r1-r2* relaxivity values measured in the first scan (x-axis) vs. the r1-r2* relaxivity values measured in the second scan (y-axis) for each in vitro experiment. Dashed line is the identity line. The measured scan-rescan mean absolute error (MAE) represents an experimental estimate of the detection limit of the r1-r2* relaxivity.*

Supplementary Figure 9

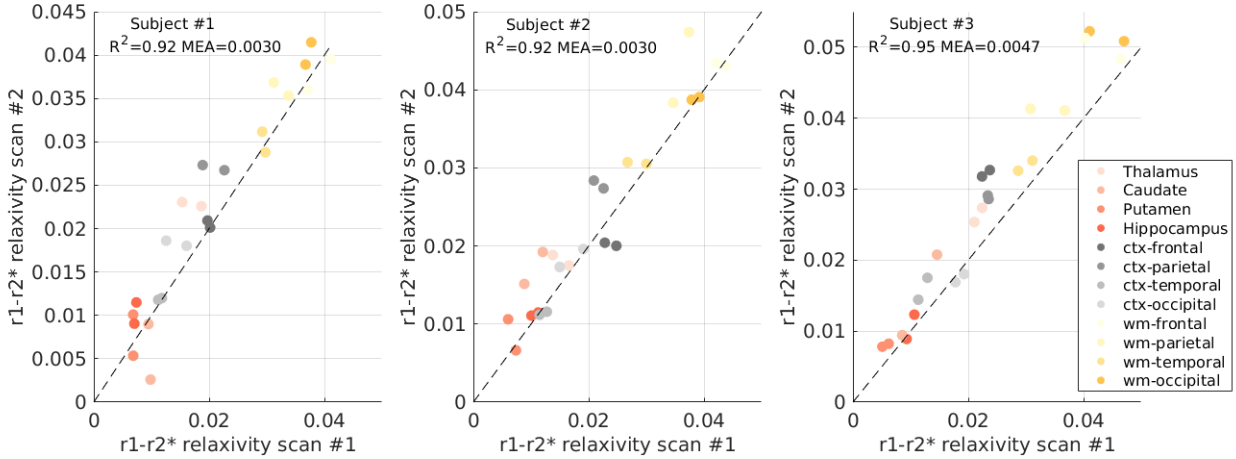

Sup. Figure 9: The reproducibility of the r1-r2* relaxivity measurement in the in vivo brain. *The reproducibility of the r1-r2* relaxivity measurement in the in vivo brain was estimated based on scan-rescan experiments in three human subjects. Each subject was scanned twice in the MRI (on different days). The r1-r2* relaxivity was calculated for each scan in 12 different brain regions (different colors) in both hemispheres. Panels show the r1-r2* relaxivity values measured in the first scan (x-axis) vs. the r1-r2* relaxivity values measured in the scanned scan for each subject. Dashed line is the identity line. The measured scan-rescan mean absolute error (MAE) represents an experimental estimate of the detection limit of the r1-r2* relaxivity.*

Supplementary Section 3: Voxel-wise r1-r2* relaxivity visualization.

Figure 2 and **Figure 4** compare the contrast of R1 and R2* in the brain to the new contrast generated by the r1-r2* relaxivity. The measurement of the r1-r2* relaxivity is calculated across all the voxels of a specific ROI in the brain (see "r1-r2* relaxivity computation for ROIs in the human brain" in Methods). Therefore, the contrasts are presented across different entire brain regions. In order to demonstrate a visualization of a voxel-wise r1-r2* relaxivity contrast, we generated representative maps of the local r1-r2* relaxivity in a healthy young subject and in a Meningioma patient. For this purpose, we used a moving-window approach, in which the r1-r2* relaxivity of each voxel is based on the local linear dependency of R1 on R2* in that voxel and all its neighboring voxels (125 voxels total, for more details see "Generating voxel-wise r1-r2* relaxivity visualizations" in Methods).

A comparison of the voxel-wise r1-r2* relaxivity to the R1 and R2* maps in the healthy brain can be seen in **Sup. Figure 10.** Similarly to the ROI-based approach (**Figure 2**), this voxel-wise comparison also shows that the r1-r2* relaxivity generates a new contrast in the brain compared to R1 and R2*. Interestingly, this local relaxivity contrast highlights the differences between superficial and deep white matter. Such contrast was previously suggested to be driven by the microscopic iron distribution[45].

In meningioma patients, we show that the ROI-based approach for the r1-r2* relaxivity allows to enhance the contrast between tumor tissue and non-pathological tissue without contrast agent injection (**Figure 4**). A comparison of the voxel-wise r1-r2* relaxivity to the R1 and R2* maps and to the Gd-enhanced contrast in a representative meningioma patient can be seen in **Sup. Figure 11**. In this example, the boundaries of the tumor can be separated from the surrounding non-pathological tissue based on the voxel-wise contrast of the r1-r2* relaxivity. Importantly, for this patient we were able to replicate our ROI-based results on the voxel-wise level (**Sup. Figure 12**). Across voxels, we find that the r1-r2* relaxivity allows to distinguish between tumor tissue and non-pathological tissue better than R1 and R2* (for example, effect size for the difference between tumor and gray matter is more than 10 times larger in the r1-r2* relaxivity compared to R1 and R2*).

Nonetheless, these representative visualizations merely provide preliminary evidence for the adaptiveness of the r1-r2* relaxivity approach for voxel-wise analyses. Notably, the presented implementation still has some limitations. First, the moving-window approach used for calculating the local r1-r2* relaxivity leads to inherent smoothing. As a result, this approach is sensitive to partial volume effects for voxels on the border between tissue types, which could be driving the observed contrast between superficial and deep white matter and between tumor tissue and non-pathological tissue. In

addition, the local computation of the r1-r2* relaxivity use fewer voxels compared to the ROI-based approach. It also does not include the binning procedure prior to the fitting which we used in the ROI-based approach. Therefore, this computation is less stable and is more sensitive to the inherent SNR of R1 and R2*, which is affected by magnetic field inhomogeneities, imperfections of the shim, and the heterogeneous magnetic susceptibility of the head. As a result, some of the calculated values in the brain are negative (4% of the voxels in the healthy subject and 11% of the voxels in the meningioma patient). These limitations should be accounted for prior to any future implementation of this voxel-wise approach for purposes other than visualization.

Supplementary Figure 10

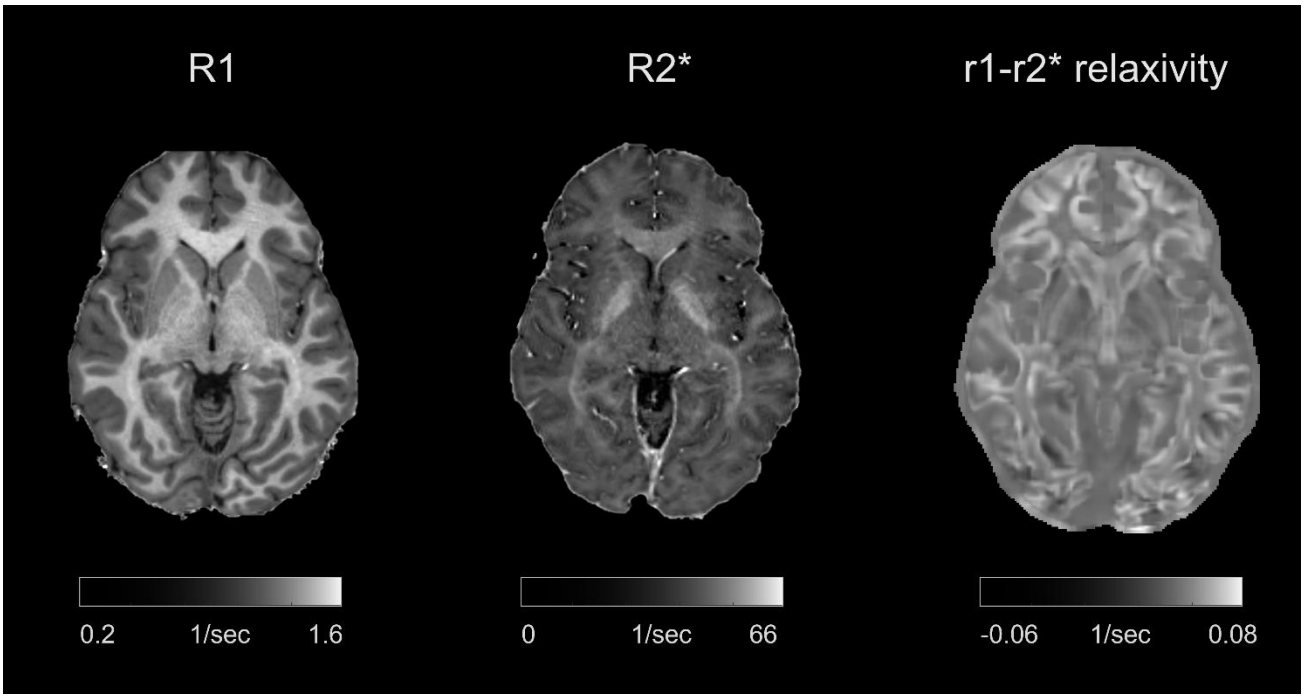

Sup. Figure 10: Voxel-wise comparison of the r1-r2* relaxivity map to R1 and R2* maps in the in vivo healthy brain. *The maps of R1 (left) and R2* (middle) are compared to the local r1-r2* relaxivity visualization (right) on a representative young healthy subject. The voxel-wise visualization of the r1-r2* relaxivity in the brain was generated based on the local linear dependency of R1 on R2* using a moving-window approach (for more details see "Generating voxel-wise r1-r2* relaxivity visualizations" in Methods).*

Supplementary Figure 11

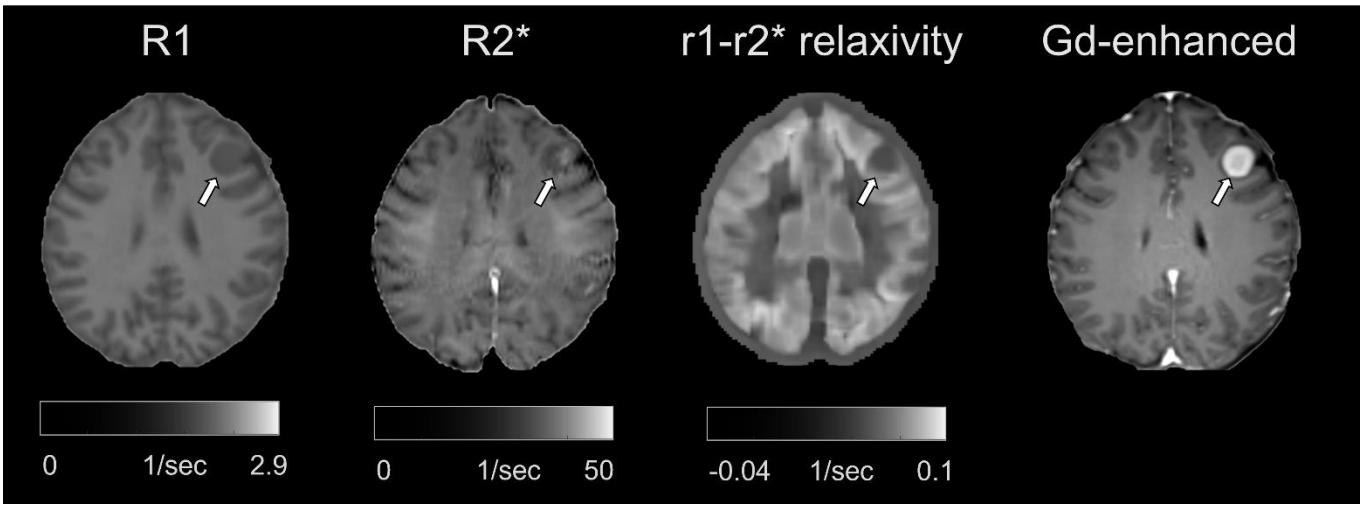

Sup. Figure 11: Voxel-wise comparison of the r1-r2* relaxivity map to R1 and R2* maps and to the Gd-enhanced contrast in the in vivo brain of a meningioma patient. *Representative visualization of R1, R2*, the voxel-wise r1-r2* relaxivity map and the Gd-enhanced contrast for a meningioma patient. Tumors are marked with arrows. The voxel-wise r1-r2* relaxivity map was generated based on the local linear dependency of R1 on R2* using a moving-window approach (for more details see "Generating voxel-wise r1-r2* relaxivity visualizations" in Methods).*

Supplementary Figure 12

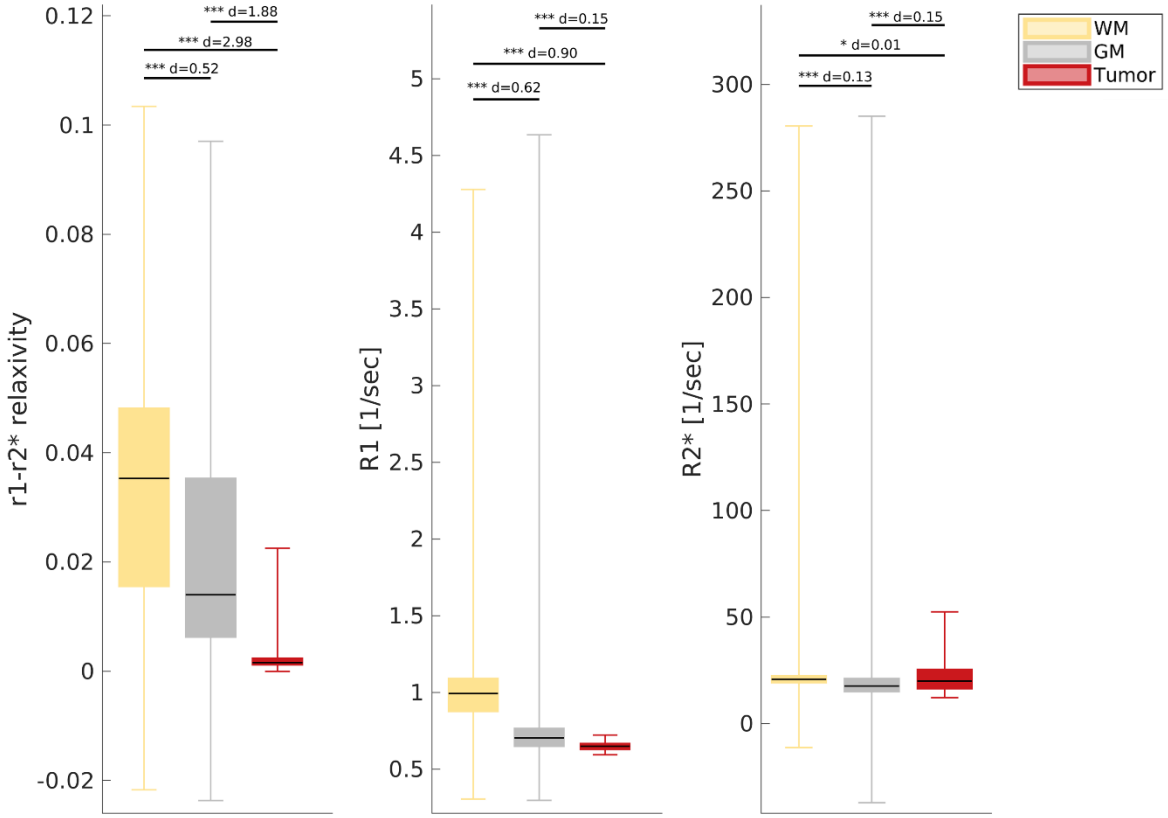

Sup. Figure 12: The voxel-wise r1-r2* relaxivity enhances the contrast between tumor tissue and non-pathological tissue on a representative meningioma patient. *Replication of the ROI-based results presented in figure 4d-f on the voxel-wise level. The contrast between the white matter (WM), gray matter (GM) and tumor tissues is presented for R1, R2* and the voxel-wise r1-r2* relaxivity. The variation in each box is calculated across voxels in a representative meningioma patient (Sup. Figure 11). The 25th, 50th and 75th percentiles and extreme data points are shown. The d-values represent the effect size (Cohen's d) of the differences between tissue types, and the significance level is based on a t-test. Across voxels, the r1-r2* relaxivity allows to distinguish between tumor tissue and non-pathological tissue better than R1 and R2*. Estimates in non-pathological tissues are for the tumor-free hemisphere. $p < 0.05$; $^{**}p < 0.01$; $^{***}p < 0.001$*

Supplementary Figure 13

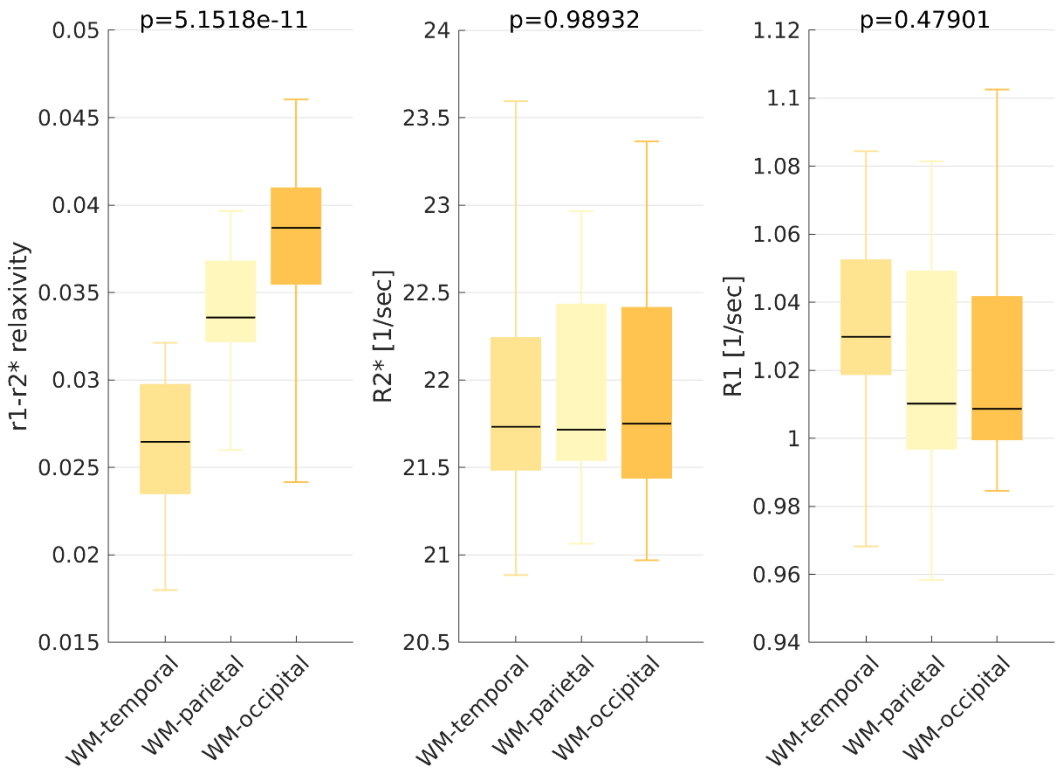

Sup. Figure 13: The new contrast of the r1-r2* relaxivity in white matter. *From left to right, r1-r2* relaxivity, R2* and R1 for three different white-matter (WM) ROIs (temporal, parietal and occipital). We can separate these three WM ROIs with the r1-r2* relaxivity but not with either R2* or R1. Boxes represent the variation in the MRI parameters across normal subjects (age 27±2, N = 21). The 50th percentile (horizontal black lines) 25th and 75th percentiles (box edges) and extreme data points (whiskers) are shown for each box. p-values are for the ANOVA test.*

Supplementary Figure 14

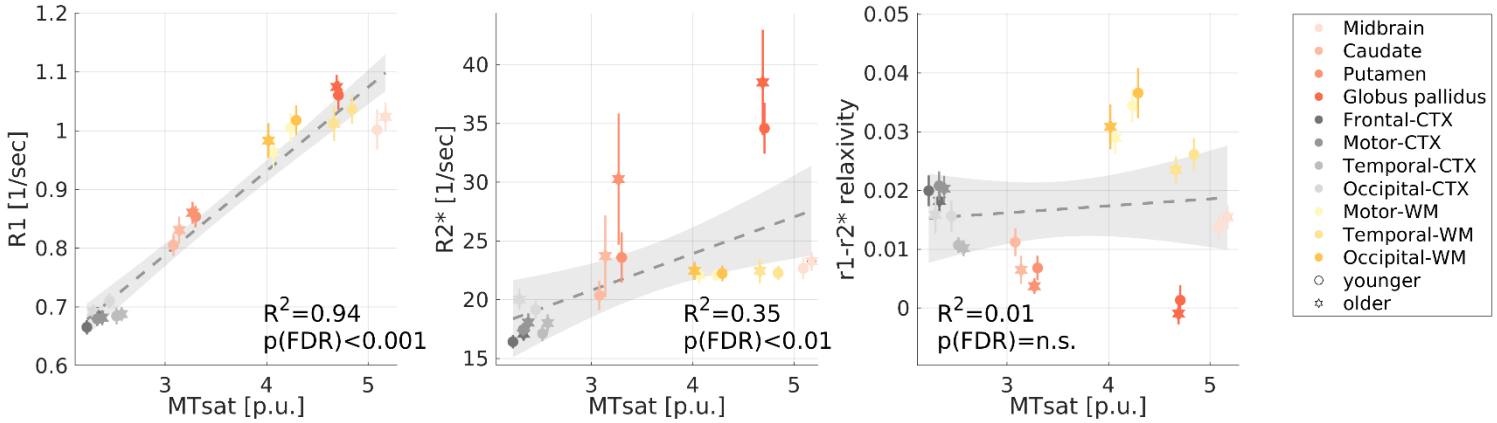

Sup. Figure 14: The correlations of MRI parameters with MTsat. *The qMRI measurement of the magnetization transfer saturation (MTsat) vs. R1, R2* and the r1-r2* relaxivity measured in vivo across younger (aged 23-63 years, N =26) and older (aged 65-77 years, N=13) subjects (different marker shapes) in 10 brain regions (different colors). Unlike R1 and R2*, the r1-r2* relaxivity is not significantly correlated with MTsat.*

Supplementary Figure 15

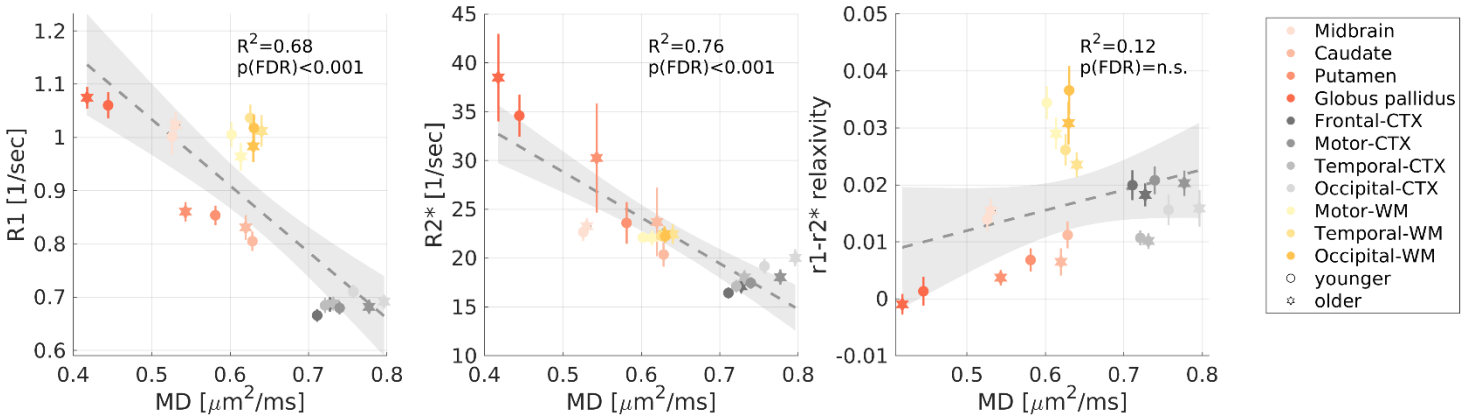

Sup. Figure 15: The correlations of MRI parameters with MD. *The qMRI measurement of the mean diffusivity (MD) measured in vivo across younger (aged 23-63 years, N =25) and older (aged 65-77 years, N=12) subjects vs. R1, R2* and the r1-r2* relaxivity measured in vivo across younger (aged 23-63 years, N =26) and older (aged 65-77 years, N=13) subjects (different marker shapes) in 10 brain regions (different colors). Unlike R1 and R2*, the r1-r2* relaxivity is not significantly correlated with MD.*

Supplementary Figure 16

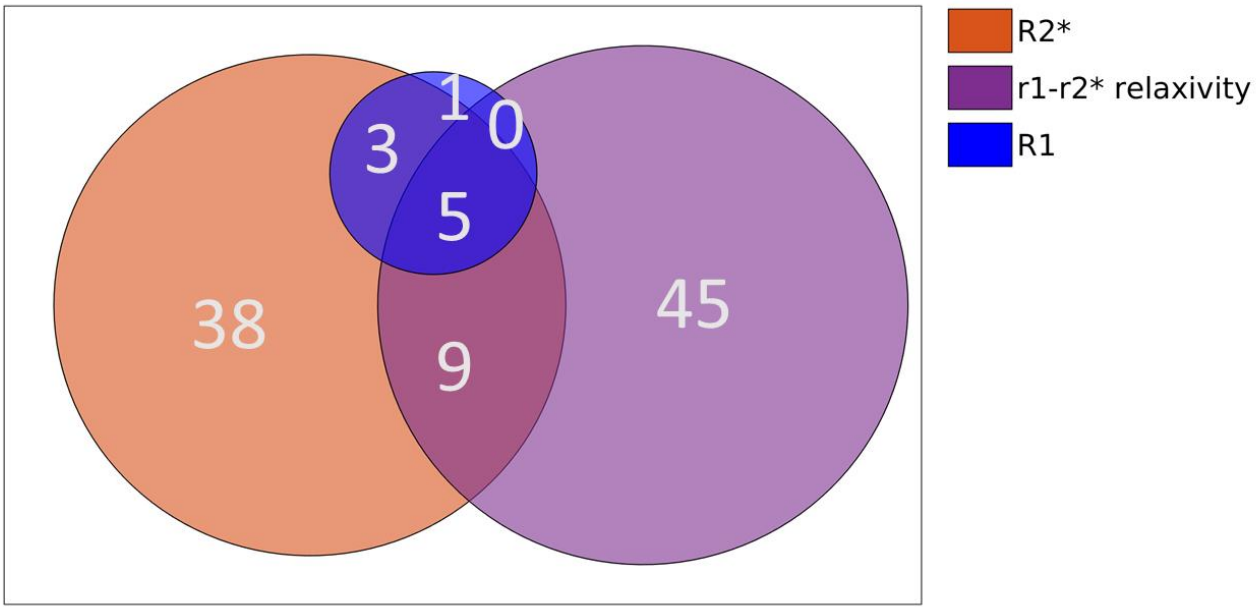

Sup. Figure 16: The number of significantly enriched pathways associated with each qMRI parameter. *The Venn diagram shows the number of significantly enriched pathways (p(FWER)<0.01) for each qMRI parameter (R2*, R1 and the r1-r2* relaxivity). Almost half of the significantly enriched pathways are exclusive for the r1-r2* relaxivity. See also supplementary table 1.*

Supplementary Table 1:

pathway	R1 NES	R1 pval	R2* NES	R2* pval	r1-r2* relaxivity NES	r1-r2* relaxivity pval
GO ALPHA BETA T CELL ACTIVATION	1.15	1	2.43	0.001	-1.12	1
GO ALPHA BETA T CELL DIFFERENTIATION	1.26	1	2.44	0.001	-1.04	1
GO ANTIGEN BINDING	0.79	1	2.23	0.024	-2.86	0
GO B CELL MEDIATED IMMUNITY	-0.64	1	1.48	1	-2.56	0
GO B CELL RECEPTOR SIGNALING PATHWAY	0.97	1	2.21	0.038	-2.50	0
GO CD4 POSITIVE ALPHA BETA T CELL ACTIVATION	0.99	1	2.32	0.005	-1.22	1
GO CD4 POSITIVE ALPHA BETA T CELL DIFFERENTIATION	1.22	1	2.38	0.003	-1.20	1
GO COMPLEMENT ACTIVATION	-0.86	1	1.33	1	-2.90	0
GO CONDENSED NUCLEAR CHROMOSOME CENTROMERIC REGION	-2.33	0.004	-1.64	1	-1.46	1
GO COTRANSLATIONAL PROTEIN TARGETING TO MEMBRANE	2.55	0.001	2.44	0.001	3.18	0
GO CYTOSOLIC LARGE RIBOSOMAL SUBUNIT	2.31	0.019	2.27	0.012	2.95	0
GO CYTOSOLIC RIBOSOME	2.21	0.112	2.57	0	3.06	0
GO CYTOSOLIC SMALL RIBOSOMAL SUBUNIT	1.73	1	2.38	0.003	2.44	0.003
GO DEFENSE RESPONSE TO BACTERIUM	0.78	1	1.76	1	-2.27	0.006
GO ESTABLISHMENT OF PROTEIN LOCALIZATION TO ENDOPLASMIC RETICULUM	2.11	0.317	2.08	0.272	3.14	0
GO FC RECEPTOR MEDIATED STIMULATORY SIGNALING PATHWAY	1.29	1	1.65	1	-2.29	0.004
GO HUMORAL IMMUNE RESPONSE	0.72	1	1.72	1	-2.43	0
GO HUMORAL IMMUNE RESPONSE MEDIATED BY CIRCULATING IMMUNOGLOBULIN	-0.52	1	1.61	1	-3.10	0
GO IMMUNE RECEPTOR ACTIVITY	1.27	1	2.46	0	0.71	1
GO IMMUNOGLOBULIN COMPLEX	-1.14	1	2.52	0	-3.62	0
GO IMMUNOGLOBULIN COMPLEX CIRCULATING	0.94	1	2.32	0.005	-3.14	0
GO IMMUNOGLOBULIN RECEPTOR BINDING	0.72	1	2.30	0.008	-3.06	0
GO KINETOCHORE	-2.00	0.594	-2.40	0.002	-0.94	1
GO LARGE RIBOSOMAL SUBUNIT	0.91	1	1.13	1	2.59	0
GO METAPHASE ANAPHASE TRANSITION OF CELL CYCLE	-2.10	0.219	-2.55	0	-0.81	1
GO MITOCHONDRIAL GENE EXPRESSION	-2.18	0.067	-2.45	0	1.57	1
GO MITOCHONDRIAL TRANSLATION	-2.08	0.266	-2.44	0	1.82	0.998
GO MITOCHONDRIAL TRANSLATIONAL TERMINATION	-2.05	0.388	-2.58	0	1.73	1
GO MITOTIC METAPHASE PLATE CONGRESSION	-1.80	1	-2.41	0.002	1.05	1
GO MITOTIC NUCLEAR DIVISION	-2.12	0.156	-2.32	0.009	-0.85	1
GO MITOTIC SISTER CHROMATID SEGREGATION	-2.19	0.059	-2.36	0.005	0.85	1
GO NEGATIVE REGULATION OF CHROMOSOME SEGREGATION	-2.01	0.548	-2.35	0.007	-0.84	1
GO NEGATIVE REGULATION OF METAPHASE ANAPHASE TRANSITION OF CELL CYCLE	-2.13	0.155	-2.46	0	-0.98	1
GO NUCLEAR TRANSCRIBED MRNA CATABOLIC PROCESS NONSENSE MEDIATED DECAY	2.25	0.059	2.36	0.003	2.49	0.001
GO PHAGOCYTOSIS RECOGNITION	-0.69	1	1.60	1	-2.89	0
GO POSITIVE REGULATION OF B CELL ACTIVATION	-0.51	1	1.50	1	-2.35	0.001
GO POSITIVE REGULATION OF LEUKOCYTE CELL CELL ADHESION	0.91	1	2.32	0.003	-1.06	1
GO POSITIVE T CELL SELECTION	1.14	1	2.45	0.001	0.92	1
GO PROTEIN LOCALIZATION TO ENDOPLASMIC RETICULUM	2.16	0.195	1.98	0.711	2.93	0
GO PROTEIN TARGETING TO MEMBRANE	1.83	0.998	1.71	1	2.50	0.001
GO REGULATION OF B CELL ACTIVATION	0.68	1	1.84	0.995	-2.29	0.004
GO REGULATION OF CHROMOSOME SEPARATION	-2.06	0.34	-2.49	0	-0.84	1
GO REGULATION OF HUMORAL IMMUNE RESPONSE	-1.03	1	1.24	1	-2.59	0
GO REGULATION OF SISTER CHROMATID SEGREGATION	-1.94	0.878	-2.43	0	-0.80	1
GO RIBOSOMAL SUBUNIT	0.93	1	1.41	1	2.79	0
GO RIBOSOME	-0.80	1	1.25	1	2.64	0
GO SMALL RIBOSOMAL SUBUNIT	-0.91	1	1.43	1	2.40	0.007
GO STRUCTURAL CONSTITUENT OF RIBOSOME	1.07	1	1.49	1	2.91	0
GO TRANSLATIONAL INITIATION	1.93	0.951	2.05	0.401	2.47	0.001
GO TRANSLATIONAL TERMINATION	-1.98	0.68	-2.51	0	1.83	0.997
GO T CELL ACTIVATION INVOLVED IN IMMUNE RESPONSE	1.27	1	2.46	0	-1.22	1
GO T CELL RECEPTOR COMPLEX	-0.60	1	2.35	0.003	0.65	1
GO T CELL SELECTION	1.21	1	2.58	0	1.06	1
GO UNFOLDED PROTEIN BINDING	-1.08	1	-2.34	0.007	1.36	1
KEGG LEISHMANIA INFECTION	1.70	1	2.44	0.001	1.01	1
KEGG RIBOSOME	2.53	0.001	2.68	0	3.10	0
PID IL12 2PATHWAY	0.99	1	2.35	0.003	-1.04	1
PID PLK1 PATHWAY	-2.61	0	-2.38	0.003	-1.27	1
PID TCR PATHWAY	0.81	1	2.37	0.003	-0.94	1
REACTOME ACTIVATION OF THE MRNA UPON BINDING OF THE CAP BINDING COMPLEX AND EIFS AND SUBSEQUENT BINDING TC	2.26	0.056	2.23	0.022	2.75	0
REACTOME ANTIGEN ACTIVATES B CELL RECEPTOR BCR LEADING TO GENERATION OF SECOND MESSENGERS	0.80	1	1.91	0.947	-3.01	0
REACTOME BINDING AND UPTAKE OF LIGANDS BY SCAVENGER RECEPTORS	-0.75	1	1.58	1	-2.74	0
REACTOME CD22 MEDIATED BCR REGULATION	-1.40	1	2.18	0.073	-3.25	0
REACTOME CELL CYCLE CHECKPOINTS	-2.17	0.073	-2.54	0	-1.00	1
REACTOME COMPLEMENT CASCADE	-1.04	1	0.94	1	-2.78	0
REACTOME CREATION OF C4 AND C2 ACTIVATORS	-0.99	1	1.52	1	-3.07	0
REACTOME CYCLIN A B1 B2 ASSOCIATED EVENTS DURING G2 M TRANSITION	-2.34	0.004	-2.45	0	-0.97	1
REACTOME EUKARYOTIC TRANSLATION ELONGATION	2.67	0	2.80	0	3.19	0
REACTOME EUKARYOTIC TRANSLATION INITIATION	2.56	0.001	2.60	0	3.23	0
REACTOME FCERI MEDIATED CA 2 MOBILIZATION	1.18	1	2.11	0.172	-2.91	0
REACTOME FCERI MEDIATED MAPK ACTIVATION	0.89	1	1.78	1	-2.88	0
REACTOME FCGAMMA RECEPTOR FCGR DEPENDENT PHAGOCYTOSIS	1.40	1	1.61	1	-2.41	0
REACTOME FCGR3A MEDIATED IL10 SYNTHESIS	0.76	1	1.93	0.891	-2.86	0
REACTOME FCGR ACTIVATION	0.97	1	2.01	0.558	-3.27	0
REACTOME GENERATION OF SECOND MESSENGER MOLECULES	1.34	1	2.57	0	1.17	1
REACTOME IMMUNOREGULATORY INTERACTIONS BETWEEN A LYMPHOID AND A NON LYMPHOID CELL	0.52	1	2.39	0.003	-2.21	0.02
REACTOME INFLUENZA INFECTION	1.42	1	1.79	1	2.70	0
REACTOME INITIAL TRIGGERING OF COMPLEMENT	-0.86	1	1.42	1	-3.05	0
REACTOME INTERLEUKIN 10 SIGNALING	0.72	1	1.92	0.929	-2.45	0
REACTOME MITOCHONDRIAL TRANSLATION	-2.06	0.339	-2.48	0	1.80	1
REACTOME MITOTIC METAPHASE AND ANAPHASE	-1.99	0.624	-2.46	0	1.20	1
REACTOME MITOTIC PROMETAPHASE	-1.89	0.969	-2.34	0.007	-0.83	1
REACTOME MITOTIC SPINDLE CHECKPOINT	-2.21	0.042	-2.69	0	-0.71	1
REACTOME NONSENSE MEDIATED DECAY NMD	2.28	0.039	2.42	0.001	2.66	0
REACTOME PARASITE INFECTION	0.90	1	1.39	1	-2.59	0
REACTOME REGULATION OF EXPRESSION OF SLITS AND ROBOS	1.49	1	1.83	0.999	2.52	0.001
REACTOME RESOLUTION OF D LOOP STRUCTURES THROUGH SYNTHESIS DEPENDENT STRAND ANNEALING SDSA	-2.15	0.101	-2.43	0	-1.38	1
REACTOME RESOLUTION OF SISTER CHROMATID COHESION	-2.31	0.005	-2.71	0	-0.72	1
REACTOME RESPONSE OF EIF2AK4 GCN2 TO AMINO ACID DEFICIENCY	2.21	0.111	2.55	0	2.73	0
REACTOME ROLE OF LAT2 NTAL LAB ON CALCIUM MOBILIZATION	1.12	1	1.94	0.852	-3.13	0
REACTOME ROLE OF PHOSPHOLIPIDS IN PHAGOCYTOSIS	1.41	1	2.25	0.016	-3.04	0
REACTOME RRNA PROCESSING	0.91	1	1.32	1	2.69	0
REACTOME SCAVENGING OF HEME FROM PLASMA	1.37	1	2.20	0.038	-3.27	0
REACTOME SELENOAMINO ACID METABOLISM	1.87	0.993	2.31	0.008	2.95	0
REACTOME SEPARATION OF SISTER CHROMATIDS	-2.05	0.363	-2.54	0	1.10	1
REACTOME SIGNALING BY ROBO RECEPTORS	1.61	1	1.90	0.961	2.40	0.007
REACTOME SRP DEPENDENT COTRANSLATIONAL PROTEIN TARGETING TO MEMBRANE	2.30	0.027	2.24	0.021	3.14	0
REACTOME TRANSLATION	-1.14	1	-1.34	1	2.93	0
WP CYTOPLASMIC RIBOSOMAL PROTEINS	2.71	0	2.77	0	3.17	0
WP MICROGLIA PATHOGEN PHAGOCYTOSIS PATHWAY	1.79	0.999	2.61	0	1.63	1
WP TYROBP CAUSAL NETWORK	2.30	0.024	2.83	0	1.16	1

Sup. Table 1: Significantly enriched pathways for R1, R2* and the r1-r2* relaxivity. *For each of the 101 gene sets, we show the normalized enrichments score (NES) for each of the three qMRI parameters, along with the FWER-corrected p-value. This table was used for the clustering shown in* ***Figure 5b****.*

Supplementary Figure 17

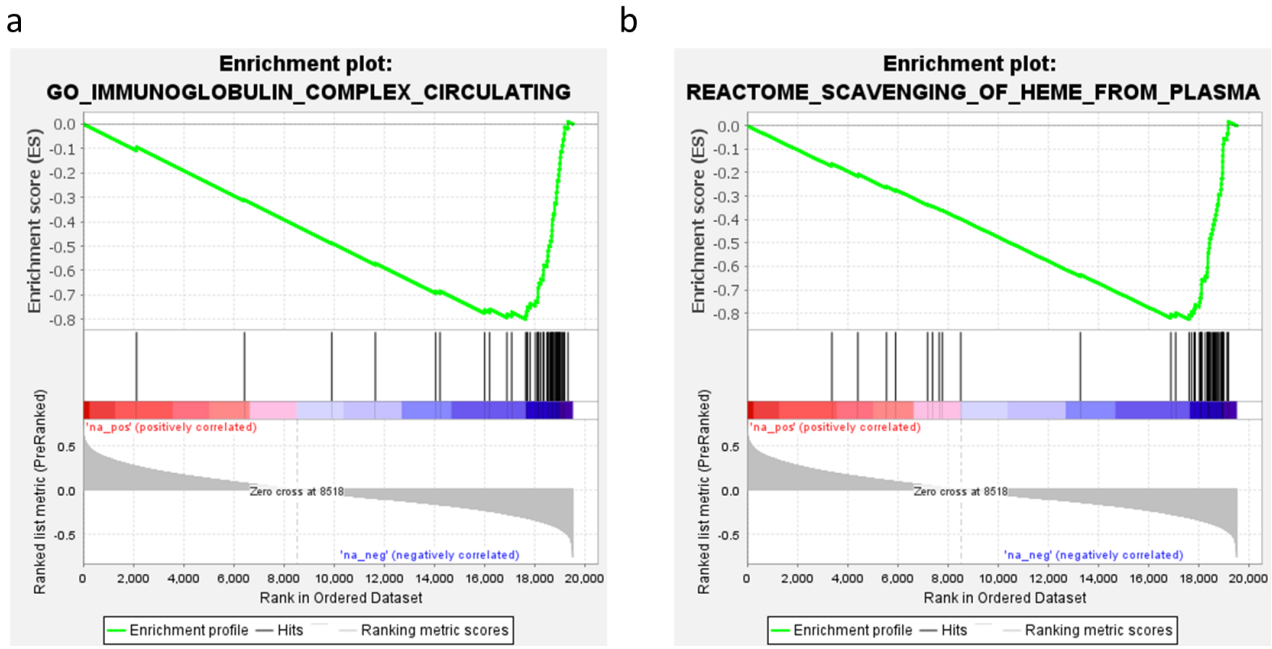

Sup. Figure 17: Enrichment plots of the two most enriched pathways for the r1-r2* relaxivity. *Gene enrichment plots of the two most enriched pathways for the r1-r2* relaxivity "Immunoglobulin complex"* ***(a)*** *and "scavenging of heme from plasma"* ***(b)****. The top portion of each panel shows the running enrichment score for the gene set as the analysis goes over the ranked list of genes. The list is based on the genes' correlation with the r1-r2* relaxivity. The middle portion of each panel shows where the members of the gene set appear in the ranked list of genes. The bottom portion of each panel shows the r value of the correlation between genes and the r1-r2* relaxivity. The two gene sets preferentially fall toward the negative end of the correlation spectrum, indicating their significant association with the r1-r2* relaxivity.*

Supplementary Figure 18

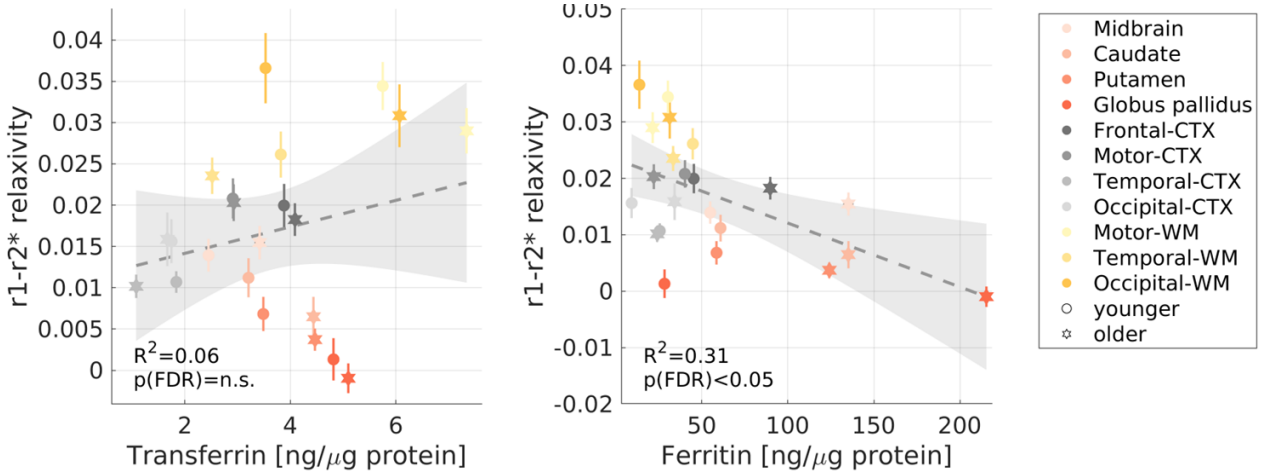

Sup. Figure 18: The correlations of the r1-r2* relaxivity with the transferrin and ferritin concentrations. *The transferrin and ferritin concentrations (postmortem, from the literature[5,7,9]) in different brain regions of younger (aged 27-64 years, N>=7) and older (aged 65-88 years, N>=8) subjects vs. the r1-r2* relaxivity measured in vivo across younger (aged 23-63 years, N =26) and older (aged 65-77 years, N=13) subjects (different marker shapes) in 10 brain regions (different colors).*

Supplementary Section 4: Exploring the biophysical sources of the r1-r2* relaxivity.

Supplementary Section 4.1: The theoretical basis for the r1-r2* relaxivity of brain tissue.

Brain tissue contains a complex milieu of iron compounds with variable iron binding capacities and aggregation states and includes myelin. Here we will expand the biophysical model of the r1-r2* relaxivity ("*In vivo* iron relaxivity model" in Methods) for the case of a heterogenous iron environment and in the presence of myelin.

Assuming the iron environment of a myelinated tissue contains N different iron compounds, and under the assumption that water can freely diffuse, the MR relaxation rates can be expressed as[87,88]:

$$\text{S1)} \qquad R_1 = \sum_N r_{(1,i)}[i] + r_{(1,M)}[M] + C_1$$

$$\text{S2)} \qquad R_2^* = \sum_N r_{(2,i)}[i] + r_{(2,M)}[M] + C_2$$

Where $[i]$ is the concentration of the i'th iron compound, and $[M]$ is the myelin concentration. $r_{(1,i)}$ and $r_{(2,i)}$ are the R1- and R2*- relaxivities of the i'th iron compound. $r_{(1,M)}$ and $r_{(2,M)}$ are the R1- and R2*-relaxivities of myelin. C_1 and C_2 are constants which capture other non-iron and non-myelin contributions.

The r1-r2* relaxivity measurement is defined as the linear dependency of R1 on R2* within an ROI in the brain (or across *in vitro* samples). This is equivalent to the total change in R1 relative to the total change in R2* ($\frac{\Delta R_1}{\Delta R_2^*}$):

$$\text{S3)} \qquad \frac{\Delta R_1}{\Delta R_2^*} = \frac{\sum_N r_{(1,i)}[\Delta i] + r_{(1,M)}[\Delta M]}{\sum_N r_{(2,i)}[\Delta i] + r_{(2,M)}[\Delta M]}$$

Where $[\Delta i]$ and $[\Delta M]$ are the changes in the iron compounds and myelin concentrations within an ROI respectively.

Supplementary Section 4.2: The r1-r2* relaxivity of ferritin and transferrin mixtures *in vitro*.

First, we tested the theoretical formulation presented in eq. $S1$-S3 in an artificial environment of multiple iron compounds. For this aim, we constructed phantom experiments containing both ferritin and transferrin in a liposomal environment. In this synthetic toy model, the transferrin-ferritin fraction ($f = \frac{[Tf]}{[Ft]+[Tf]}$) represents an example for a feature of the molecular iron environment which should affect the

r1-r2* relaxivity. To test this assumption, the biophysical model shown in Supp. Section 4.1 can be further developed under the conditions of these phantom experiments:

When ferritin, transferrin and myelin are present, eq. S*1*-S2 can be expressed as:

$$\text{S4)} \qquad R_1 = r_{(1,Ft)}[Ft] + r_{(1,Tf)}[Tf] + r_{(1,M)}[M]$$

$$\text{S5)} \qquad R_2^* = r_{(2,Ft)}[Ft] + r_{(2,Tf)}[Tf] + r_{(2,M)}[M]$$

Where $[Ft]$, $[Tf]$ and $[M]$ are the ferritin, transferrin and myelin concentrations respectively. $r_{(1,Ft)}$, $r_{(1,Tf)}$ and $r_{(1,M)}$ are the R1-relaxivities of ferritin, transferrin and myelin respectively. $r_{(2,Ft)}$, $r_{(2,Tf)}$ and $r_{(2,M)}$ are the R2*-relaxivities of ferritin, transferrin and myelin respectively.

According to eq. S3, the r1-r2* relaxivity measurement is equivalent to the total change in R1 relative to the total change in R2* ($\frac{\Delta R_1}{\Delta R_2^*}$):

$$\text{S6)} \qquad \frac{\Delta R_1}{\Delta R_2^*} = \frac{r_{(1,Ft)}[\Delta Ft] + r_{(1,Tf)}[\Delta Tf] + r_{(1,M)}[\Delta M]}{r_{(2,Ft)}[\Delta Ft] + r_{(2,Tf)}[\Delta Tf] + r_{(2,M)}[\Delta M]}$$

Where $[\Delta Ft]$, $[\Delta Tf]$, and $[\Delta M]$ are the changes in the ferritin, transferrin and myelin concentrations across *in vitro* samples, respectively.

In the ferritin-transferrin mixtures experiments we tested four different transferrin-ferritin fractions ($f = \frac{[Tf]}{[Ft]+[Tf]}$). For each fraction, we prepared samples with varying ferritin and transferrin concentrations, while keeping the fixed fraction between them (**Sup. Figure 19**). This allowed us to fit the linear relationship between R1 and R2* (the r1-r2* relaxivity) for each transferrin-ferritin fraction (**Sup. Figure 20**).

Assuming the transferrin-ferritin fraction (f) remains fixed across the *in vitro* samples over which the r1-r2* relaxivity is calculated:

$$f = \frac{Tf_1}{Tf_1 + Ft_1} = \frac{Tf_0}{Tf_0 + Ft_0}$$

(defining $[\Delta Tf] = Tf_1 - Tf_0$ and $[\Delta Ft] = Ft_1 - Ft_0$).

Under this condition:

$$\text{S7)} \qquad f = \frac{[\Delta Tf]}{[\Delta Ft]+[\Delta Tf]} = \frac{[Tf]}{[Ft]+[Tf]}$$

And therefore eq. S6 can be expressed as:

$$\text{S8)} \qquad \frac{\Delta R_1}{\Delta R_2^*} = \frac{\left(f*r_{(1,Tf)}+(1-f)r_{(1,Ft)}\right)[\Delta iron]+r_{(1,M)}[\Delta M]}{\left(f*r_{(2,Tf)}+(1-f)r_{(2,Ft)}\right)[\Delta iron]+r_{(2,M)}[\Delta M]}$$

Where $[\Delta Ft] + [\Delta Tf] = [\Delta iron]$.

In the ferritin-transferrin mixtures experiments, the liposomal fraction, which mimics the effect of myelin, was fixed at 17.5%. Therefore, in this case $[\Delta M] = 0$ and eq. $\mathrm{S8}$ reduces to:

$$\text{S9)} \qquad \frac{\Delta R_1}{\Delta R_2^*} = \frac{\left(f*r_{(1,Tf)}+(1-f)r_{(1,Ft)}\right)[\Delta iron]}{\left(f*r_{(2,Tf)}+(1-f)r_{(2,Ft)}\right)[\Delta iron]} = \frac{\left(f*r_{(1,Tf)}+(1-f)r_{(1,Ft)}\right)}{\left(f*r_{(2,Tf)}+(1-f)r_{(2,Ft)}\right)}$$

Using the ferritin and transferrin relaxivities ($r_{(1/2,Tf/Ft)}$) measured for each liposomal iron compound individually (Figure 1a-c), we could test the prediction of this model. Notably, the theoretical r1-r2* relaxivities calculated with eq. $\mathrm{S9}$ were in agreement with the experimental r1-r2* relaxivities (**Sup. Figure 21**), validating the presented biophysical framework *in vitro*. Moreover, the differences in the r1-r2* relaxivities measured for different transferrin-ferritin fractions were above the detection limit of this MRI measurement as estimated in a scan-rescan experiment (MAE=$3.9*10^{-4}$, **Sup. Figure 8**). Therefore, this toy example demonstrates that the heterogeneity in the iron environment can produce measurable changes in the r1-r2* relaxivity, which are in agreement with the biophysical modeling of this measurement.

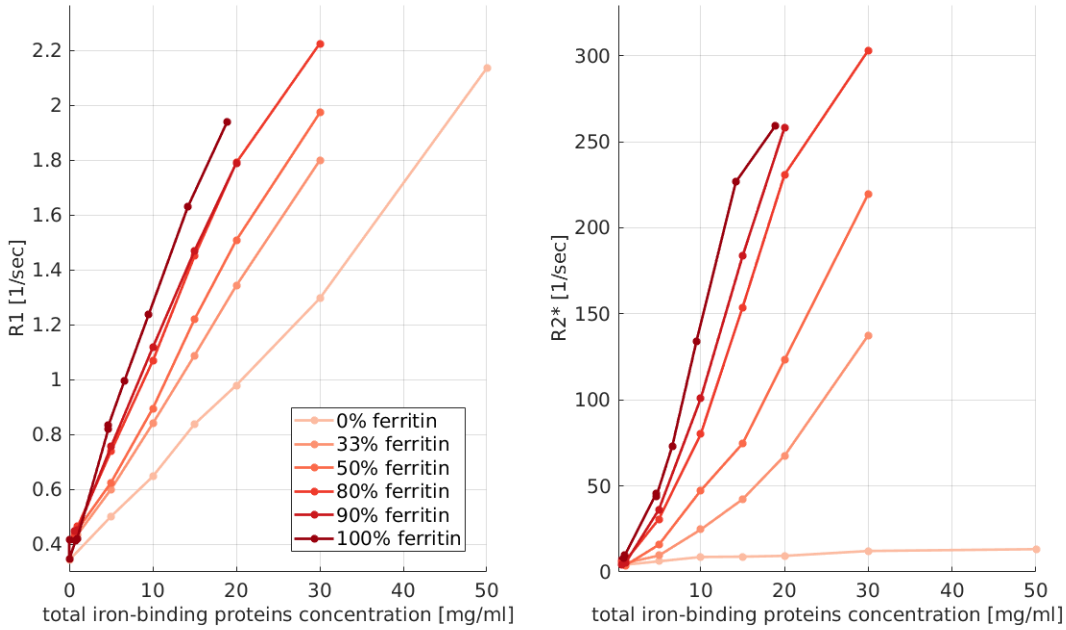

Sup. Figure 19: The dependency of R1 (left) and R2* (right) on the total iron-binding proteins concentration for four transferrin-ferritin mixtures. *Each mixture has a different transferrin-ferritin fraction (different colors, legend shows the percentage of ferritin in the mixture). Data points are different transferrin-ferritin samples, line connect between samples with the same transferrin-ferritin fraction and varying total iron-binding protein concentrations.*

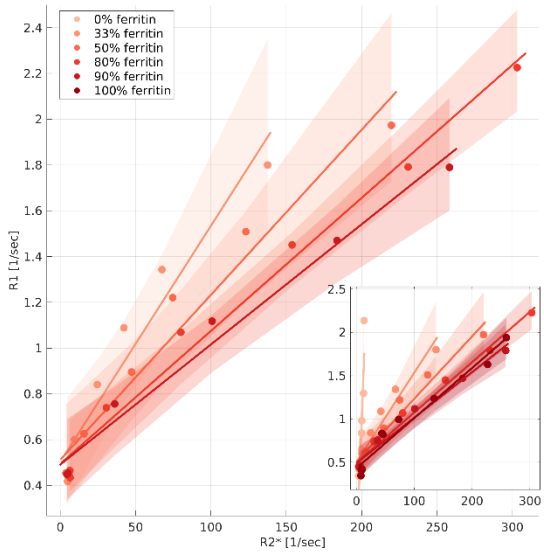

Sup. Figure 20: The dependency of R1 on R2* for four transferrin-ferritin mixtures. *Each mixture has a different transferrin-ferritin fraction (different colors, legend shows the percentage of ferritin in the mixture). Data points represent samples with varying total iron-binding proteins concentrations. The linear relationships of R1 and R2* are marked by lines. The slopes of these lines are the r1-r2* relaxivities. Shaded areas represent the 95% confidence bounds. Inset shows the pure ferritin (100% ferritin) and pure transferrin (0% ferritin) samples as well.*

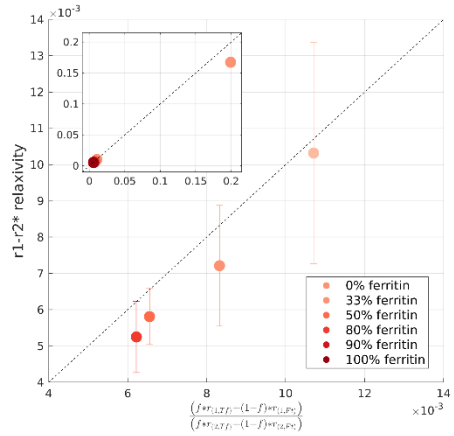

Sup. Figure 21: The theoretical r1-r2* relaxivities calculated with eq. S9 are in agreement with the experimental r1-r2* relaxivities. *The y-axis shows the r1-r2* relaxivity calculated for four transferrin-ferritin mixtures with different transferrin-ferritin fractions (different colors, Sup. Figure 20). Errorbars show the 95% confidence bounds. The x-axis shows the prediction for the r1-r2* relaxivity based on eq. S9. The ferritin and transferrin relaxivities in the equation were plugged in based on our experimental results for liposomal ferritin and liposomal transferrin samples (*Figure 1a-c*). f represents the transferrin-ferritin fractions and varies between data points. Dashed line is the identity line. Inset shows the data points for pure ferritin (100% ferritin) and pure transferrin (0% ferritin) samples as well. Note that for these pure samples the prediction is already presented in figure 1e.*

Supplementary Section 4.3: Numerical simulations of the r1-r2* relaxivity.

The phantom experiments of ferritin and transferrin mixtures allowed us to establish a theoretical framework for the r1-r2* relaxivity in an *in vitro* environment where only the iron concentration changes, and the liposomal fraction mimicking the myelin is fixed ($[\Delta M] = 0$). In the brain, we estimate the r1-r2* relaxivity across all voxels of an anatomically-defined ROI. Within brain tissue ROIs, both the iron and the myelin concentration may vary[45].

Importantly, rearranging eq. S8 we find that the strength of the myelin effect on the r1-r2* relaxivity depends on how variable is the myelin content within an ROI relative to how variable is the iron content ($\frac{[\Delta M]}{[\Delta iron]}$):

$$S10) \qquad \frac{\Delta R_1}{\Delta R_2^*} = \frac{\left(f * r_{(1,Tf)} + (1-f) r_{(1,Ft)}\right) + r_{(1,M)} \frac{[\Delta M]}{[\Delta iron]}}{\left(f * r_{(2,Tf)} + (1-f) r_{(2,Ft)}\right) + r_{(2,M)} \frac{[\Delta M]}{[\Delta iron]}}$$

In order to evaluate how the r1-r2* relaxivity is modulated by the molecular iron environment and by the myelin and iron variabilities within an ROI in the brain, we performed a set of numerical simulations. In these simulations, similar to the *in vitro* mixtures experiments, the transferrin-ferritin fraction ($f =$

$\frac{[Tf]}{[Ft]+[Tf]}$) represents an example for a feature of the molecular iron environment which should affect the r1-r2* relaxivity.

In these analyses we aim to simulate realistic concentrations of ferritin, transferrin and myelin, in order to achieve brain-like R1 and R2* values. Next, we follow our analysis pipeline; binning of the R2* and R1 measurements, excluding bins with small number of voxels, and assessing the r1-r2* relaxivity across the binned values. By varying the simulated content of the myelin and iron compounds we test to what extent each biological source contributes to the measurement of the r1-r2* relaxivity. First, we will examine our hypothesis that changes in the molecular iron environment, reflected by the transferrin-ferritin fraction, but not in the iron concentration, affect the r1-r2* relaxivity. We will then evaluate how the r1-r2* relaxivity is modulated by myelin. We will show that non-physiological conditions are required in order for the myelin by itself to fully explain the r1-r2* relaxivity changes measured in the brain.

Each numerical simulation was designed to mimic an ROI in the brain containing 1M voxels, with a fixed transferrin-ferritin fraction (f) across all voxels and varying myelin, transferrin and ferritin concentrations (**Sup. Table 2**). We synthetically generated R1 and R2* values for each voxel based on eq. $S4$-$S5$. The relaxivities of ferritin and transferrin ($r_{(1/2,Ft)}$, $r_{(1/2,Tf)}$) were taken from the results of our phantom experiments (**Figure 1**). In order to generate simulations that are as realistic as possible, the rest of the parameters were adapted from the human brain. The mean ferritin and transferrin concentrations (across all voxels of the ROI) were estimated based on post-mortem findings[5,7,9]. The myelin characteristics were simulated based on the qMRI measurement of the macromolecular tissue volume (MTV)[46], defined as 1-water fraction, which was shown to approximate the myelin content [48–52]. The myelin relaxivity ($r_{(1/2,M)}$) is defined as the dependency of relaxation rates on the myelin concentration[76]. We estimated the myelin relaxivity as the linear dependency of R1 and R2* on MTV, averaged across 16 ROIs in the brains of 21 young subjects. In order to assess the changes in myelin content within brain ROIs ($[\Delta M]$), we calculated the range of MTV values within white-matter (WM) or gray-matter (GM) regions averaged across 8 ROIs in the brains of 21 young subjects (**Sup. Figure 22**). Finally, the changes in ferritin and transferrin concentrations within brain ROIs ($[\Delta iron]$) were determined based on the range of R2* values within 16 WM and GM regions in the brains of 21 young subjects. We assumed that the changes in R2* not explained by MTV are related to changes in iron concentration (**Sup. Figure 23**):

$$\Delta(iron)R_2^* = \Delta(total)R_2^* - r_{(2,M)}[\Delta M]$$

We found that the total change in R2* within ROIs in the human brain is on average $\Delta(total)R_2^*$=9.0 1/sec, from which about 61% ($\Delta(iron)R_2^*$=5.6 1/sec) could be related to changes in iron concentration. Therefore, the simulated variably in the ferritin and transferrin concentrations were set to satisfy this requirement.

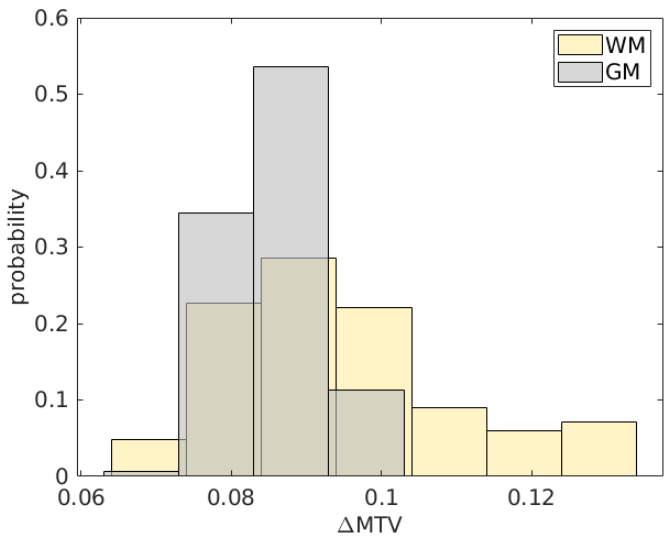

Sup. Figure 22: Change in MTV values ($[\Delta MTV]$) within white-matter (WM) or gray-matter (GM) regions. *ΔMTV values for gray matter (GM) and white matter (WM) are presented across 16 ROIs in the brains of 21 young subjects. For each ROI, we extracted the MTV values from all voxels and pooled them into 36 bins spaced equally between 0.05 and 0.40 [fraction]. We removed any bins in which the number of voxels was smaller than 4% of the total voxel count in the ROI. This was done so that the calculation will not be heavily affected by outlier voxels with extreme values. The median MTV of each bin was computed, and the difference between the highest and lowest binned MTV values was set as ΔMTV ([fraction]) in the ROI.*

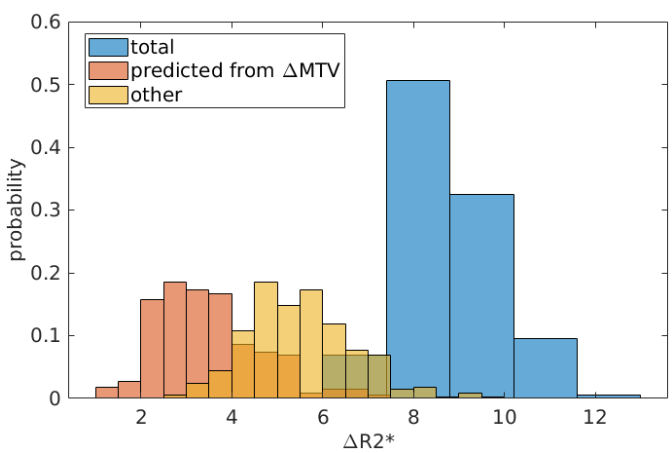

Sup. Figure 23: Myelin- and iron- related changes in R2* within brain regions. Total change in R2* values ($[\Delta R2*]$) within brain regions (blue histogram) *is presented across 16 ROIs in the brains of 21 young subjects. For each ROI, we extracted the R2* values from all voxels and pooled them into 36 bins spaced equally between 0 and 50. We removed any bins in which the number of voxels was smaller than 4% of the total voxel count in the ROI. This was done so that the calculation will not be heavily affected by outlier voxels with extreme values. The median R2* of each bin was computed, and the difference between the highest and lowest binned R2* values was set as ΔR2* in the ROI (in [1/sec]).* ***R2* changes related to myelin (orange histogram)*** *were estimated based on MTV; the change in R2* predicted from the change in MTV (ΔMTV) within each ROI was calculated as the linear dependency of R2* on MTV in the ROI multiplied by ΔMTV in the ROI ($r_{(2,M)}[\Delta M]$).* ***R2* changes related to iron (yellow histogram)*** *were estimated as the change in R2* not explained by the change in MTV.*

Parameter	*Value*	*Estimation method*
Transferrin-ferritin fraction (f)	0.1 or 0.2	Based on literature values[5,7,9].
R1-ferritin relaxivity ($r_{(1,Ft)}$)	0.067 [(sec^{-1})/(mg/wet ml)]	*In vitro* linear dependency of R1 on ferritin concentration
R2-ferritin relaxivity* ($r_{(2,Ft)}$)	11.2 [(sec^{-1})/(mg/wet ml)]	*In vitro* linear dependency of R2* on ferritin concentration
R1-transferrin relaxivity ($r_{(1,Tf)}$)	0.026 [(sec^{-1})/(mg/wet ml)]	*In vitro* linear dependency of R1 on transferrin concentration
R2-transferrin relaxivity* ($r_{(2,Tf)}$)	0.13 [(sec^{-1})/(mg/wet ml)]	*In vitro* linear dependency of R2* on transferrin concentration
Transferrin concentration ($[Tf]$)	0.025±0.025 [mg/wet ml]	Median is based on literature values[5,7,9]. Range across voxels was set so that the total change in R2* will mimic the physiological change of 6-12 [1/sec] (**Sup. Figure 23**)
Ferritin concentration ($[Ft]$)	$\left(\frac{1}{f}-1\right)[Tf]$	Set to satisfy the requirement for fixed transferrin-ferritin fraction (f) across all voxels.
Myelin concentration in WM ($[M]_{WM}$)	0.29±0.047 [fraction]	Brain *in vivo* MTV values
Myelin concentration in GM ($[M]_{GM}$)	0.19±0.043 [fraction]	Brain *in vivo* MTV values
R2-myelin relaxivity* ($r_{(2,M)}$)	38.8 [(sec^{-1})/fraction]	Brain *in vivo* linear dependency of R2* on MTV
R1-myelin relaxivity ($r_{(1,M)}$)	2.6 [(sec^{-1})/fraction]	Brain *in vivo* linear dependency of R1 on MTV

Sup. Table 2: simulation parameters.

An example result of the numerical simulation is presented in **Sup. Figure 24A**. It is evident that both the changes in myelin concentration across voxels of the simulated ROI (represented by different colors) and the changes in ferritin and transferrin concentrations across voxels (represented by the symbols size) affect the measured r1-r2* relaxivity. In our analysis pipeline we first bin the R1 and R2* values within the ROI and next calculate r1-r2* relaxivity over the binned values. Therefore, the variability in R1 for a given R2* bin is collapsed to an average R1 value (black data points). We assume that this approach eliminates some of the variability related to myelin. We hypothesized that the r1-r2* relaxivity is sensitive to the iron environment. Indeed, in our simulations we find that by setting different physiological transferrin-ferritin fractions and leaving the myelin parameters constant, the r1-r2* relaxivity changes considerably (**Sup. Figure 24**).

In addition, we hypothesized that the r1-r2* relaxivity less sensitive to the iron concentration and is more sensitive to the iron environment. To test this, we run two numerical simulations with the same transferrin-ferritin fraction but with different transferrin and ferritin concentrations. As expected, R1 and R2* values changed with increased ferritin and transferrin concentrations but the r1-r2* relaxivity did not change (**Sup. Figure 25**). This indicates that the r1-r2* relaxivity measurement is less

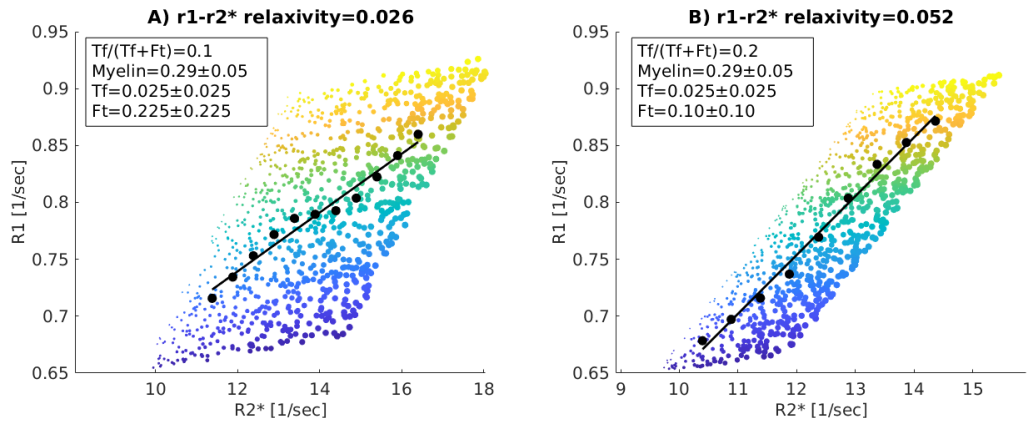

Sup. Figure 24: The r1-r2* relaxivity in two simulated ROIs with different transferrin-ferritin fractions (Tf/(Tf+Ft))*; (A) the transferrin-ferritin fraction is 0.1; (B) the transferrin-ferritin fraction is 0.2. Each figure shows the dependency of R1 on R2* for 1,000 representative simulated voxels. The colors of the data points indicate the variability in myelin concentration across voxels, and their sizes indicate the variability in iron compounds concentration across voxels (the simulated concentrations are shown in the text box, myelin is in units of [fraction] as MTV, transferrin and ferritin are in units of [mg/ml]). As in our in vivo pipeline, R2* and R1 values were binned (black data points represent the bins' median), and a linear fit was calculated (black line). The slopes of the linear fit (shown in the title) represent the dependency of R1 on R2* (r1-r2* relaxivity) and vary with the transferrin-ferritin fraction.*

sensitive to absolute changes in the iron concentration and is sensitive to the interplay between iron compounds, reflected in the simulations by the transferrin-ferritin fraction. In the brain, changes in the myelin content between GM and WM are known to substantially affect the measurements of R1 and R2*[4,19,25,29,40–44]. To test the potential contribution of the myelin to the r1-r2* relaxivity, we changed the myelin concentration in our simulation while keeping the rest of the parameters fixed. Setting the myelin concentration to that typical for GM or WM (as estimated *in vivo* by MTV) led to considerable changes in R1 and R2*, but did not produce any change in the r1-r2* relaxivity (**Sup. Figure 26**).

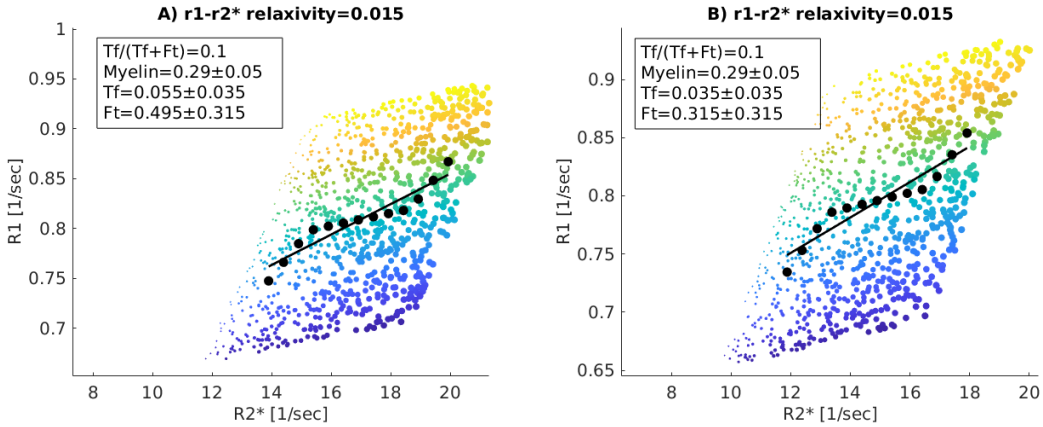

Sup. Figure 25: The r1-r2* relaxivity in two simulated ROIs with different transferrin and ferritin concentrations and a similar transferrin-ferritin fraction (Tf/(Tf+Ft)); *(A) a higher transferrin and ferritin*

concentrations and a transferrin-ferritin fraction of 0.1; (B) a lower transferrin and ferritin concentrations and a transferrin-ferritin fraction of 0.1. Each figure shows the dependency of R1 on R2 for 1,000 representative simulated voxels. The colors of the data points indicate the variability in myelin concentration across voxels, and their sizes indicate the variability in iron compounds concentration across voxels (the simulated concentrations are shown in the text box, myelin is in units of [fraction] as MTV, transferrin and ferritin are in units of [mg/ml]). As in our in vivo pipeline, R2* and R1 values were binned (black data points represent the bins' median), and a linear fit was calculated (black line). The slopes of the linear fit (shown in the title) represent the dependency of R1 on R2* (r1-r2* relaxivity) and do vary with the change in transferrin and ferritin concentrations.*

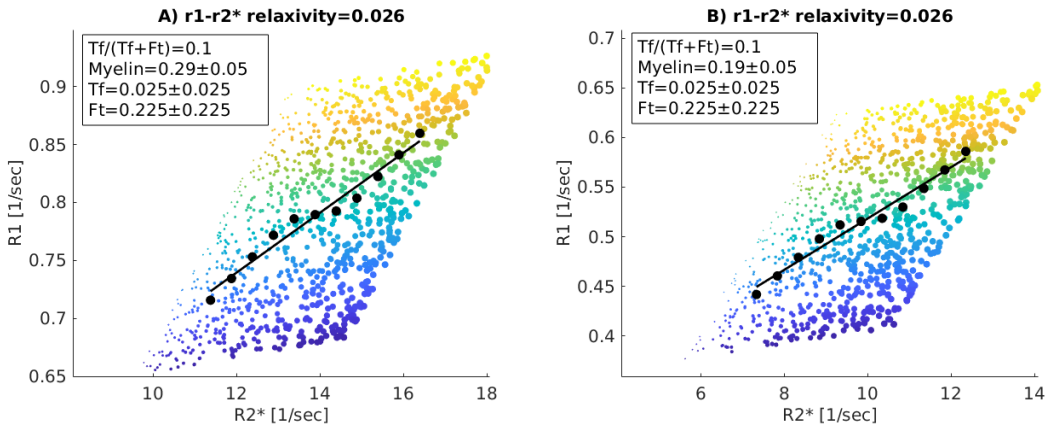

Sup. Figure 26: The r1-r2* relaxivity in two simulated ROIs with different myelin concentrations and similar transferrin-ferritin fractions (Tf/(Tf+Ft))*; (A) a higher myelin concentration and transferrin-ferritin fraction of 0.1; (B) a lower myelin concentration and transferrin-ferritin fraction of 0.1. Each figure shows the dependency of R1 on R2* for 1,000 representative simulated voxels. The colors of the data points indicate the variability in myelin concentration across voxels, and their sizes indicate the variability in iron compounds concentration across voxels (the simulated concentrations are shown in the text box, myelin is in units of [fraction] as MTV, transferrin and ferritin are in units of [mg/ml]). As in our in vivo pipeline, R2* and R1 values were binned (black data points represent the bins' median), and a linear fit was calculated (black line). The slopes of the linear fit (shown in the title) represent the dependency of R1 on R2* (r1-r2* relaxivity) and does not vary with the change in myelin concentration.*

The theoretical formulation presented here indicates that it is not the myelin concentration, but the variability in myelin within an ROI ($[\Delta M]$), that is important for determining the r1-r2* relaxivity (eq. S10). However, estimating the variability in myelin within ROIs *in vivo* based on the myelin marker MTV, we find that it only explains ~30% of the variation in the *in vivo* r1-r2* relaxivity measurements across the brain (**Sup. Figure 27**). In the simulations, setting both the range and concentration of myelin to the ones typical for WM or GM (as estimated by MTV, **Sup. Figure 22**), slightly changed the r1-r2* relaxivity (0.002, **Sup. Figure 28**). Importantly, changing the transferrin-ferritin fraction between the physiological values of 0.1-0.2 led to a change of 0.026 in the r1-r2* relaxivity (**Sup. Figure 24**). Therefore, the simulated changes related to the molecular iron environment were one order of magnitude bigger (**Sup. Figure 24**).

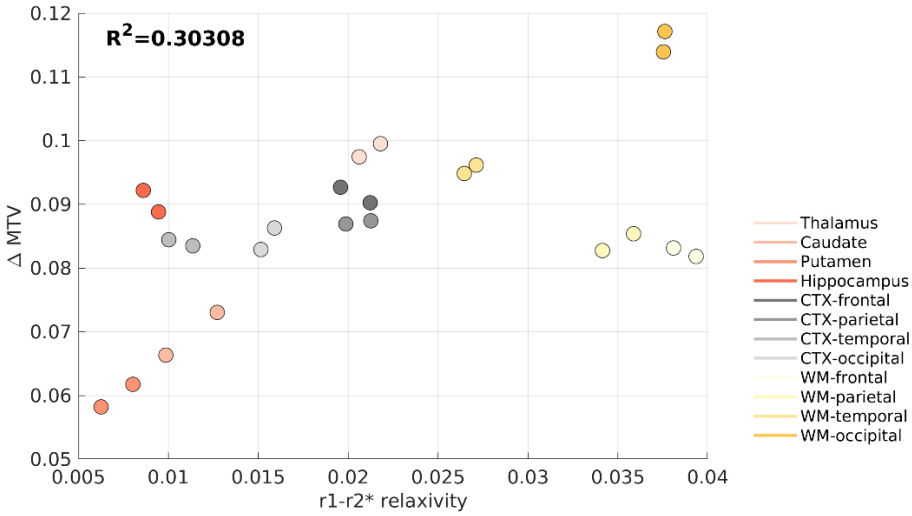

Sup. Figure 27: The in vivo estimates of the variability in myelin within ROIs vs. the in vivo r1-r2* relaxivity. *The average estimated myelin variability within ROIs, computed across the brains of 21 young subjects, vs. the average r1-r2* relaxivity for the same subjects. Brain regions are presented in different colors (each ROI has left and right hemisphere estimates). The variability in myelin within brain regions was estimated based on the variability in MTV across voxels of each ROI (ΔMTV, y-axis). For each ROI, we extracted the MTV values from all voxels and pooled them into 36 bins spaced equally between 0.05 and 0.40 [fraction]. We removed any bins in which the number of voxels was smaller than 4% of the total voxel count in the ROI. This was done so that the calculation will not be heavily affected by outlier voxels with extreme values. The median MTV of each bin was computed, and the difference between the highest and lowest binned MTV values was set as ΔMTV ([fraction]) in the ROI.*

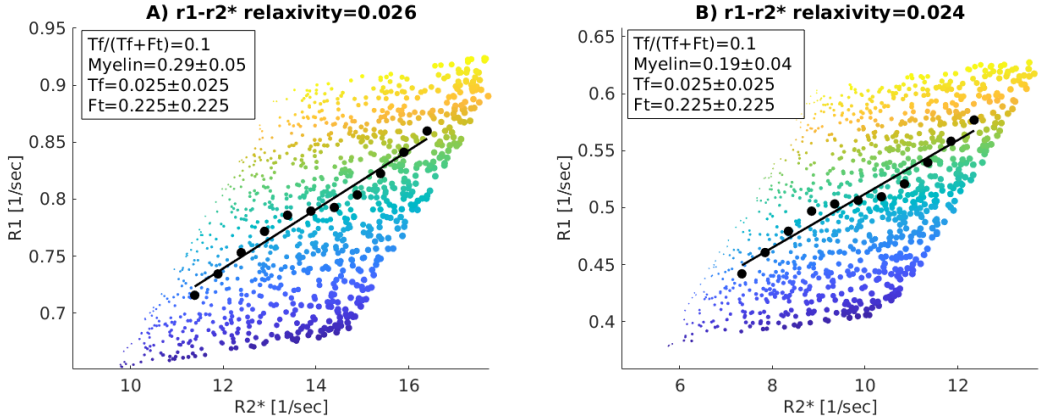

Sup. Figure 28: The r1-r2* relaxivity in two simulated ROIs with different myelin concentrations, different ranges of myelin concentrations ([ΔM]), and similar transferrin-ferritin fractions (Tf/(Tf+Ft))*; (A) WM; a higher myelin concentration and a larger range of myelin variability, the transferrin-ferritin fraction is 0.1; (B) GM; a lower myelin concentration and a lower range of myelin variability, the transferrin-ferritin fraction is 0.1. Each figure shows the dependency of R1 on R2* for 1,000 representative simulated voxels. The colors of the data points indicate the variability in myelin concentration across voxels, and their sizes indicate the variability in iron compounds concentration*

across voxels (the simulated concentrations are shown in the text box, myelin is in units of [fraction] as MTV, transferrin and ferritin are in units of [mg/ml]). As in our in vivo pipeline, R2 and R1 values were binned (black data points represent the bins' median), and a linear fit was calculated (black line). The slopes of the linear fit (shown in the title) represent the dependency of R1 on R2* (r1-r2* relaxivity) and vary slightly with the range of myelin variability ($[\Delta M]$).*

We further tested what are the myelin properties that would generate similar r1-r2* relaxivity effect as the effect observed when changing the transferrin-ferritin fraction (a change of 0.026 in the r1-r2* relaxivity, **Sup. Figure 24**). As changing the myelin concentration does not change the r1-r2* relaxivity (**Sup. Figure 26**), we changed the variability in myelin concentration within the ROI ($[\Delta M]$, **Sup. Figure 28**). We found that in order to generate a change of 0.026 in the r1-r2* relaxivity only through myelin-related changes (when the iron-related properties are fixed), the variability in MTV within the simulated ROI should be in the order of 0.187 [fraction] (**Sup. Figure 29**). Evaluating the *in vivo* variability in MTV within WM, GM and subcortical ROIs across 21 young subjects, the typical variability is ~ 0.09 [fraction], and the most extreme variability that was measured was 0.13 [fraction] (in the WM, **Sup. Figure 22**). Even this atypical value is still much lower than that required to generate a change of 0.026 in the r1-r2* relaxivity (0.187 [fraction] in MTV). Thus, while the variability in myelin within ROIs can affect the r1-r2* relaxivity, there are no physiological myelin properties that would fully explain the r1-r2* relaxivity effect measured in the brain.

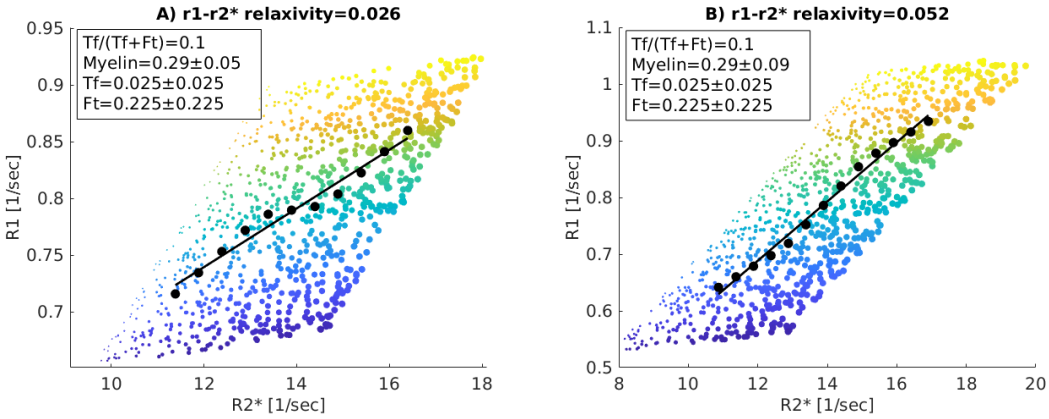

Sup. Figure 29: The r1-r2* relaxivity in two simulated ROIs with different extreme ranges of myelin concentrations ($[\Delta M]$) and similar transferrin-ferritin fractions (Tf/(Tf+Ft)); *(A) a physiological range of myelin variability, and a transferrin-ferritin fraction of 0.1; (B) the range of myelin variability is almost doubled, and the transferrin-ferritin fraction is 0.1. Each figure shows the dependency of R1 on R2* for 1,000 representative simulated voxels. The colors of the data points indicate the variability in myelin concentration across voxels, and their sizes indicate the variability in iron compounds concentration across voxels (the simulated concentrations are shown in the text box, myelin is in units of [fraction] as MTV, transferrin and ferritin are in units of [mg/ml]). As in our in vivo pipeline, R2* and R1 values were binned (black data points represent the bins' median), and a linear fit was calculated (black line). The*

slopes of the linear fit (shown in the title) represent the dependency of R1 on R2 (r1-r2* relaxivity) and change considerably under this condition of extreme variability in myelin concentration ($[\Delta M]$).*

The iron and myelin contents of brain tissue are tightly related, as iron is required for the formation of myelin[4]. To test how this affects the r1-r2* relaxivity measurement, we simulated a case where iron and myelin are completely correlated. Importantly, even in this extreme case, different transferrin-ferritin fractions exhibited different r1-r2* relaxivity (**Sup. Figure 30**).

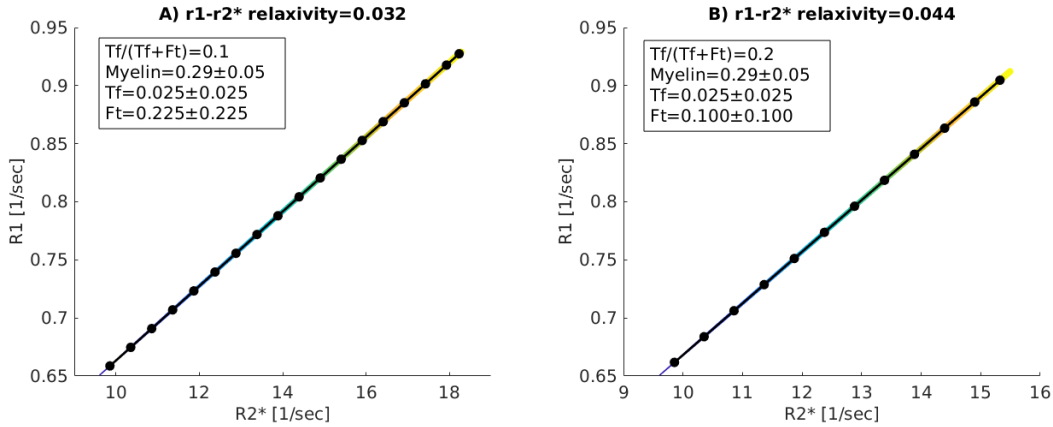

Sup. Figure 30 : The r1-r2* relaxivity in two simulated ROIs with different transferrin-ferritin fractions (Tf/(Tf+Ft)) and a correlation between iron and myelin concentrations across voxels*; (A) The transferrin-ferritin fraction is 0.1; (B) the transferrin-ferritin fraction is 0.2. In both A and B iron and myelin are correlated. Each figure shows the dependency of R1 on R2* for 1,000 representative simulated voxels. The colors of the data points indicate the variability in myelin concentration across voxels, and their sizes indicate the variability in iron compounds concentration across voxels (the simulated concentrations are shown in the text box, myelin is in units of [fraction] as MTV, transferrin and ferritin are in units of [mg/ml]). As in our in vivo pipeline, R2* and R1 values were binned (black data points represent the bins' median), and a linear fit was calculated (black line). The slopes of the linear fit (shown in the title) represent the dependency of R1 on R2* (r1-r2* relaxivity) and change considerably with the transferrin-ferritin fraction even when iron and myelin are correlated.*

To conclude, we simulated a brain-like environment in order to test the biological sources affecting the r1-r2* relaxivity measurement. We found that physiological changes in the molecular iron environment, represented in the simulations by the ferritin-transferrin fraction, led to considerable changes in the r1-r2* relaxivity (0.026). This effect could not be attributed to the absolute concentrations of iron compounds, only to the ratio between them. To estimate whether the effect of changing the molecular iron environment is measurable *in vivo*, we assessed the detection limit of the r1-r2* relaxivity measurement using scan-rescan experiments (**Sup. Figure 9**). We found that the changes in the r1-r2* relaxivity simulated by different physiological transferrin-ferritin ratios are well above the detection limit of this MRI measurement *in vivo* (MEA~0.0035). Importantly, our arguments regarding the sensitivity of

the r1-r2* relaxivity to the molecular iron environment are demonstrated in the simulations based on the example of the transferrin-ferritin ratio. However, it is evident from our theoretical formulation (S10) that the variability in iron concentration within an ROI contributes to the r1-r2* relaxivity as well. Therefore, while the transferrin-ferritin ratio was used as an example, other features of the iron environment such as the spatial variability of iron compounds, their binding capacities and aggregate sizes, could affect the r1-r2* relaxivity as well. Next, we confirmed that changes in the myelin concentration affect the measurements of R1 and R2*, but not the r1-r2* relaxivity. The myelin variability within an ROI can affect the r1-r2* relaxivity. However, we found that *in vivo* estimates of this myelin characteristic explains only 30% of the variation in the *in vivo* r1-r2* relaxivity measurement across the brain. In the simulation, setting the myelin variability within an ROI to typical GM and WM values led to a slight change in the r1-r2* relaxivity. However, we found that unrealistic myelin variability is required in order to produce the r1-r2* relaxivity effect observed for realistic changes in the transferrin-ferritin fraction. Therefore, while the myelin substantially affects the measurements of R1 and R2*, it is not the main component governing the measurement of the r1-r2* relaxivity, and under physiological conditions it cannot by itself explain the measured variability in the r1-r2* relaxivity across the brain.

Supplementary Section 5: The r1-r2* relaxivity in the pallidum.

The pallidum is unique in terms of its paramagnetic properties: it is highly rich in iron, but also contains iron oxides and metal depositions[3,89,90] which might affect the measurement of the r1-r2* relaxivity.

For young subjects, R1 and R2* values in the pallidum were the highest among all regions tested, and the r1-r2* relaxivity was the lowest (**Figure 3**). To make sure our results are not driven by the outlier values in the pallidum, we tried to exclude it from the comparisons between MRI and iron histology we show in **Figure 3b-c**. The correlation of the r1-r2* relaxivity with the iron concentration did not survive after excluding the pallidum (**Sup. Figure 31**). On the contrary, the correlations of R2* with the iron concentration and of the r1-r2* relaxivity with the iron mobilization remained significant even when the pallidum was excluded from the analysis (**Sup. Figure 31**).

Therefore, the correlation of the r1-r2* relaxivity with the iron concentration was driven mostly by the distinct behavior of the pallidum, while its correlation with the iron mobilization was stronger and more stable. These analyses demonstrate the enhanced sensitivity of the r1-r2* relaxivity to the iron homeostasis rather than to the absolute iron concentration.

Supplementary Figure 31

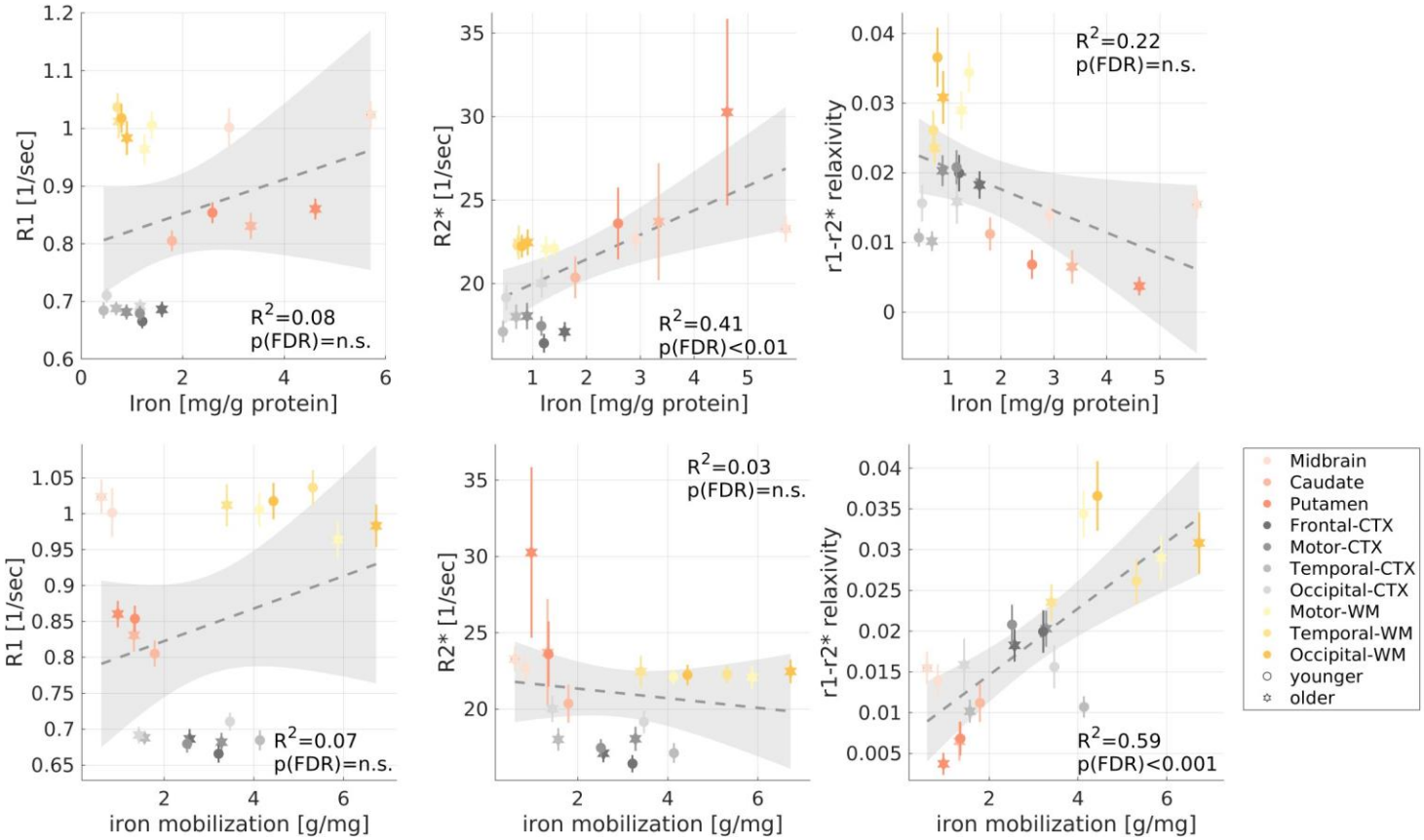

Sup. Figure 31: The correlations of MRI parameters with the iron environment when excluding the pallidum. (a) *Replication of Figure 3*b-c *excluding the globus pallidus. The iron concentration and the iron mobilization capacity (transferrin/iron ratio) estimate postmortem (from the literature[5,7,9]) in different brain regions of younger (aged 27-64 years, N>=7) and older (aged 65-88 years, N>=8) subjects vs. R1, R2* and the r1-r2* relaxivity measured in vivo across younger (aged 23-63 years, N =26) and older (aged 65-77 years, N=13) subjects (different marker shapes) in 10 brain regions (different colors), excluding the pallidum. The correlation of the r1-r2* relaxivity with the iron concentration did not survive after excluding the pallidum. On the contrary, the correlations of R2* with the iron concentration and of the r1-r2* relaxivity with the iron mobilization remained significant.*

Supplementary methods

R1-MTV dependency computation for phantoms.

We computed the linear dependency of R1 on MTV across samples with varying iron-binding protein concentrations and liposomal fractions[76]. This process was implemented in MATLAB. We extracted the MTV values from all voxels and pooled them into 12 bins spaced equally between 0.05 and 0.40. This was done so that the linear fit would not be heavily affected by the density of the samples in different MTV regimes. The median MTV of each bin was computed, along with the median R1. We fitted the following linear model across samples:

$$R1 = a * MTV + b$$

The slope of this linear model (a) represents the R1-MTV dependency. b is constant.